UNIVERSITA' DELLA CALABRIA

DIPARTIMENTO DI FISICA

DOTTORATO DI RICERCA IN
Scienze e Tecnologie Fisiche Chimiche e dei Materiali

Ciclo
XXXIII

Tesi

Thermo-Plasmonic triggered Bio-Photonic applications

Settore Scientifico Disciplinare
Fis/07

Coordinatore
Prof.ssa Gabriella Cipparrone

Firma oscurata in base alle linee guida del Garante della privacy

Supervisore scientifico interno
Prof. Cesare Umeton

Firma oscurata in base alle linee guida del Garante della privacy

Supervisore scientifico esterno
Prof. Luciano De Sio

Firma oscurata in base alle linee guida del Garante della privacy

Dottoranda
Dott.ssa Alexa Guglielmelli

Firma oscurata in base alle linee guida del Garante della privacy

---

Contents

Lists of Publications

This Ph.D. thesis is based on the following peer-reviewed journal articles:

1. De Sio, L., Cataldi, U., **Guglielmelli, A**., Bürgi, T., Tabiryan, N., & Bunning, T. J. - *Dynamic optical properties of gold nanoparticles/cholesteric liquid crystal arrays* - MRS Communications, 26 April **2018**, 1-6. (DOI 10.1557/mrc.2018.80)
2. **Guglielmelli A.**, Vasdekis A. E., De Sio L. - *Modular diffraction gratings in soft-composite materials* – J. Phys. D: Appl. Phys., **2018**. (DOI 10.1088/1361-6463/aaedf4)
3. Palermo G., **Guglielmelli A.**, Pezzi L., Cataldi U., De Sio L., Caputo R, De Luca A., Bürgi T., Tabiryan N. & Umeton C.- *A command layer for anisotropic plasmonic photo-thermal effects in liquid crystal*- Liquid Crystal, **2018**.(Invited Article) (DOI 10.1080/02678292.2018.1515370)
4. Annesi F., Pane A., Losso M. A., **Guglielmelli A.**, Lucente F., Petronella F., Placido T., Comparelli R., Guzzo M. G., Curri M. L., Bartolino R. & De Sio L. - *Thermo-Plasmonic Killing of Escherichia coli TG1 Bacteria - Materials*, 12(9), 1530, **2019**. (DOI 10.3390/ma12091530)
5. Pezzi L., Pane A., Annesi F., Losso M. A., **Guglielmelli A**., Umeton C., & De Sio, L. - *Antimicrobial Effects of Chemically Functionalized and/or Photo-Heated Nanoparticles* - Materials, 12(7), 1078, **2019**. (DOI 10.3390/ma12071078)
6. Pierini F., **Guglielmelli A.**, Urbanek O., Nakielski P., Pezzi L., Buda R., Lanzi M., Kowalewski T. A. & De Sio L. - *Thermoplasmonic-activated hydrogel based dynamic light attenuator* - Adv. Optical Mater. **2020**, 2000324. (DOI 10.1002/adom.202000324)
7. **Guglielmelli A.**, Rosa P., Contardi M., Prato M., Mangino G., Miglietta S., Petrozza V., Pani R., Calogero A., Athanassiou A., Perotto G. & De Sio L. - *Biomimetic keratin gold nanoparticle-mediated in vitro photothermal therapy on glioblastoma multiforme* – Nanomedicine, **2021,** 16:2, 121-138 (DOI 10.2217/nnm-2020-0349)

List of Figures

List of Tables

List of Acronyms

2PP	Two Photons Polymerization
3D	Three-Dimensional
AFM	Atomic Force Microscopy
AuNP/GNP	Gold Nanoparticle
AuNR/GNR	Gold Nanorod
AgNP	Silver NanoParticle
AR	Aspect Ratio
BSE	BackScattered Electrons
BY	Brilliant Yellow
CFU	Colony-Forming Unit
CLC, NLC , LC	Cholesteric, Nematic Liquid Crystal
CMOS	Complementary Metal Oxide Semiconductor
CTAB	CetylTrimethylAmmonium Bromide
CW	Continuous Wave
DAPI	4′,6-diamidino-2-phenylindole
DLS	Dynamic Light Scattering
DNA	DeoxyriboNucleic Acid
DVB	Divinylbenzene
EPR	Enhanced Permeability and Retention
EM	ElectroMagnetic
FACS	Fluorescence-Activated Cell Sorting
FITC	Fluorescein isothiocyanate
FPA	Focal Plane Array
FTIR	Fourier-Transform Infrared Spectroscopy
IFOV , FOV	Instantaneous Field Of View
Ker-AuNP	Keratin capped Gold Nanoparticle
LSPR	Localized Surface Plasmon Resonance
NETD	Noise Equivalent Temperature Difference
NIR	Near InfraRed
NP	NanoParticle
OD	Optical Density
PAL	Photo-Alignment Layer
PBS	Phosphate-Buffered Saline
PDMS	Polydimethylsiloxane
PEG	Poly(Ethylene Glycol)
PI	Propidium Iodide
PPT	Plasmonic Photo-Thermal
PPTT	Plasmonic Photo-Thermal Therapy
ROI	Region Of Interest
RPM	Revolutions Per Minute
SEM, TEM	Scanning and Transmission Electron Microscopy
TGA	ThermoGravimetric Analysis
U87-MG	Uppsala 87-Malignant Glioma
UV-Vis	Ultraviolet–Visible
WAXS	Wide Angle X-ray Scattering
XPS	X-ray Photoelectron Spectroscopy

List of Symbols and Constants

$\parallel$	Parallel direction
$\perp$	Perpendicular direction
$\mathbf{c_0}$	Speed of light in vacuum 2.99792458×10^{8} (m s^{-1})
$\boldsymbol{\varepsilon_0}$	Dielectric vacuum constant 8.85×10^{-12} (F m^{-1})
$\boldsymbol{\nu}$	Frequency (s^{-1})
$\boldsymbol{\omega}$	Angular frequency (rad $s^{-1)}$
$\boldsymbol{\omega_p}$	Plasma frequency (rad s^{-1})
$\boldsymbol{\lambda}$	Free space illumination wavelength (m)
$\boldsymbol{\lambda_{LSPR}}$	LSPR peak wavelength (m)
$\boldsymbol{k}$	Wave vector (m^{-1})
$\boldsymbol{n}$	Refractive index
$\boldsymbol{\varepsilon_r}$	Relative dielectric constant, relative permittivity
$\boldsymbol{\varepsilon_1, \varepsilon_2}$	Real, Imaginary parts of dielectric function
$\boldsymbol{\varepsilon_m}$	Surrounding medium dielectric constant
a or R	NP radius (m)
d	NP diameter (m)
V	NP volume (m^3)
N	Total number of NPs
D	Intra-particle distance (m)
$\mathbf{P_j}$	Depolarization factors along the axes
$\boldsymbol{\gamma}$	Damping constant (s^{-1})
E	Electric field (V m^{-1})
$\mathbf{E_0}$	External electric field amplitude (V m^{-1})
D	Electric displacement (C m^{-2})
J	Electric current density (A m^{-2})
$\boldsymbol{\Delta T_{NP}}$	NP temperature increase (K)
$\boldsymbol{\Delta T(r)}$	Temperature increase outside the NP (K)
$\mathbf{q_j}$	Power delivered by the j^{th} NP (W)
$\mathbf{k_h}$	Host medium thermal conductivity (W m^{-1} K^{-1})
$\boldsymbol{\chi_{NP}}$	Electric susceptibility
$\boldsymbol{\rho}$	Mass density (Kg m^{-3})
$\boldsymbol{c}$	Specific heat capacity (J K^{-1} Kg^{-1})
h	Plank constant 6.6×10^{-34} (J s)
$\mathbf{k_B}$	Boltzmann’s constant 1.4×10^{-23} (J K^{-1})
$\mathbf{W_\nu}$	Spectral radiance (W sr^{-1} m^{-2} Hz^{-1})
I	Light or laser intensity (Wm^{-2})
P	Laser power (W)
$\boldsymbol{\sigma_{ext}}$	NP extinction cross section (m^2)
$\boldsymbol{\sigma_{abs}}$	NP absorption cross section (m^2)
$\boldsymbol{\sigma_{sca}}$	NP scattering cross section (m^2)

Introduction and Contents

The role of photonics is predominant in our lives today. The importance of light cannot be taken for granted, because it is essential to most aspects of our contemporary society.[1] Photonics is a branch of optics, which essentially studies the photons' generation, detection, and manipulation. Furthermore, nowadays, photonics has taken on a different connotation, which concerns the correct use of light as a tool for human beings' benefit. It is not surprising that photonics has become a part of every aspect of our life, from everyday lives to highly innovative science. In fact, it is exploited in applications involving data transmissions, such as optical fibers and optoelectronics, laser printing, two-photon polymerization, digital holography, fiber-optic lasers and sensors. [1] Besides, it is currently fully involved in a wide range of healthcare applications, such as imaging used in hospitals or lasers used for optometric surgery, imaging and disease prevention, and endoscopy.[2] But the aspect that, today, most captures the attention of not only basic scientific research but also of clinical research, concerns photonics which lends itself as a decisive tool in biomedicine, theranostics, and above all precision nanomedicine, an emerging field often called nanobiophotonics.[3]

Nano-photonics studies the interaction of light with nanostructured matter and offers the advantage to confine electromagnetic (EM) waves to dimensions lower than the wavelength of the incident radiation, coupling the light with materials characterized by a high dielectric permittivity. Among all these materials, considerable interest has been directed towards metal plasmonic nanoparticles, such as Gold NanoParticles (AuNPs). [4] One of their most fascinating and useful aspects is their resonant optical property and the interconnected light-triggered thermal effect, the Plasmonic Photo-Thermal (PPT) effects.

When AuNPs are illuminated by appropriate incident radiation, they concentrate a strong EM field at the nanoscale, and cause a coherent and dipolar oscillation of the surface electrons (Localized Surface Plasmon Resonance, LSPR), the damping of which leads to the heat produced by Joule dissipation.[5] This phenomenon is triggered under excitation by a suitable light of a wavelength that matches the intrinsic LSPR at the interface. AuNPs are harmless, biocompatible, and unarmed until a suitable incident light triggers them at the resonant frequency when they become fearsome weapons that convert light into highly localized heat. This phenomenon has turned AuNPs into a promising tool for cancer treatment[6], makes them the best candidates for applications requiring spatio-temporal confined heating.[7]

Cancer is one of the greatest, ever-present challenges facing our world. It affects everyone regardless of age, gender, or social status and represents a huge burden on patients, families, and society in general. If no further action is taken, the European Research Commission says, the number of people newly diagnosed with cancer each year in Europe will increase from the current 3.5 million to over 4.3 million by 2035. In light of that statement, cancer has been included among the missions in need of urgent resolution plans in the European Framework Program for Research and Innovation, Horizon Europe 2021-2027.

AuNP-based plasmonic photothermal therapy (PPTT) has been extensively explored for several cancer treatments, generating strong success, and in many cases achieving promising results.[8-9] Strong optical absorption and highly efficient photothermal conversion at the cancer sites are crucial to the high efficacy of AuNPs-based PPTT. [10]

Ideal nano-formulations for PPTT should meet several criteria: (i) have strong and tunable LSPR, especially in the "biological window" (NIR wavelengths) for better tissue penetration, (ii) high photo-thermal efficiency, (iii) have low toxicity by changing the common colloidal stabilizer CTAB know to be toxic, (iv) and be easy to functionalize via bioconjugation for actively targeting specific cancer sites and maximize the cellular uptake.[7]

The LSPR frequency can be easily tuned, in the most suitable spectral band, by changing the particles' size, shape, or environment, and the light-to-heat conversion can be optimized.[11] To actively deliver AuNPs in the target tumoral site, several strategies can be exploited, such as antibody-antigen or ligand-receptor recognition, to have a highly targeted action.[12] In that way, laser-induced local heating of tumoral tissue through PPTT using either pulsed or continuous laser radiation and mediated by light-absorbing AuNPs provides precisely localized damage limited to even single cells.[13]

Like cancer cells, most bacteria (such as the mesophilic strain of bacteria Escherichia Coli, E. Coli) viability is compromised when experiencing a temperature greater than 45 °C. Therefore, a similar PPTT strategy can be explored, for sterilization and disinfection applications, such as a valid tool for dealing with the emergency of antibiotic resistance. [14-16]

The possibility of tuning the LSPR band, simply by acting on the refractive index of the medium surrounding the AuNPs, offers incredible possibilities for the realization of optical and biosensory devices and represents one of the crucial aspects of this thesis work. Precisely for this purpose, a particular class of soft materials was investigated, thermotropic Liquid Crystals (LCs), whose optical properties undergo substantial changes under the thermal effect. Despite the intriguing properties of LCs, they suffer from a lack of biocompatibility. To channel towards biomedical applications, it was essential to consider another class of smart and thermo-responsive materials, the hydrogels.

Furthermore, probing and exploiting the AuNPs plasmonic heating, both at macroscale using the indirect method or at the nanoscale using thermo-responsive materials, is mandatory for a safe and side-effect free PPTT. This is the main topic of my Ph.D. thesis.

The work in this thesis is organized as follows:

- The **first chapter** aims at providing a general overview of the physical phenomena underlying the unique properties of AuNPs. The LSPR optical phenomenon is treated with the quasi-static approximation, and then the main parameters responsible for the plasmon band tuning are described.
- In the **second chapter,** the basic theory behind the AuNPs light-to-heat conversion phenomenon is discussed. The general equations governing the distribution of heat from an AuNP to its surrounding medium is not a new concept; the heat transfer equation has been used to describe all the systems in which a transfer of heat

between different media occurs for decades. Finally, the PPT heating produced by an ensemble of AuNPs and its potential uses is examined.

- In the **third chapter**, various techniques to detect the temperature triggered by LSPR at the macro and nanoscale are introduced. In particular, the infrared thermography technique is described in detail, underlining the pros and cons of using this investigation method. Then we focus on using smart and heat-responsive materials, from whose response to the temperature changes induced by the AuNPs, it is possible to detect the temperature variation at the nanoscale. The materials used for these nano-thermometry applications are mainly LCs and hydrogels, soft materials whose optical properties change in response to temperature changes. The transition from LCs to hydrogels represents a necessary step to approach the PPT effect applications in the biomedical field. This first part of the experiments was mainly performed in the Optics Laboratory (University of Calabria) coordinated by Prof. Cesare Umeton. Besides, for the part concerning the hydrogels fabrication and morphological characterization, we collaborated with Dr. Filippo Pierini, from the Department of Biosystems and Soft Matter, Institute of Fundamental Technological Research, Polish Academy of Sciences, Warsaw. These experiments were published and reported in articles 1, 3, 6 of the publication list.
- In the **fourth** and last chapter, two applications of the biomedical field's PPT effect are finally presented. The first essentially concerns the use of Au nano-heaters, as a tool for the fight against antibiotic resistance. An in-vitro method for killing bacteria is presented, taking Escherichia Coli as a model mesophilic bacterium, by triggering rod-shaped AuNPs with NIR light. On the other hand, the second application focuses on the fight against tumors through PPTT mediated by a completely innovative class of AuNPs, made extremely biocompatible by bioconjugation with a protein, keratin. The use of Ker-AuNPs has made it possible to obtain a highly stable and biocompatible colloidal solution, excellent internalization in glioblastoma cancer cells, and considerable heat-induced lethality at the nanoscale towards glioblastoma cancer cells. The experiments concerning the PPTT-based bacteria disinfection were conducted in the Physics Department's cleanroom (University of Calabria), collaborating with researchers from CNR-Lab. Licryl, Institute NANOTEC. The Ker-AuNP-based PPT experiments applied to glioblastoma cancer cells were conducted in the Biophotonics laboratory of Prof. Luciano De Sio, Department of Medical-Surgical Sciences and Biotechnology, Sapienza University. Furthermore, for the synthesis and morphological characterization of Ker-AuNPs we had the fundamental support of Dr. Giovanni Perotto of Smart Materials, Italian Institute of Technology (IIT). Part of the results presented can also be accessed in the 4 and 7 published journal articles.
- In the **appendix** at the end of the thesis, an interesting application in the photonics field, with possible implications in the medical field, is described. A new class of waveguides, embedded in a transparent and biocompatible material, the PDMS, have been created using direct laser writing and the two-photon photopolymerization (2PP) technique.[17] The 2PP 3D microfabrication method

works within the near-infrared (NIR) radiation, implementing additive manufacturing with sub-diffraction limit resolution within the bulk of a photosensitive material, reaching a much better structural resolution and quality than the widely exploited soft lithography method.[18] This technique has allowed the realization of very shallow waveguides at the micrometric scale. Subsequently, employing a thin film of photo-aligning and a thin layer of Nematic LCs (NLCs), the waveguide coupled light's polarization-dependent behavior was investigated, exploiting the intrinsic NLC birefringence. This application could pave the way for realizing PPTT, not only of superficial tumors but also of deep tumors reachable by light coupled in micrometric and biocompatible fibers. The fabrication and characterization of these waveguides were entirely performed in the Optics Laboratory of Prof. Demetri Psaltis and the cleanroom of the Center for MicroNanotechnology (CMi) at the EPFL, École Polytechnique Fédérale de Lausanne, Switzerland.

Introduction and Contents (Italian)

La fotonica ha assunto un ruolo predominante nelle nostre vite, tanto da rendere l'impiego della luce essenziale per la maggior parte degli aspetti della nostra società contemporanea. Essenzialmente la fotonica è una branca dell'ottica, che studia la generazione, il rilevamento e la manipolazione di fotoni. Inoltre, al giorno d'oggi, la fotonica sta via via assumendo una connotazione diversa, che vira verso il corretto utilizzo della luce come strumento a beneficio degli esseri umani.

La fotonica trova impiego in applicazioni concernenti la trasmissione di dati (fibre ottiche e optoelettronica), stampa laser, scrittura laser diretta e polimerizzazione a due fotoni, olografia digitale e sensori. Inoltre il suo impiego ormai si estende anche ad applicazioni sanitarie, come le tecniche di imaging, le metodiche diagnostiche per la prevenzione di malattie, la chirurgia laser e l'endoscopia. Ma l'aspetto che, oggi, cattura maggiormente l'attenzione della ricerca scientifica traslazionale, riguarda la fotonica che si presta come strumento determinante in biomedicina, teranostica e soprattutto nanomedicina di precisione, un campo emergente spesso definito nanobiofotonica.

La nano-fotonica studia l'interazione della luce con la materia nano-strutturata ed offre il vantaggio di poter confinare le onde elettromagnetiche (EM) in dimensioni inferiori alla lunghezza d'onda della radiazione incidente, accoppiando la luce con materiali caratterizzati da un'elevata permittività dielettrica. Tra tutti questi materiali, le nanoparticelle plasmoniche metalliche, come le nanoparticelle di oro (AuNPs), rivestono un ruolo di particolare rilievo. Il loro fascino deriva maggiormente dalle loro proprietà ottiche correlate alle proprietà foto-termiche.

Quando le AuNPs sono illuminate da un'opportuna radiazione incidente, confinano un forte campo EM su scala nanometrica; viene, così, generata un'oscillazione coerente e dipolare degli elettroni liberi di superficie (Risonanza Plasmonica Superficiale Localizzata LSPR), il cui smorzamento produce calore tramite effetto Joule. Questo fenomeno è indotto dall’interazione con un fascio di luce caratterizzato da una lunghezza d'onda che corrisponde proprio all'LSPR delle AuNPs. Le AuNPs infatti sono innocue e biocompatibili, fino a quando non vengono irradiate ed eccitate da una specifica radiazione risonante, che le trasforma in potentissime nano-sorgenti di calore altamente localizzato. L’effetto fototermico ha reso le AuNPs uno strumento promettente per la cura del cancro, e le migliori candidate per applicazioni che necessitano di calore confinato sia nello spazio che nel tempo.

Il cancro è una delle maggiori sfide da affrontare; colpisce tutti indipendentemente dall'età, dal sesso o dallo stato sociale e rappresenta un enorme fardello per i pazienti, le famiglie e la società in generale. Senza ulteriori e specifiche azioni, afferma la commissione Europea per la ricerca, il numero di persone con una nuova diagnosi di cancro ogni anno in Europa aumenterà dagli attuali 3,5 milioni a oltre 4,3 milioni entro il 2035. Proprio alla luce di tali previsioni, il cancro è stato inserito tra le missioni che necessitano di urgenti piani risolutivi, nel programma Europeo per la ricerca e l’innovazione, Horizon Europe 2021-2027.

La terapia plasmonica fototermica (PPTT) che fa uso di AuNPs è stata estensivamente esplorata per il trattamento del cancro riscuotendo forte successo ed ottenendo in molti casi risultati incoraggianti e promettenti. Affinché la PPTT venga attuata sortendo gli effetti desiderati bisogna disporre di AuNPs caratterizzate da un’elevata sezione d’urto d’assorbimento e un’efficiente conversione fototermica localizzata nella regione di interesse.

Le nano-formulazioni ideali per la PPTT devono soddisfare diversi criteri: (i) una LSPR facilmente sintonizzabile nella "finestra biologica" (lunghezze d'onda nel vicino infrarosso, NIR) per una migliore penetrazione nei tessuti; (ii) efficienza di conversione luce-calore significativa, (iii) citotossicità trascurabile, (iv) funzionalizzazione tramite bio-coniugazione facilmente accessibile, così da bersagliare selettivamente le cellule tumorali e massimizzarne l'uptake cellulare.

La frequenza della LSPR può essere facilmente regolata, nella banda spettrale più adatta, cambiando le dimensioni, la forma o l'ambiente circostante delle AuNPs; allo stesso modo la conversione da luce a calore può essere ottimizzata. Al fine di veicolare attivamente le AuNPs nel sito tumorale bersaglio, è possibile sfruttare diverse strategie come il riconoscimento anticorpo-antigene o recettore-ligando, così da avere un'azione altamente mirata e localizzata, scongiurando eventuali effetti collaterali sui tessuti circostanti sani. In questo modo, il riscaldamento locale del tessuto tumorale indotto dal fascio laser tramite PPTT procura un danno spazialmente confinato, che può raggiungere precisioni anche dell’ordine della singola cellula.

In maniera similare alle cellule tumorali, anche la vitalità della maggior parte dei batteri (come il ceppo mesofilo di batteri Escherichia Coli, E. Coli) è compromessa quando questi ultimi sono sottoposti ad una temperatura superiore a 45°C. Pertanto, la strategia PPTT può essere efficientemente traslata, anche per applicazioni di sterilizzazione e disinfezione, così da essere un valido strumento per affrontare l'emergenza dell’antibiotico-resistenza.

La possibilità di adattare la banda plasmonica, agendo semplicemente sull'indice di rifrazione del mezzo che circonda le nanoparticelle, offre incredibili possibilità per la realizzazione di dispositivi ottici monitorabili dall'esterno con la luce, e rappresenta uno degli aspetti cruciali di questo lavoro di tesi. Proprio a questo scopo è stata indagata una classe particolare di materiali intelligenti, i cristalli liquidi termotropici (LCs), le cui proprietà ottiche subiscono sostanziali modifiche sotto l'effetto termico. Nonostante i cristalli liquidi godano di intriganti proprietà, essi peccano di mancanza di biocompatibilità, per cui è stato fondamentale, al fine di indirizzare la ricerca alle applicazioni biomediche, prendere in analisi un'altra classe di materiali termo-responsivi, gli idrogel.

Sintetizzando, lo scopo principale di questo lavoro di tesi consiste nel sondare e sfruttare il riscaldamento plasmonico indotto dalle AuNPs, sia su macroscala avvalendosi della termografia infrarossa, sia alla nanoscala mediante i materiali termosensibili, in modo da ottenere una PPTT sicura e priva di effetti collaterali.

La tesi è organizzata come segue:

- Il **primo capitolo** mira a fornire una panoramica generale dei fenomeni fisici alla base delle proprietà ottiche delle AuNPs. Il fenomeno della LSPR è stato trattato sfruttando l'approssimazione quasi-statica, dopodiché sono stati illustrati i principali parametri responsabili del "tuning" della banda plasmonica.
- Il **secondo capitolo** tratta il fenomeno della conversione di luce in calore ad opera delle AuNPs. Vengono illustrate le equazioni generali che governano la diffusione del calore generato da una singola AuNP al suo mezzo circostante, ottenute partendo dalle ben note equazioni di trasferimento del calore. Infine, è stato esaminato il riscaldamento prodotto da un insieme di AuNPs e i possibili utilizzi.
- Nel **terzo capitolo**, vengono introdotte diverse tecniche atte a monitorare e misurare la temperatura indotta a seguito della LSPR alla macro e nano scala. In particolare, viene descritta dettagliatamente la tecnica di termografia infrarossa, sottolineando i pro e i contro dell'utilizzo di tale metodica di indagine. Successivamente ci si è concentrati sull'impiego di materiali intelligenti e termo-responsivi, dalla cui reazione ai cambiamenti di temperatura indotti dalle AuNPs, si riescono ad ottenere informazioni sulla variazione di temperatura alla nano-scala. I materiali utilizzati, in queste applicazioni di nano-termometria, sono soprattutto i cristalli liquidi e gli idrogel, materiali soffici le cui proprietà ottiche mutano in funzione dei cambiamenti di temperatura. Il passaggio dai cristalli liquidi agli idrogel rappresenta uno step necessario per avvicinarsi alle applicazioni dell'effetto fototermico al campo biomedico. Questa prima parte degli esperimenti è stata condotta principalmente nel Laboratorio di Ottica del Prof. Cesare Umeton dell'Università della Calabria. Inoltre, per la parte riguardante la fabbricazione e la caratterizzazione morfologica dell'idrogel, ci siamo avvalsi dell'importante collaborazione con il Dr. Filippo Pierini, del Dipartimento di Biosistemi e Materia Soffice, Istituto di Ricerca Tecnologica Fondamentale, Varsavia. I risultati di questi esperimenti sono oggetto degli articoli 1, 3, 6 della lista delle pubblicazioni.
- Nel **quarto capitolo**, vengono infine presentate due applicazioni dell'effetto fototermico nell'ambito biomedico. La prima riguarda essenzialmente l'impiego delle AuNPs come strumento per la lotta contro l'antibiotico-resistenza. Viene

presentato un metodo in-vitro per indurre mortalità nei batteri, prendendo come batterio mesofilo modello il ceppo di E. Coli, ed eccitando con luce NIR delle AuNPs a forma di bastoncino, le Au-Nanorods. La seconda applicazione invece si focalizza sulla lotta contro i tumori tramite PPTT mediata da una nuovissima generazione di AuNPs bioconiugate con una proteina, la keratina (Ker-AuNPs). L'impiego delle Ker-AuNPs ha permesso di ottenere una soluzione colloidale fortemente stabile e biocompatibile, un'ottima internalizzazione nelle cellule tumorali di glioblastoma, ed una notevole letalità indotta dal calore alla nanoscala nei confronti delle cellule tumorali. La campagna sperimentale concernente i batteri è stata principalmente condotta all'interno della camera bianca nel Dipartimento di Fisica dell'Università della Calabria, in collaborazione con i ricercatori del CNR-Lab. Licryl, Istituto NANOTEC. Gli esperimenti di PPTT, sfruttando le Ker-AuNPs applicati a cellule cancerose di glioblastoma sono stati, invece, condotti nel laboratorio di Biofotonica del Prof. Luciano De Sio, Dipartimento di Scienze Medico-Chirurgiche e Biotecnologie, Università La Sapienza. Inoltre, per la sintesi e la caratterizzazione delle Ker-AuNPs ci siamo avvalsi del prezioso supporto del Dr. Giovanni Perotto dell'IIT (Genova). È possibile accedere a parte dei risultati negli articoli 4 e 7 pubblicati su rivista.

- Nell'**appendice** a fine tesi, viene descritta un'interessante applicazione in ambito fotonico. Facendo uso della scrittura diretta tramite laser e della tecnica di fotopolimerizzazione a due fotoni (2PP) è stata realizzata una nuova classe di guide d'onda, incorporate in un materiale trasparente e biocompatibile, il PDMS. Il metodo 2PP di microfabbricazione 3D opera nel range di radiazione del NIR e consente la scrittura di guide d'onda all'interno di un materiale fotosensibile, raggiungendo una risoluzione strutturale e una qualità nettamente migliori rispetto al più comune metodo di litografia. Infatti, tale tecnica ci ha permesso di realizzare guide d'onda alla scala micrometrica, molto superficiali. Successivamente tramite l'impiego di un layer nanometrico di fotoallineante e uno strato sottile di CLs, è stato indagato il comportamento dipendente dalla polarizzazione della luce accoppiata nelle guide d'onda, sfruttando la birifrangenza intrinseca dei CLs. Questa applicazione potrebbe aprire la strada alla realizzazione di PPTT, non solo per tumori superficiali, ma anche tumori profondi e non facilmente accessibili, resi raggiungibili dalla luce accoppiata in fibre micrometriche e biocompatibili. La fabbricazione e la caratterizzazione di queste guide d'onda è stata interamente eseguita nel Laboratorio di Ottica del Prof. Demetri Psaltis e nella camera bianca del Centro di MicroNanoTecnologia (CMi) dell'EPFL, École polytechnique fédérale de Lausanne, in Svizzera.

Chapter 1

FUNDAMENTALS OF LOCALIZED SURFACE PLASMON RESONANCE IN GOLD NANOPARTICLES

In this chapter, the fascinating optical phenomenon of Localized Surface Plasmon Resonance (LSPR), arising from the interaction between an electromagnetic (EM) wave and the conduction electrons in a Gold Nanoparticles (AuNPs), is described. In order to describe the LSPR, from an optical point of view, it is necessary to explain it in terms of the extinction cross-section, since the phenomenon is closely related to the phenomenon of absorption as to that of scattering of light radiation. The optical process is presented, by considering the interaction of metal nanoparticles (NPs) with an EM wave in order to induce the resonance condition. This first chapter deals with the theoretical description of the LSPR by means of the quasi-static approximation approach, valid for sub-wavelength spheres, without going into the details of the Mie theory that is required to discuss NPs of larger dimensions and it is not strictly required for the thesis purpose. In the concluding sections some of the major morphological, chemical, and physical factors that influence the LSPR, and how to properly manipulate them according to the required application, are investigated.

1.1 Introduction to Nano-Plasmonics

Gold has always aroused a strong interest, for its unique chemical and optical properties, both in its macroscopic and microscopic state, but the most intriguing phenomena emerge in the metallic structures reduced to the nanoscale.

On a macroscopic scale, gold is characterized by its unique bright yellow color and its chemical stability. At the nanoscale, the optical phenomena manifest themselves immediately in a perceptible way to our eyes, with very precise colors: indeed a solution containing spherical NPs has a characteristic purple-red color.

The behavior of the matter at the nanoscale is unexpected and different from that of bulks and is related to the unusual electronic configuration combines with other effects due to the extremely small dimensions: (i) high ratio of surface atoms to bulk atoms, so that overall properties are dictated by the surface atoms, (ii) EM confinement when an optical wave interacts with a AuNP giving rise to their specific color through a LSPR, and (iii) quantum effects that explain the change from metallic to semiconducting character of very small NPs.[19] The branch of optics, and more particularly of nanophotonics, that deals with the behavior of EM waves in the visible range in nanostructured materials is NanoPlasmonics[20].

In particular, the LSPR phenomenon allows to push down and amplify the electric field at the AuNPs surface, on a scale much shorter compared to the incident radiation wavelength. In the far field, such resonant excitation leads to both strong absorption and scattering of light. The study of these phenomena and their applications is the main goal of NanoPlasmonics.

1.2 Optical behavior of metal: the dielectric function

AuNPs have a considerable number of easily polarizable and free conduction electrons, predominantly distributed at the surface, which is an essential prerequisite for interaction with EM fields. The main consequence is that the AuNPs are capable of squeezes EM waves into very small scales; therefore they possess the ability to amplify the EM field at nanometric distance from the metal surface. This optical process is one of the fundamental phenomena in the study of plasmonics, in fact, the term "plasmons" refers to collective oscillations of free electrons in metals. In the presence of an oscillating EM field, the conduction band free electrons of metal undergo collective oscillations in resonance with a particular frequency of light, the so-called plasmon resonance ω_{LSPR}. The electric component of the external optical field exerts a force on the conductive electrons and displaces them from their equilibrium positions creating uncompensated charges at the NPs surface. The difference in the total charge present at the NPs surface behaves as a restoring force, causing a dipolar oscillation of all electrons, with the same phase. Hence, the plasmon in an NP can be considered as a mass-spring harmonic oscillator driven by the energy resonant light wave, where the electron cloud oscillates like a simple dipole in parallel direction to the electric field of the EM radiation. (**Figure 1.1**)

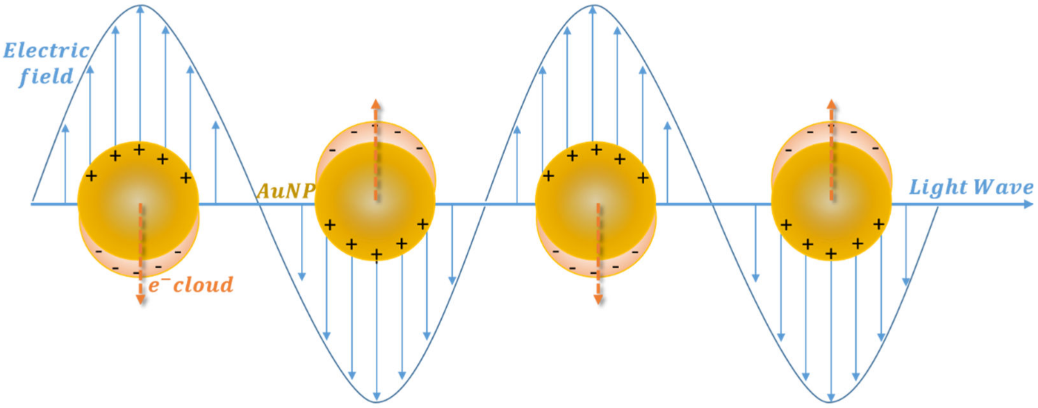

Figure 1.1 *– Scheme of LSPR for a sphere, showing the displacement of the conduction electron charge cloud relative to the nuclei.*

Such a coherent and dipolar oscillation of the electron cloud, after the interaction with the electric field $\vec{E}(\vec{r},\omega)$ creates a dynamic polarization $\vec{P}(\vec{r},\omega)$. This quantity expresses the displacement of the electron cloud relative to the core atoms, in response to the $\vec{E}(\vec{r},\omega)$. The polarized atoms result in the creation of an electric displacement $\vec{D}(\vec{r},\omega)$ linked to the excitation $\vec{E}(\vec{r},\omega)$ by the relationship[21-22]:

$$\vec{D}(\vec{r},\omega) = \varepsilon_0\varepsilon(\omega)\vec{E}(\vec{r},\omega) \tag{1.1}$$

$\varepsilon(\omega)$, the metal dielectric function, fully describes the optical response of metal to the EM excitation wave over the entire frequency spectrum. If the surrounding medium is vacuum, ($\varepsilon(\omega) = 1$, $\vec{D} \propto \vec{E}$), ε accounts for any kind of materials and in the general case, it is a complex function expressed as:

$$\varepsilon(\omega) = \varepsilon_1(\omega) + i\varepsilon_2(\omega) \tag{1.2}$$

For metals, ε is dominated by its real part which is a negative function (**Figure 1.2**). ε is related to the optical complex index $\tilde{n}$ by:

$$\varepsilon = \tilde{n}^2 = [n + ik]^2 = n^2 - k^2 + 2nki \tag{1.3}$$

$\varepsilon, \tilde{n}$ are functions of the angular frequency ω ($\omega = 2\pi c/\lambda$, linked to the wavelength λ). This dependence often appears implicitly in equations, in order to simplify the notation, but is fundamental since the LSPR is directly linked to it.

As described before, the oscillator model is the simplest analytical way to describe the polarization and gives rise to Drude dielectric function [21, 23-24] of the free electron gas, modelling the optical properties of metal by a plasma model, and expressed as follow:

$$\varepsilon(\omega) = 1 - \frac{\omega_p^2}{\omega^2 + i\gamma\omega} \tag{1.4}$$

Electron oscillating motion is damped via collision at a typical frequency $\gamma = 1/\tau$, τ ($\approx 10^{-14} s$) is the relaxation time and $\omega_p^2 = \frac{ne^2}{\varepsilon_0 m}$ is the plasma frequency.[5]

For visible and near-infrared frequencies, where $\gamma \ll \omega_p$, the above relation would be reduced to the following form as:

$$\varepsilon(\omega) \approx 1 - \frac{\omega_p^2}{\omega^2} \tag{1.5}$$

The Drude model is a good approximation for describing the dielectric functions of an ideal free-electron metal ($\varepsilon \to 1, \omega \gg \omega_p$). However, Drude's model is not precise and detailed enough, as it mainly considers free electrons (intraband transitions), completely neglecting the bound electrons contribution (interband transitions), which plays an important role for gold [25-26], so an extension to this model is needed. In this framework, equation (1.5) needs a slight correction by replacing the factor 1 with a constant ε_∞ (usually

$1 \leq \varepsilon_\infty \leq 10$) that accounts for transitions that do not need to be explicitly expressed in the visible range, leading to:

$$\varepsilon(\omega) = \varepsilon_\infty - \frac{\omega_p^2}{\omega^2 + i\gamma\omega} \tag{1.6}$$

From these inaccuracies the Drude model fails to predict exactly the experimental data, the validity limits are evident in **Figure 1.2** where the real ε_1 and the imaginary ε_2 components of the complex dielectric function are plotted.

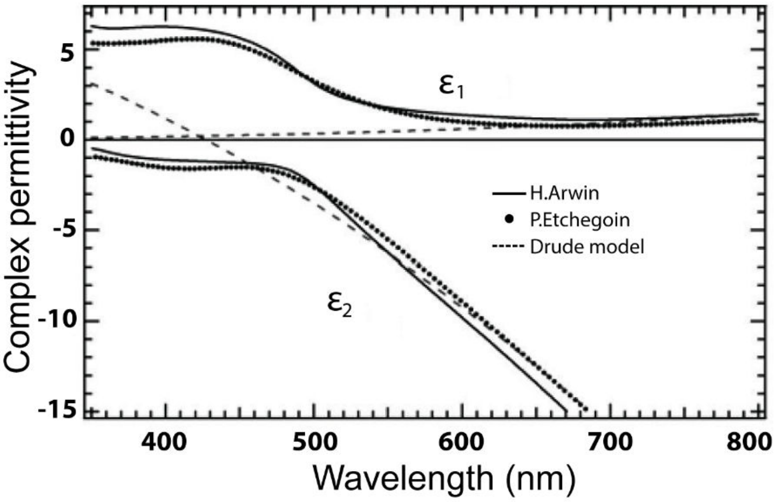

Figure 1.2 *– The Au complex dielectric function* $\varepsilon = \varepsilon_1 + i\varepsilon_2$*. The ellipsometric experimental curve*[27] *(continuous line), the analytical curve*[26] *(large dots) obtained on Johnson and Christy's data*[25] *and the theoretical curve from Drude model (dashed line). This model accounts well for the free electron contribution but not for the bound electrons (intraband transitions). This discrepancy is clearly visible in the range of 300 nm to 530 nm.*

The accurate measurement of the dielectric function is crucial for reasonably modelling the optical response of AuNPs. One of the preferred measurements was performed by Johnson and Christy in 1972[25] and an approximated analytical model has been provided by Etchegoin[26]. In the visible frequency range, especially in the violet/near-UV region, given the important role played in AuNPs by interband transitions, the free-electron model is not accurate, causing an increase in ε_2. Indeed, Au has at least two interband transitions at λ~470 and ~330nm, which are fundamental to obtain a reliable analytic model for $\epsilon(\omega)$.[26]

1.3 Quasi-static approximation for sub-wavelength AuNPs

From a theoretical point of view, for an isolated spherical AuNP characterized by a diameter much smaller than the wavelength of visible light (d<<λ) (quasi-static approximation), the distortion of the electron cloud caused by the electric field can be defined by the metal polarizability. In particular, when the NP involved in the optical process is a sub-wavelength metal NP, the interaction with the EM field can be investigated using the simple quasi-static approximation, introduced first by Rayleigh who studied the scattering of light from small NPs.[24] Assuming the aforementioned conditions, the phase of the harmonically oscillating EM field is basically constant within the NP volume, allowing to determine the spatial field distribution by simply assuming the case of a NP located in an electrostatic field.

On the contrary, if the sphere diameter is comparable with the wavelength (d≊λ) the spatial variation of the field within the NP would create a multipolar surface charge distribution. If instead d<<λ (generally less than 30nm), the field inside the sphere can be considered uniform and the charge distribution on the sphere surface creates a single dipole (dipole approximation); the same is true in the time domain: the propagation time inside the sphere will be very small compared to the oscillation period of the field. In the quasistatic limit, the excitation field and the electronic polarization are in phase (no retardation effect) and the electrons are displaced globally. In this case, the problem is simplified, neglecting the temporal dependence of the applied field, to a simple polarization effect of a sphere immersed in a uniform field, which is solved using the Laplace equation, setting suitable boundary conditions.[5]

For a theoretical discussion of the problem, it is reasonable, to begin with the simpler geometric shape for an analytical treatment: an isotropic, homogeneous sphere, characterized by a radius a and positioned at the origin of a uniform, static electric field $E = E_0\hat{z}$ (**Figure 1.3**).

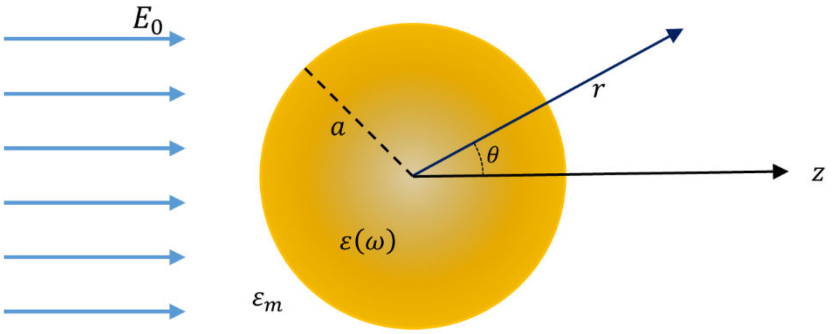

Figure 1.3 *– Sketch of a homogeneous sphere placed into an electrostatic field.*

The dielectric constant ε_m describes the surrounding, isotropic and non-absorbing medium, while the dielectric function ε (ω) (considered as a simple complex number ε) describes the dielectric response of the sphere. Also assume that the field lines are parallel to the z-direction, at sufficient distance from the sphere.[5]

In this framework of an electrostatic approach[28], we are interested in finding a solution to the Laplace equation for the electric potential, which enables the calculation of the electric field.

$$\nabla^2\phi = 0 \longrightarrow \mathrm{E} = -\nabla\phi \tag{1.7}$$

Thanks to the azimuthal symmetry, a general solution for the equation (1.7, can be written as follows:[29]

$$\phi(\mathrm{r},\theta) = \sum_{l=0}^{\infty}\left[A_l r^l + B_l r^{-(l+1)}\right]P_l(\cos\theta) \tag{1.8}$$

where A_l and B_l are coefficients to be determined, $P_l(\cos\theta)$ are the Legendre polynomials of order l, which often appear in physics problems expressed in spherical coordinates. It must be imposed that at the origin the potentials are finite, and two boundary conditions both for $r \to \infty$ and for $r = a$ (NP surface).[5] In particular, it is required that: (i) at large distance from the sphere, the electric field is the unperturbed applied field ($r \to \infty, \phi_{out} \to -E_0 z$); (ii) continuity of the tangential components of the electric field, and (iii) continuity of the normal components of the displacement field.[5] Considering these requirements it is straightforward to obtain the solution for the potentials ϕ_{ins} inside and ϕ_{out} outside the sphere[29]:

$$\phi_{in} = -\frac{3\varepsilon_m}{\varepsilon + 2\varepsilon_m}E_0 r\cos\theta \tag{1.9}$$

$$\phi_{out} = -E_0 r\cos\theta + \frac{p \cdot r}{4\pi\varepsilon_0\varepsilon_m r^3} \tag{1.10}$$

Therefore, substantially, the potential outside the sphere, ϕ_{out} is given by the sum between the contribution of the applied field and the contribution deriving from a dipole placed at the NP center. Therefore, the application of the field induces inside the sphere a dipole moment p of magnitude proportional to $|E_0|$. Introducing the polarizability defined via $p = \varepsilon_0\varepsilon_m \propto E_0$, we obtain:

$$\alpha = 4\pi a^3\frac{\varepsilon - \varepsilon_m}{\varepsilon + 2\varepsilon_m} \tag{1.11}$$

The equation (1.11) is the complex polarizability of a sub-wavelength diameter NP in the electrostatic approximation, and it is similar to the Clausius-Mossotti relation.[30] In other words, the metal polarizability can be interpreted as the distortion of the oscillating electron cloud induced by the electric field[31]; this physical quantity undergoes a resonant amplification, reaching its maximum value when the denominator quantity $|\varepsilon + 2\varepsilon_m|$ is minimum. The condition, known as Fröhlich condition, to be fulfilled can be simplifies to:

$$Re[\varepsilon(\omega)] = -2\varepsilon_m \tag{1.12}$$

The mode associated to the equation (1.12) is the dipole surface plasmon of the metal NP. For a metallic sphere characterized by a complex dielectric function defined according to the Drude model (equation (1.4) and surrounded by air, the Fröhlich condition occurs at the frequency $\omega_0 = \omega_p/\sqrt{3}$. From the expression (1.5) setting $\varepsilon(\omega) \approx \varepsilon_1 = -2\varepsilon_m$ as the resonance condition, it can be obtain the maximum peak of the LSPR frequency as

$$\omega_{LSPR} = \frac{\omega_p}{\sqrt{2\varepsilon_m + 1}} \tag{1.13}$$

Because the relation between frequency and wavelength is denoted as λ=2πc/ω and replacing the dielectric constant with the refraction index, the wavelength of LSPR can be expressed:

$$\lambda_{LSPR} = \lambda_p \sqrt{2n_m^2 + 1} \tag{1.14}$$

in which λ_{LSPR} is the peak wavelength of LSPR, while $\lambda_p$represents the corresponding wavelength to the plasma frequency of the bulk metal.

In the case of a AuNP, with a diameter smaller than $\sim 30nm$, in water ε_m=1.77 and considering ε_m a constant and real parameter, the equation applied to the real part of ε: $\varepsilon_1 + 2\varepsilon_m = 0$, leads to $\varepsilon_1 = -3.54$. From the plot in **Figure 1.2** it is easy to observe that this condition implies a plasmon resonance centered at $\lambda_{LSPR} = 520nm$. If the AuNP was in air, the plasmon resonance would be at $504nm$.These calculated values for the plasmon resonance in water or air correspond closely to the experimental values of spherical AuNPs.

However, for larger AuNPs (starting from 30nm diameter), this dipolar approximation is not sufficient, because significant higher order multipolar modes emerge, and more complex models, such as Mie theory[5, 28, 32-33], accounting for retardation effects, are required. In a seminal paper, Mie in 1908[34] in order to find a physical explanation of the red-purple color of colloidal AuNPs in solution, which at the time had not yet been theoretically investigated, conceived a revolutionary theory of EM radiation absorbed or scattered by a sphere.

Above expression (1.9) and (1.10) leads to the calculation of internal field and dipolar field of NP:

$$\mathrm{E}_{in} = \frac{3\varepsilon_m}{\varepsilon + 2\varepsilon_m} E_0 \tag{1.15}$$

$$\mathrm{E}_{out} = E_0 + \frac{3n\,(n \cdot p) - p}{4\pi\varepsilon_0\varepsilon_m} \frac{1}{r^3} \tag{1.16}$$

As predicted, the resonance in the polarizability value α (1.11), also induces a resonant enhancement of both the internal E_{in} (dielectric confinement) and dipolar fields E_{out}, which occurs under the Fröhlich condition.

1.4 Optical Cross Sections

However, in order to proceed one step further and calculate the intensity of light being scattered or absorbed, the electrostatic model has to be implemented to take into account that light is a wave and not a static electric field. Upon interaction with the NP, light is absorbed (absorption cross section σ_{abs}) and scattered (scattering cross section σ_{scatt}). As a result, the beam going through a NP undergoes an extinction characterized by the extinction cross section (σ_{ext}).

The three cross sections are linked by the simple relation[35]:

$$\sigma_{ext} = \sigma_{abs} + \sigma_{sca} \tag{1.17}$$

The extinction cross section provides a measure of the total power subtracted from the incident wave (by both absorption and scattering processes) over the total power transported by the incident EM wave.

These phenomena are strongly frequency dependent and, therefore, time dependent, and the representation of an ideal dipole is no longer valid. It is necessary to consider an electric dipole that is oscillating in time.

In particular, under plane-wave illumination with $E(r,t) = E_0 e^{-i\omega t}$, the induced harmonically oscillating electric dipole is $p(t) = \varepsilon_0 \varepsilon_m \alpha E_0 e^{-i\omega t}$, with α given by the electrostatic result (1.11). The model of the radiating dipole allows for calculating the absorption and scattering cross sections[35] and links them to α:

$$\sigma_{abs} = k \,\mathrm{Im}[\alpha] \tag{1.18}$$

$$\sigma_{sca} = \frac{k^4}{6\pi}|\alpha|^2 \tag{1.19}$$

The above equations, substituting the polarizability α, the wavenumber $k = 2\pi/\lambda$ and the sphere volume $V = \frac{4}{3}\pi a^3$, become:

$$\sigma_{abs} = \frac{18\pi V {\varepsilon_m}^{3/2}}{\lambda}\frac{\varepsilon_2}{|\varepsilon + 2\varepsilon_m|^2} \tag{1.20}$$

$$\sigma_{sca} = \frac{24\,\pi^3 V^2 \varepsilon_m^2}{\lambda^4}\left|\frac{\varepsilon - \varepsilon_m}{\varepsilon + 2\varepsilon_m}\right|^2 \tag{1.21}$$

The $\sigma_{sca} \propto V_{NP}^2$, and $\sigma_{sca} \propto 1/\lambda^4$ (Rayleigh scattering); while $\sigma_{abs} \propto \mathrm{V}_{NP}$. For a metal NP (radius = a), immersed in a homogeneous medium, the relationship between the two cross sections is:

$$\sigma_{sca}/\sigma_{abs} \propto (a/\lambda)^3 \tag{1.22}$$

In the quasi-static approx. ($a \ll \lambda$), the scattering (which scales with a^6) is negligible compared to the absorption (which scales with a^3). The two effects become comparable for Au NPs of about 50 nm, and scattering prevails above 70-100 nm. This implies that for small NP, the extinction cross section, defined as follow[5]:

$$\sigma_{ext} = 9\frac{\omega}{c}\varepsilon_m^{3/2}V\frac{\varepsilon_2}{[\varepsilon_1 + 2\varepsilon_m]^2 + \varepsilon_2^2} \tag{1.23}$$

it strictly depends on the absorption process: $\sigma_{sca} \ll \sigma_{abs} \approx \sigma_{ext}$. By increasing the radius of the NPs, on the contrary, the scattering process becomes predominant (**Figure 1.4**).

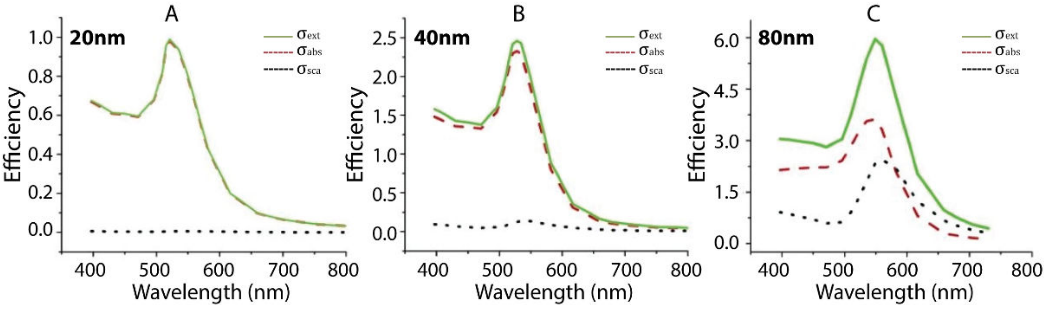

***Figure 1.4** – Comparison of the extinction σ_{ext}, absorption σ_{abs} and scattering σ_{sca} efficiencies as a function of AuNPs diameter. For NPs of 20 nm diameter (A), and 40 nm (B) absorption prevails, while for 80 nm NP, scattering and absorption are comparable. (C). Adapted from [36].*

A proper calculation within the discrete dipole approximation formalism has been conducted by El-Sayed and coworkers [36] and shows that for 20 nm AuNP, no scattering occurs and the NPs only absorb radiation. For larger NPs scattering dominates (see **Figure 1.4**). Therefore, depending on the application it is possible to choose the most suitable AuNPs size. For biomedical applications where AuNPs have to be used as markers, it is mandatory to work with brilliant NPs, so it is appropriate to choose AuNPs with a large diameter (d ≫40 nm). Indeed, AuNPs with d=40 nm have a calculated molar absorption coefficient ε of 7.66 × 109 M^{-1} cm^{-1} at λ_{LSPR}=528 nm, that is five orders larger than the molar extinction coefficient for indocyanine green (ε = 1.08 × 104M^{-1}.cm^{-1} at 778 nm), a NIR dye used in theranostic[37-39]. On the contrary for PPTT where AuNPs must act as nano sources of heat[20, 40-41], is important to deal with AuNPs characterized by high absorption cross section, so AuNPs with a relative small diameter ($D \ll 40nm$), since the Au-NPs photo-induced thermal response is dictated by the absorption (see Chapter 2).

From equation (1.23) it is evident that: (i) the plasmonic properties of any material are defined by its ε(ω); (ii) σ_{ext} scales with NP volume; (iii) σ_{ext} is maximum when the denominator is minimized, in other words, the Fröhlich condition (1.12), defines the LSPR position. Clearly, the frequency of the LSPR is tunable by changing the $\varepsilon_m(\omega)$ of the surrounding medium, but it is also strongly affected by NP size, shape, and composition, as discussed in the next section.

1.5 Experimental parameters shifting the LSPR of AuNPs

In most of the applications, which involve the use of AuNPs, it is often necessary to tune the LSPR wavelength. This is the case, for example, in the field of PPTT where the excitation of AuNPs through the human skin requires a light source operating in the biological window (650–900 nm)[10, 42-45]. Another case among many others is the use of AuNPs, in sunlight driven smart photonic devices (i.e. smart window) or water disinfection applications: it might be necessary to work with broadband-light absorbing AuNPs[46-49]. A further example is represented by the case in which the NPs are exploited as chimeric agents for theranostic applications[50], in which to carry out the detection part it is necessary that the AuNPs work at suitable wavelengths to realize the in-vivo imaging.

The plasmon band of AuNPs strictly depends on various parameters such as their size, shape, geometry, metal composition, nature of the dielectric environment, and the electronic interactions between the stabilizing ligands with NPs[51]. By changing these parameters, the plasmon band can be tuned in terms of wavelength, and intensity. In the following three paragraphs, the main effects deriving from changes in size, shape, and chemical surroundings are studied.

1.5.1 Size effects

To understand the NPs size impact in a clear way, the general approach must be distinguished into two regimes such as small NPs having sizes smaller than the incident light wavelength and large NPs with the size comparable to the light wavelength. As theoretically explained previously, small NPs whose radius is up to 50nm, can be efficiently described by a dielectric dipole. In such case, acting on NPs size mainly affects the width and the intensity of the plasmon band, while the shift in the λ_{LSPR} is almost negligible as shown in **Figure 1.5 B**.

Furthermore, it is worth specifying that, in order to study the effects induced by size change in this range, it is necessary to differentiate between intrinsic and extrinsic size effects. Intrinsic size effects are due to the modification of the metal optical constant when AuNP size is below 30 nm. In particular, the free electron scattering at the NP surface is no longer negligible when the conduction electron mean free path (~30 nm for Au) becomes comparable to NP size. In order to better explain the underlined mechanism, it is useful to introduce the quality factor Q_{LSPR} that gives quantitative information about the LSPR intensity[52]:

$$\mathrm{Q}_{LSPR}(\omega) = -\frac{Re[\varepsilon_{Au}(\omega)]}{Im[\varepsilon_{Au}(\omega)]} \tag{1.24}$$

While $Re[\varepsilon_{Au}(\omega)]$ describes the resonance frequency of a plasmonic system, $Im[\varepsilon_{Au}(\omega)]$ describes its losses, that limit the persistence of plasmonic oscillation. Losses result from several processes, including electron gas confinement, radiative damping, structural imperfections, and metal heating losses[53].

The intrinsic size effect is responsible for the increase Im[εAu], and thus the decrease of Q_{LSP}, and it appears as damping of the LSPR band for decreasing NP size. Indeed, LSPR quenching is almost total in AuNPs smaller than 2 nm.

The extrinsic size effect, is a retardation effect and is a bare EM phenomenon, appears in the optical absorption spectrum as broadening and redshift of the LSPR for increasing Au NP size[52], and is more evident in AuNPs bigger than 50nm.

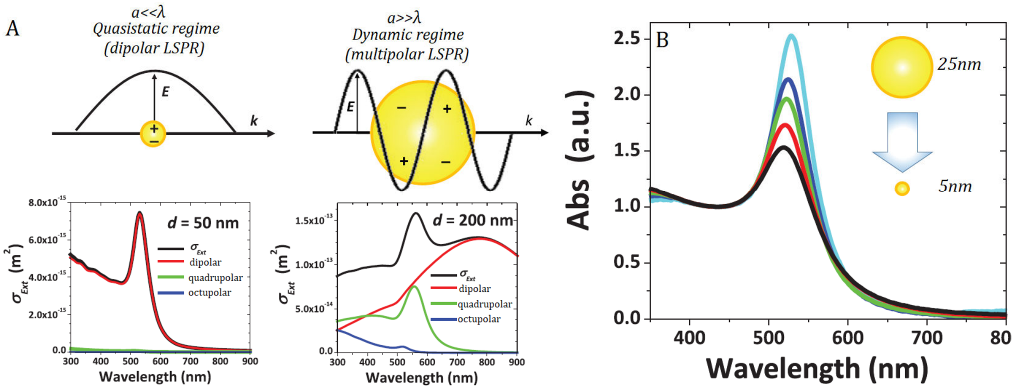

Figure 1.5 *– (A)Contribution of dipolar (red), quadrupolar (green), and octupolar (blue) LSPR to the σ_{Ext} (black) in Au NPs with a size of 50 and 200 nm. (B) LSPR broadening and damping in Au NPs with size decreasing from 25 to 5 nm. Adapted from* [52].

On the other hand, AuNPs with radii greater than 50 nm, cannot be described simply in terms of dipole approximation due to the nonnegligible dimensions compared to the wavelength. Therefore it becomes necessary to consider multipolar terms, which lead to the formation of multiple plasmonic bands, characterized by different peaks (two peaks for quadrupole, three peaks for an octopole). **Figure 1.5 A** shows the contribution of the various terms to the extinction cross section of Au NPs (with size of 50 and 200nm). It is evident that the quadrupolar and octupolar term can be neglected for Au NPs with radius below 50 nm.

1.5.2 Morphology effects

As explained in detail in the previous paragraph, increasing the AuNPs diameter could shift the plasmon resonance, but with nanosphere, one can hardly shift the resonance above 600 nm. Furthermore, the size of AuNPs cannot be arbitrarily increased for some application, in particular for biomedical application, in which the smaller the AuNP is, the more it can be easily internalized in cancer cells[54], and cross biological barriers[55] and reach the target site for localized therapy or deliver specific drug.[56]

The other strategy, to shift the λ_{LSPR}, consists in deviating from a spherical shape. To substantially red-shift the λ_{LSPR} it is convenient to act on the aspect ratio (length divided by width) of the AuNP, using nanorods (AuNRs or GNRs) or discs for instance. By changing the axes lengths the λ_{LSPR} can be tuned from $\lambda = 500$ nm up to the NIR range [42].

The morphological changes of the AuNPs, thanks to the advances in nanochemistry, can go even further, up to the most exotic forms. Nowadays it is possible to synthesize AuNPs with a plethora of different geometries, such as nanoshells (NSs), nanowires, nanocubes, nanostars, nanotriangles, and nanocones, just to mention a few (**Figure 1.6**) [10, 57-58]. Significant examples are the core–shells and NRs, whose λ_{LSPR} can be tuned away from the intraband transitions of Au, thus neglecting the losses and improving the Q_{LSPR}[36]. This category of AuNSs, a type of spherical NPs consisting of a dielectric core which is covered by a thin Au shell, was introduced by Naomi Halas in the late ’90s[59].

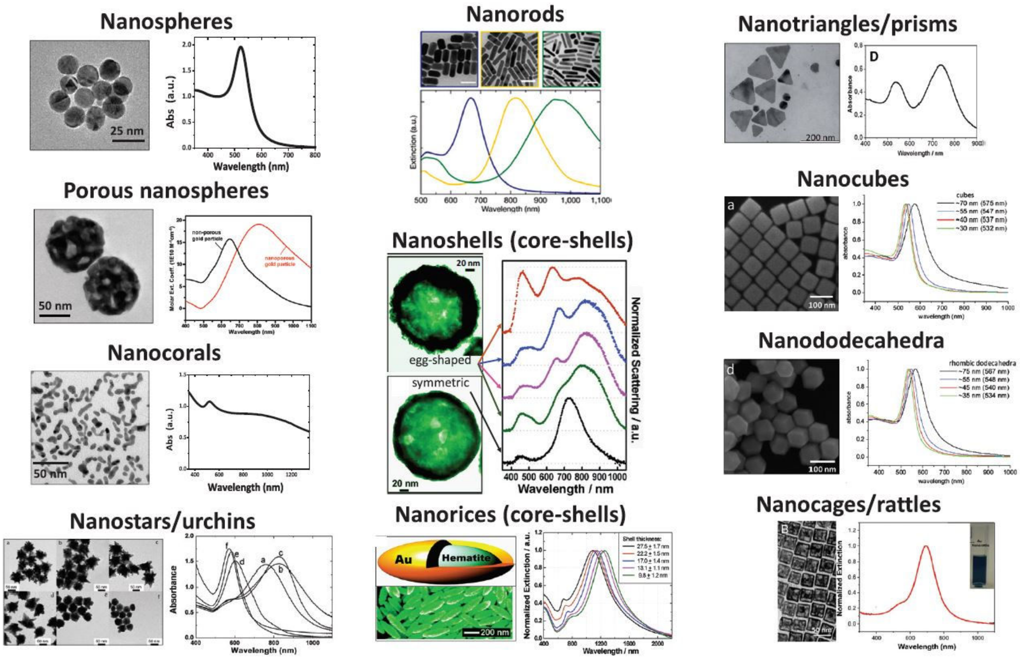

Figure 1.6 *– Au NPs with different shapes along with their corresponding optical and morphological characterization. Images adapted from review [52].*

In order to explain shape effects, AuNRs are the best example[60]. Richard Gans further extended the Mie theory, to include spheroidal NPs of any aspect ratio in the small NP approximation. In the Gans theory, the absorption is mainly related to the aspect ratio of the NPs and not on the absolute dimensions.

Both the polarizability and the dipole moment are described as function of a geometric factor L_i [35]:

$$\alpha_i = -\frac{V_e}{4\pi} \times \frac{\varepsilon - \varepsilon_m}{\varepsilon_m + L_i(\varepsilon - \varepsilon_m)} \tag{1.25}$$

$$p_i = \varepsilon_m \alpha_i E_0 \tag{1.26}$$

V_e is the volume of the ellipsoids given by: $V_e = \frac{4\pi}{3}abc$, with a, b and c being the semiaxes of the ellipsoids. For simplicity, we will consider revolution ellipsoids with two equal axes.

The absorption cross section for a prolate spheroid (rod-shaped NP) is found analogous to that of the spherical NPs, as [32]:

$$\sigma_{ext} = \frac{\omega}{3c}\varepsilon_m^{3/2} V \sum_j \frac{(1/P_j^2)\varepsilon_2}{\left[\varepsilon_1 + [(1-P_j)/P_j]\varepsilon_m\right]^2 + \varepsilon_2^2} \tag{1.27}$$

Where P_j are the depolarization factors along the axes, they are described as functions of the aspect ratio R and eccentricity e of the corresponding ellipse along axis i.

$$\mathrm{P}_a = \frac{1-e^2}{e^2}\left[\frac{1}{2e} ln\left(\frac{1+e}{1-e}\right) - 1\right] \tag{1.28}$$

$$\mathrm{P}_b = \mathrm{P}_c = \frac{1-\mathrm{P}_a}{2} \tag{1.29}$$

$$e = \left[1 - \left(\frac{b}{a}\right)^2\right]^{1/2} = \left(1 - \frac{1}{R^2}\right)^{1/2} \tag{1.30}$$

For a sphere (a = b = c), the three resonances are equal, so the depolarization factors correspond to 1/3. In this case, it is easy to check that equation (1.25) gives the polarizability of the electrostatic model of relation (1.11).

Importantly, the LSPR occurs at the condition that minimizes the denominator of equation (1.27):

$$\varepsilon_1 = -\left[(1-P_j) \times \frac{\varepsilon_m}{P_j}\right] \tag{1.31}$$

and again, like for the Fröhlich condition (1.12) for a spherical AuNP, the absorption, scattering, and extinction cross sections are significantly enhanced under resonance conditions.

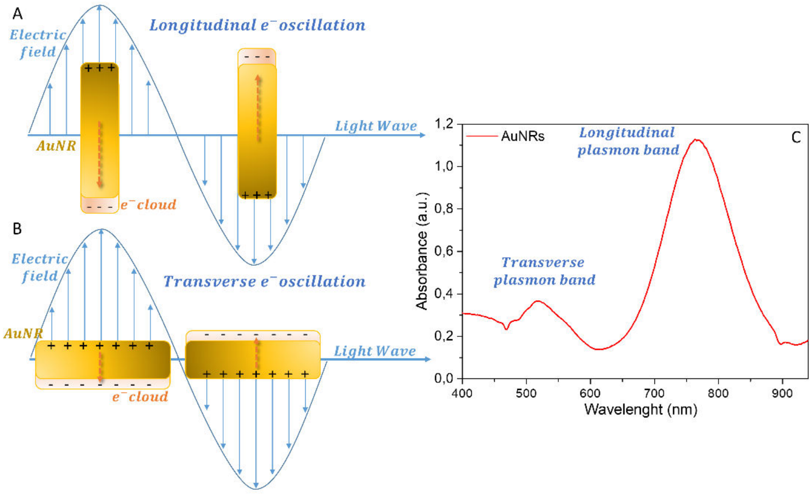

Figure 1.7 *– (A, B) Charge accumulation for longitudinal and transversal LSPRs in AuNRs. The longitudinal and transverse oscillations of electrons result in different plasmon bands (C).*

As shown in **Figure 1.7**, for a AuNR, the charge accumulation and the electron oscillations at the surface, is different along the rod axis (longitudinal plasmons) and along a perpendicular direction (transversal plasmons). A direct consequence is that the extinction spectrum consists of two peaks, one matching the transverse plasmon mode and the other matching the longitudinal plasmon mode. The first band, caused by the excitation along the minor axis, is slightly blueshifted with respect to the LSPR in an equivalent sphere, while the second band, caused by the excitation along the major axis, is redshifted and more intense, since Q_{LSP} increases with wavelength.

When R increases, the transverse plasmon band occurs almost on the same position as for spherical NPs, the resonance of longitudinal plasmons shifts towards longer wavelengths. Indeed, the wavelength of the longitudinal plasmon absorption (λ_{LSPR}^{L}) is almost linearly dependent on the aspect ratio R and the dielectric constant ε_m.[61] For example, from the result by El-Sayed et al., the maximum peak of the longitudinal band displayed a red shift from 650 to 800 nm after altering R from 2.6 to 3.6.[61]

1.5.3 Physical-chemical environment effects

The spectral response would also rely on several other factors, such as the local medium surrounding the AuNP. Following the equation (1.12), a change in ε_m corresponds to a change in the LSPR frequency of AuNPs (in a non-absorbing matrix $\varepsilon_m = Re[\varepsilon_m] = \varepsilon_1$). The surrounding medium, through its refractive index n connected to the dielectric permittivity: $\varepsilon_m = n^2$, represents a fundamental parameter in determining the LSPR.

Since $\varepsilon_1$decreses versus wavelength (see **Figure 1.2**), equations (1.13), (1.14) imply that the LSPR is redshifted for increasing ε_m (i.e. going from water to glass) and blueshifted for decreasing ε_m (i.e. going from water to air). It is not surprising that the surrounding medium plays such a dominant role in determining LSPR, considering that LSPR phenomena occur on the AuNP surface. Indeed, due to the nanometric size of NPs, i.e. to the large fraction of surface atoms over the total, the LSPR position is very sensitive to the environmental dielectric properties, such as changes in liquid or gas density, change in LCs director orientation[62], formation of organic shells such as those of stabilizing ligands, and in general to any surface adsorption of chemical compounds[22]. This interesting property can, therefore, be suitably exploited for a dual function, both to detect chemical-physical changes in the host medium, but also to implement an active control (i.e. dynamic modulation)[62] of the LSPR by exploiting smart materials (such as LCs, hydrogel, etc.), as illustrated in the following chapters.

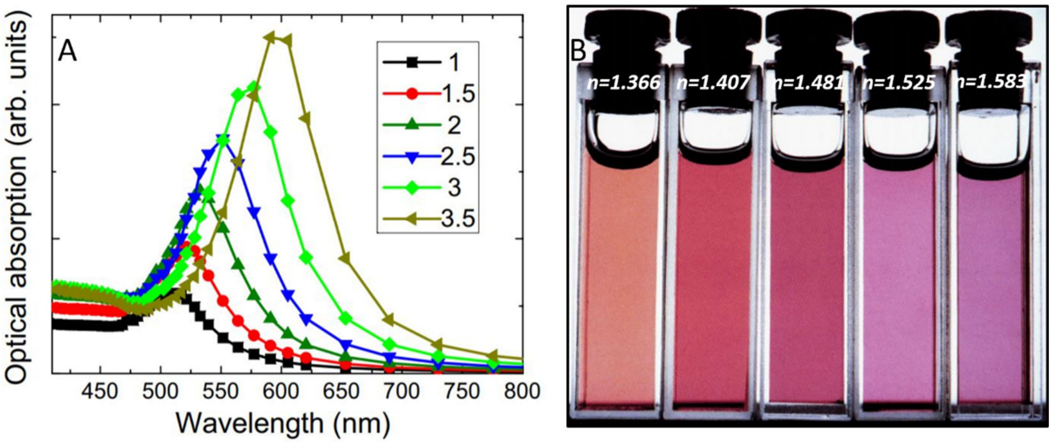

Figure 1.8 *–.(A) LSPR bands for 10nm Au in a dielectric medium with different dielectric functions calculated according to Mie theory.*[63] *(B) Color variation of colloidal AuNPs solutions from pale red to violet, induced by changing the solvent refractive index.*[64]

Figure 1.8 A shows the absorption spectra for 10 nm size spherical AuNPs surrounded by media with different dielectric functions. The surrounding medium does not affect the bandwidth, that is mainly related to the NP size, but significantly modifies the resonance intensity that increases as the ε_m increases.[63] This, and also the λ_{LSPR} redshift, are the expected behaviors for a forced oscillator. As ε_m increases, the total NP surface charge decreases, causing the restoring force to decrease. From classical physics, it is well known that reducing the restoring force leads to: (i) smaller resonant frequency (larger wavelengths), and (ii) higher resonance amplitude. Mathematically this is evident from equation (1.23), from the relationship $\sigma_{abs} \propto \varepsilon_m^{3/2}$. **Figure 1.8 B** shows the change in color of different colloidal AuNPs solutions dispersed in water from pale red to violet with respect to the change in refractive indices of surrounding media. This behavior indicates that dispersion of similar NPs in different dielectric media such as water, ethanol and other transparent oxide matrices leads to a remarkable shift in the λ_{LSPR} of NPs.

The high σ_{ext} and the possibility to modulate the LSPR in response to a change of the surrounding chemical environment make the Au NPs an excellent signal transducer, widely used for the development of sensors [65]. Sensing of chemical and biological species using plasmonic AuNPs has received considerable scientific attention with important implications in the field of environmental sciences, diagnostics, and medicine [66] Besides, optical extinction in NP ensembles can be probed with UV-Vis spectrometers that are present in most laboratories, without altering the sample, and the registration of the spectrum requires short times [22]. Looking at the equation (1.14), it is possible to find an approximated linear relationship between the LSPR maximum (λ_{LSPR}) and the environment refractive index.

Chapter 2

BASICS OF THERMO-PLASMONIC HEATING

The localized surface plasmon resonance (LSPR) is an efficient way to confine energy on an extremely small scale, thus drastically enhancing both absorption and scattering cross-sections of an AuNPs.[67] While the scattering cross section tells how energy is re-radiated by the NP in the form of light, the absorption cross section suggests how the absorbed light is re-emitted in the form of heat. Thus, absorption is what primarily matters in thermoplasmonics[20], the domain of nanoplasmonics that uses plasmonic NPs as nanosources of heat. Taking advantage of this light-to-heat conversion provides access to an innovative way of studying and controlling heat-induced phenomena at the nanoscale. In this chapter, it is discussed how the plasmonic properties can turn AuNPs into efficient nano-sources of heat. The first part of this chapter shows the photo-induced generation of thermal energy within and around AuNPs, by providing the basic principles and considering cases useful for some applications. Then temperature arising from bulk medium containing AuNPs is examined.

2.1 Physics of Plasmonic Heating

The LSPR absorption is an efficient and fast way of inputting energy into the AuNP by macroscopic light excitation, the inner exchange mechanisms then allowing this energy to be mainly converted into heat at the nanoscale. In order to gain a deeper insight into these processes, it must be considered that the optical properties of such nano-objects are governed by a series of energy exchanges, each of them characterized by a typical time scale[67] (**Figure 2.1**).

After the interaction with an incident light (i.e. a “very short” light pulse) in the visible spectral domain, the AuNPs gain energy by absorbing photons through electron transitions. If the frequency of the incident radiation matches the LSPR band, a resonant coupling with the EM wave occurs, with consequent excitation of the plasmon resonance (**Figure 2.1 A**); this triggering of phenomena manifests itself in a collective, coherent, and dipolar electronic oscillation in the conduction band. The result is a global non-equilibrium condition of the electronic distribution, with some electrons absorbing photonic energy and others remaining unexcited. In order to restore the internal thermal equilibrium of the electron conduction band, the energy is redistributed, through electron-electron collisions (e-e), inside the quasi-free electronic gas. This process, which does not involve loss of energy acquired by photons, occurs on a time scale of approximately $10fs \leq \tau \leq 100fs$, based on the total energy introduced into the system. Subsequently, the energy of the hot carriers is redistributed with a relaxation process (**Figure 2.1 B**), through electron-phonon scattering (e-ph), on a time scale of $100fs \leq \tau \leq 1ps$. The last step takes into account the medium surrounding the nanoparticle, and the transfer of thermal energy to the interface, via phonon-phonon collisions (ph-ph), on a $10ps \leq \tau \leq 10ns$ time scale. This last process (thermal dissipation, **Figure 2.1 C**) leads to the cooling of the AuNP which releases heat to the surrounding medium, causing its temperature to rise. The dynamics of this process (see below) strongly depend on the heat transfer properties of the surrounding medium.[68]

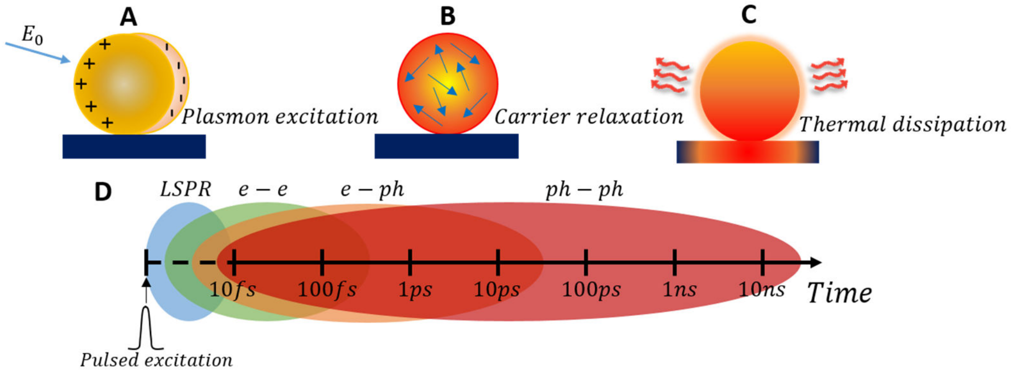

Figure 2.1 *– Schematic illustration of (A) photoexcitation of LSPR, (B) relaxation of photoexcited LSPR, (C) releases of thermal energy to the surrounding medium. (D) Energy transfers involved in the PPT response of AuNPs on a logarithmic time scale.*

To summarize, the effect of this series of energy transfers (**Figure 2.1 D**), is that the internal energy of the electron gas subsequent to photon energy absorption goes through (i) a rapid and resonant enhancement (*LSPR*), (ii) a confined electron gas redistribution (*e-e*) (athermal regime), (iii) a fast decrease (*e-ph*) and (iv) a slow recovery of the initial state of equilibrium (*ph-ph*) (heat transfer to the surrounding medium).

It is worth pointing out that this light-absorption-triggered nanoscale heating of AuNPs, should be carefully calibrated in applying the photothermal effect to bio-related applications[68]. If the AuNP heating, triggered by the absorption of light is much faster than the cooling by the surrounding medium, the photothermal heat confined within the AuNP lattice can lead to structural changes of AuNPs, such as ablation, melting, or reshaping[68]. At the same time, the ideal condition for photothermal-based biomedical applications is a slower rate of energy accumulation relative to AuNP cooling so that the temperature inside the AuNP is efficiently transferred to the AuNP surrounding medium.

Therefore, the AuNP thermal dissipation toward its close environment must be thoroughly analyzed to use gold NP as photo-induced heat nanosources [67]. It is easily understandable, for instance, that the higher the thermal conductivity of the surrounding medium, the faster the relaxation and the lower the temperature at a given distance from the AuNP.

The athermal regime (e-e collisions), closely related to the out-of-equilibrium state for the conduction electrons, occurs in a short time interval after excitation. After the thermal equilibrium phase, the energetic couplings within the AuNPs and with their environment can be treated by classical thermodynamics approaches. In many cases, like the studies reported herein, the athermal regime can be disregarded, as in the experiments the time scale under consideration is much larger than the athermal regime duration.

In particular, in order to study the heating generated from the AuNPs, it is possible to use a steady state regime for the excitation since for CW laser beams, the photo-absorbed energy input is slow against the typical lifetimes of these off-equilibrium states. This steady-state analysis has been carried out by different authors.[41, 69-70] For this, the energy absorbed is considered as entirely converted into heat and the electron excitation and the e-ph coupling can then be disregarded.

The heat source term $Q(\mathbf{r}, t)$ is calculated by evaluating the power density of the electromagnetic field absorbed in the NP. This first step can be performed through a simple approach when the field in the NP can be analytically calculated; (i.e. for an isolated AuNP in the stationary regime λ>>d, see Chapter 1), by calculating the absorption cross section. In this particular case, the total power of heat generation Q can be easily expressed considering the σ_{abs}:

$$Q = \sigma_{abs}\, I \tag{2.1}$$

where $I = nc\varepsilon_0 E_0^2/2$ is the irradiance of the incident plane wave (W/cm^2), c is the speed of light, and E_0 is the amplitude of the external electric field. This approach enables to simple calculate σ_{abs} analytically, which is the case for a sphere or an ellipsoid amongst others. For more complicated geometries, a numerical model is required to evaluate Q.

2.1.1 Heat power density distribution

In order to settle the theoretical background of thermoplasmonics and to derive the main physical underlying rules that govern a temperature field generated by AuNPs, it must take into account that metals are not ideal conductors, at optical frequencies. Thus, there are different damping mechanisms for the LSPR phenomenon in AuNPs, like the aforementioned e-ph collision. This damping exerted on the free electron gas oscillating inside the AuNPs results in heat generation via the Joule mechanism.

To explore this process, we consider a metallic NP interacting with a monochromatic light source at the angular frequency $\omega = k_0 c$.

In the following, let specifically consider a common experimental case where the NP is surrounded by water. The electric field is $E(r,t) = Re\{E(r)\, e^{-i\omega t}\}$, with $E(r,t)$ its complex amplitude.

The external radiation produces Joule heating on the AuNP yielding a heat power density $q\ (r,t)$, at any time t and any location r, given by [20]:

$$q(r,t) = J(r,t) \cdot E(r,t) \tag{2.2}$$

where J is the electric current density (charge per unit time and area) inside the NP. Using the complex-number formalism, (2.2) reads:

$$q = \frac{1}{4}\left(J \cdot E\, e^{-2i\omega t} + J^* \cdot E^*\, e^{2i\omega t} + J^* \cdot E + J \cdot E^*\right) \tag{2.3}$$

Since, the oscillations of q at the angular frequency ω are much faster than any subsequent effect observed in thermoplasmonics, from now on, it will be used the time average $\bar{q}(r) = \langle q\,(r,t)\rangle_t$, instead of the time-dependent quantity $q\,(r,t)$. Note that $\langle e^{2i\omega t}\rangle_t = \langle e^{-2i\omega t}\rangle_t = 0$. Thus, from (2.3), one gets:

$$\bar{q} = \langle J(r,t) \cdot E(r,t)\rangle_t = \frac{1}{4}(J^* \cdot E + J \cdot E^*) = \frac{1}{4}Re(J^* \cdot E) \tag{2.4}$$

The relations $J(r) = \partial_t P = i\omega P(r)$ and $P(r) = \varepsilon_0(\varepsilon_m - 1)E(r)$ permit to express the heat power density $\bar{q}$ as a function of the inner electric field from the previous equation:

$$\bar{q} = \frac{\omega}{2} Im(\varepsilon_m)|E(r)|^2 \tag{2.5}$$

where $\varepsilon_m$is the metal permittivity. The heat power density $\bar{q}$ within a NP is thus proportional to the square of the amplitude of the electric field inside the NP. The electric field inside the NP can be easily expressed in terms of the external electric field through the expression:

$$E = \frac{3\varepsilon(\omega)}{\varepsilon(\omega) + 2\varepsilon_m} E_0 \tag{2.6}$$

The total heat power Q delivered by an AuNP can be obtained integrating q over the AuNP volume:

$$Q = \frac{\omega}{2} Im(\varepsilon_m) \int_V |E(r)|^2 \tag{2.7}$$

The expression (2.7 shows that the quantity of the generated heat is governed by the electric field intensity within the metal. Consequently, the heat power density distribution strongly depends on the NP size and shape[11].

In order to investigate numerically the heat generation in AuNPs, Baffou et al.[11, 70], have taken in consideration different NPs shapes, assigning at all nanostructures the same volume, in order to focus specifically on morphology effects. Their work allows the possibility to map the spatial distribution of $\bar{q}$ inside the AuNPs, explaining in detail the origin of heating as a function of the morphology, progressively deforming an Au-sphere into a rodlike geometry, at a constant volume. **Figure 2.2 A** displays calculations of heat power spectra Q for different geometries of colloidal AuNPs surrounded by water (n=1.33, to mimic physiological environments) and illuminated by a plane wave (I=1mW/μm^2=10^{5}W/cm^2). Two fundamental properties arise from the calculations, in addition to the theoretically expected LSPR redshift as the AR increases (see 1.5.2), a considerable enhancement in the heating efficiency occurs (60% respect to the sphere) (**Figure 2.2 A**).

The reason is clear looking at the 3D mapping of $\bar{q}$ in **Figure 2.2 B**: (i) in the excitation process of the LSPR in a spherical AuNP, the heating generation derives substantially from the incident radiation exposed region of the NP; (ii) for rod-shaped AuNRs, the heating process involves the entire AuNR volume effectively, being the outer and internal region almost attached, which explains the noticeable increase in the heating efficiency.[11]

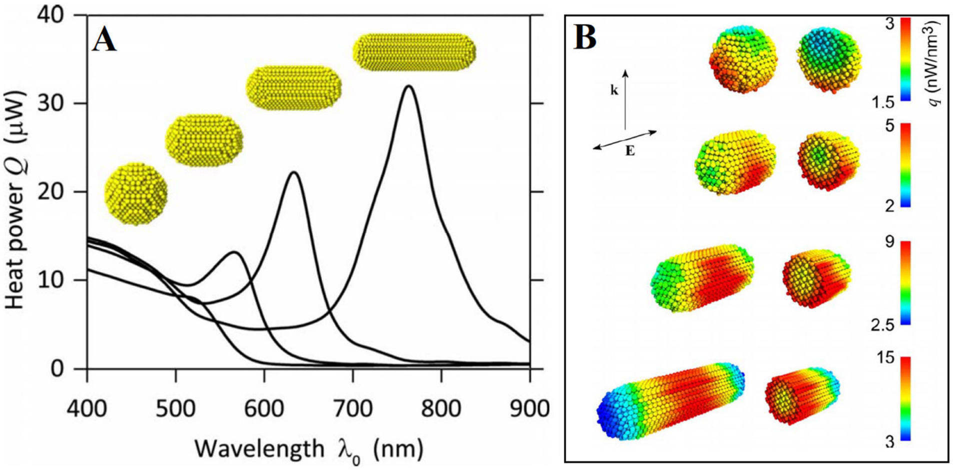

Figure 2.2 *– Heat generation in AuNPs: (A) trend of the heat power with the AuNPs aspect ratio, along with the (B) 3D mapping of the heat power density for different AuNPs of the same volume at their respective LSPR [readapted from [11]].*

The drastic influence of the NP geometry on the photo-thermal conversion efficiency offers some degree of control for designing efficient nano-source of heating, remotely controllable by laser illumination. Note that the maps represented in **Figure 2.2 B** must not be confused to the temperature distribution inside the NP.

2.1.2 Temperature distribution

To derive the temperature [69] around a single AuNP, first, it is necessary to determine the heat sources deriving from the Joule effect; secondly, once we have assumed that no phase transitions occur in the surrounding medium, we can replace the physical quantities determined (heat power density) in the general equations governing the distribution of heat in the surrounding environment and solving the heat transfer equation.[71]

$$\nabla \cdot Q = \langle J \cdot E \rangle_t - \frac{de}{dt} \tag{2.8}$$

Equation (2.8) results from an energy balance: the global amount of thermal energy generated by a single AuNP must be equal to the total amount of thermal energy generation (the ones governed by Joule effect), plus the amount of thermal energy confined inside (AuNP internal energy variation). Considering a medium that can be described by a thermal conductivity $k(r)$, a mass density $\rho(r)$ and a specific heat capacity c(r).

$$\nabla \cdot (-k(r)\nabla T(r,t)) = q(r,t) - \rho(r)c(r)\frac{dT(r,t)}{dt} \tag{2.9}$$

The factor ρc quantifies the ability of a medium to store thermal energy and k quantifies the ability of a medium to conduct thermal energy.

Considering a continuous wave illumination and the steady state regime, since there is no variation in temperature over time, the derivative is zero, so the last term can be erased. For a uniform medium k is constant and the Laplacian operator ∇^2 can be used, so the heating process inside and outside AuNPs is governed by the Poisson equation:

$$k\,\nabla^2 T(r) = -\bar{q}(r) \tag{2.10}$$

A dimensional analysis of this equation permits to estimate the expected temperature spatial variation T throughout the structure, that turns out to be $\delta T \cong 0.1°C$.[11]

Such a small value comes from the very small spatial dimension of the AuNP: at this scale, the thermal diffusion is so fast that, even though the heating power density undergoes strong spatial variations, the temperature diffuses quickly and remains almost uniform. Moreover, thanks to the extremely high thermal conductivity of metals compared with that of the surroundings, the temperature $T(r)$ is kept quasiuniform throughout the metal. In particular, the ratio between thermal conductivity of gold and water is ≈500, indeed $k_{Au} = 318\,Wm^{-1}K^{-1} \gg k_{water} = 0.6\,Wm^{-1}K^{-1}$, in terms of thermal diffusion, heat flows so fast inside the AuNP, compared to the outside medium, that its temperature is nearly uniform for moderate NP size.[70, 72]

The equation (2.10) is valid inside the AuNP, $0 \leq r \leq R_{NP}$ and, conductivity k_0, while in the region $r > R_{NP}$ and host medium conductivity k_H, the equation governing the heat diffusion around the AuNP becomes a Laplace equation:

$$\nabla^2 T(r) = 0 \tag{2.11}$$

The absence of heat production can be validly explained considering that the only heat source of the analyzed system is the plasmon structure.

Under the uniform-temperature approximation[70], the equation (2.10), for a simple case of a spherical AuNP of radius R, produces a profile of temperature increase given by a Coulomb potential outside the AuNP.

$$\Delta T(r) \approx \Delta T_{NP}\frac{R}{r} \qquad r > R \tag{2.12}$$

$$\Delta T(r) \approx \Delta T_{NP} \qquad r < R \tag{2.13}$$

Where ΔT_{NP} is the uniform temperature increase of the AuNP, generated by the total absorption power Q, defined as in the expression (2.1). The actual ΔT experienced by AuNP is dependent on several parameters, namely its absorption cross-section, its shape, the thermal conductivity of the surrounding medium, and the wavelength and irradiance of the incident light.[40]

More precisely, the ΔT of a uniform charged AuNP dispersed in a homogeneous medium with a thermal conductivity k_m, can be calculated by imposing equality between the heat power Q and the integral of the current density $J_{th} = -k_0 \nabla T$ over the AuNP boundary [11], which gives:

$$\Delta T_{NP} = \frac{Q}{4\pi k_m R} = \frac{\sigma_{abs} I}{4\pi k_m R} \tag{2.14}$$

and consequently the equation (2.12 can be written as:

$$\Delta T(r) \approx \frac{\sigma_{abs} I}{4\pi k_m r} \qquad r > R \tag{2.15}$$

The $1/r$ dependence of ΔT outside the sphere leads to an infinite amount of thermal energy stored in the surrounding medium (**Figure 2.3 a, b**). The maximum temperature increase occurs at the NP surface (i.e. at $r = R_{NP}$), and since $\sigma_{abs} \propto V_{NP} \propto R_{NP}$, the maximum temperature is proportional to the second power of the NP radius. The two factors leading to this dependence are: (i) the total heat generation rate inside the AuNP, proportional to the NP volume; (ii) the total heat transfer through the AuNP surface, which turns out to be a growing function connected to the AuNP surface area.[52]

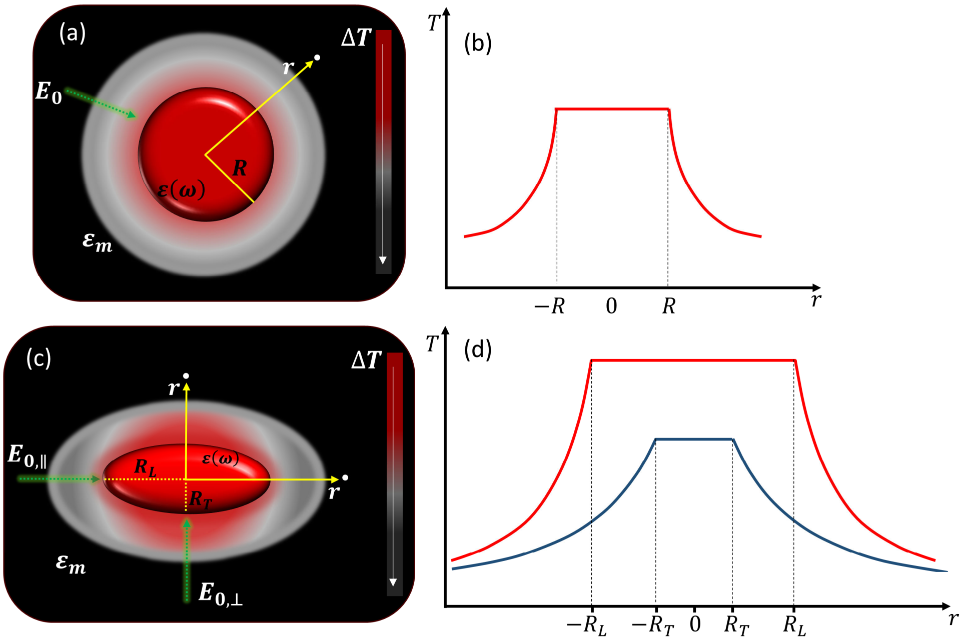

***Figure 2.3** – (a) Schematic of PPT conversion process in AuNPs with radius R, and (c) AuNRs with longitudinal R_L and transversal R_T axes (b) along with its temperature distribution as a function of distance, r, to the surface of the AuNP and AuNR. (d) The red curve, related to R_L, is obtained irradiating the AuNR with light polarized along the longitudinal axis, the blu curve, related to R_T, is obtained irradiating the AuNR with light polarized along the transversal axis.*

The measurement of local temperature at the surface of NPs is very challenging and can be made through monitoring phase transformations of the surrounding matrix [41, 69] (i.e. AuNPs embedded within ice), or with photothermal optical probes,[73] based, for example, on thermoresponsive molecules such as thermotropic LCs[74] or biologically relevant molecules such as DNA[75], where the thermal response of the smart material is known. In the following chapters, the methods used in this thesis work to monitor the temperature directly, at the nanoscale, or indirectly at the macroscale, will be illustrated in more detail.

To give an order of magnitude of ΔT_{NP}, a spherical AuNP in water with a diameter of 20 nm, illuminated at the LSPR (λ = 530nm), with an irradiance of I = 1mW/μm^2 experiences a temperature increase of ~ 5°C.[40]

The validity of the equation (2.15), is not only restricted to spherical AuNPs, indeed can be used also to extract surface temperatures of non-spherical AuNPs, (**Figure 2.3 c, d**), by including a dimensionless geometrical correction factor β in the denominator[76]:

$$\Delta T_{nonspherical} = \frac{\sigma_{abs} I}{\beta \, 4\pi k_m R_{eff}} \tag{2.16}$$

Where R_{eff} is the radius of a spherical shape with a volume identical to that of the nonspherical AuNP. β has been calculated for a large set of AuNPs morphologies with axial symmetry (i.e. rods, ellipsoids, discs) and are reported in the Baffou et al. work.[70] In the uniform-temperature approach, the value of β does not depend on any structure that the NP might have in its interior, for instance, spherical shells behave the same as spheres in this respect, with $\beta = 1$.

Generally, for the AuNPs, the establishment of this steady-state temperature profile is very fast, the characteristic time scale τ_{tr} of the transient regime mainly depends on the characteristic size L of the system (for instance the radius R for a spherical AuNP), but is independent on the temperature increase [69, 77]. If the continuous light source is switched on at time t = 0, the typical time needed to reach the steady state is

$$\tau_{st} \approx R^2/D_H \tag{2.17}$$

where $D_H = k_H/\rho c_H$ is the host medium thermal diffusivity. For water, it equals to 0.14 mm^2/s. Hence, $\tau_{st} \approx 6\,ns$ for a 30nm AuNP in water.[67] Thus, 10 ns -10 μs is the range of characteristic time scales of thermal processes that occur at the nanoscale, independently of the temperature increase.

It is worth underlining that, in all the calculations and observations made previously, the spherical shape for AuNPs has often been considered, although they are not the most efficient light-to-heat converters for the reasons expressed in paragraph 2.1.1. This choice is mainly due to the exceptional thermal stability that characterizes this morphology, and which makes it, in many circumstances, an excellent candidate for biomedical applications. Other AuNP morphologies, which may seem more convenient for such purposes, such as nanostars, suffer from thermal instabilities. Indeed, nanostars although are efficient light-to-heat nano-converters, have thin spikes that suffer from poor thermal stability when subjected to high temperatures and could easily reshape changing their optical properties, thus limiting their use in thermoplasmonics. Spherical shapes are significantly more stable with respect to morphological changes and structural reshaping, and hence, retaining their optical properties unaltered even at high temperatures.[76]

In the following section the mechanism of heat production in AuNPs ensemble is explained in detail.

2.2 From single AuNP heating to collective bulk heating

For photothermal-based bio-applications, it is convenient to know both the single NP nanoscale heating as well as the global temperature resulting from irradiating a known density of plasmonic NPs. When an ensemble of homogeneously distributed AuNPs is involved in the photo induced heating process, it is necessary to consider physical phenomena that are much more complex than those related to the LSPR excitation of a single AuNP.[78] When the AuNPs are immersed in a bio-system a precise prediction of the induced temperature is fundamental, and it's not enough to consider the effect of the temperature increment on individual cells, since all the temperature-induced changes in this kind of environment are intrinsically related by the intensity and the duration of the temperature increment.[79] In bulk photothermal experiments, two temperature regimes are established which operate on different time scales: (i) the nanoscale temperature surrounding the NP, that equilibrates during 100 ns, and (ii) the global temperature for a volume with a radius between 1 and 10 mm, with a characteristic heating time of several hundreds of seconds.

As for nano-scale temperature monitoring, the collective heating from irradiated NPs immersed in a colloidal solution or deposited on a substrate can be readily obtained from bulk measurements by using several methods, like thermal imaging[80] or a simple thermometer. Bulk temperature estimation, therefore, provides a robust readout for the relative photothermal heat generation generated from ensembles of different nanostructures.[76]

Indeed, experimentally, when illuminating several AuNPs dispersed in solution, the temperature profile throughout the system is no longer localized around each NP, because some collective effects can arise.[81]Thus, the global temperature becomes uniform throughout the AuNPs assembly, although the size of the source (the laser beam radius) is nanometric, a situation suited for application such as PPTT.[82]

What has been so far described, is related to heat diffusion in a uniform, infinite medium of thermal conductivity (k_H), experimentally, this corresponds to the case of metal colloids dispersed in a solvent. Another class of experiments is rather based on the use of metal colloids randomly or periodically deposited on a planar substrate. In this case, the thermodynamic problem is more complex. The first problem arises considering that the surrounding medium consists of two media featuring different thermal conductivities[20]. In this case, when the experiment is performed at an interface, such as a glass−water interface, the thermal conductivity of the surroundings can be replaced by an effective conductivity which is the average of the conductivity of the two media $\bar{k} = (k_1 + k_2)/2$.[40] If the heat source is located right at the interface, the temperature profile recovers a point symmetric and reads in any of the two media:

$$\nabla T(r) \approx \frac{Q}{4\pi\bar{k}|r|} \tag{2.18}$$

This important conclusion represents the basis of a current assumption in thermo-plasmonics: when conducting numerical simulations involving plasmonic structures lying on a substrate, one can consider the structures as embedded in a uniform medium of average thermal conductivity, which simplifies a lot the numerical simulations. This is an assumption in the sense that the NPs are not exactly at the interface, as they are standing in the upper medium and not within the substrate.

In general, the heating effect, due to the presence of several AuNPs, undergoes a substantial increase generated by the accumulative effect. In this case, the thermal energy "source" should be written as a sum over all NPs, to take into account the different heat flux contributions associated with each single NP:

$$Q(r) = \sum_i Q_i(r_i) \tag{2.19}$$

where Q_i describes the heat generation by the i^{th} NP located at the r_i position. The more NPs, the stronger the temperature increase that appears in the system. If the intra-particle distance between AuNPs is greater than the AuNPs radius, the heating effect is not affected by the coupling effect.[41]

Baffou et al.[82], derived an analytical expression aimed at calculating the actual temperature increase at the center of a microscopic assembly of AuNPs, another more accurate theoretical model was presented by Pezzi et al.[83]. To address the theoretical problem of calculating the heating effect of AuNPs randomly distributed on a given substrate and surrounded by a known medium, the theoretical model starts from the same assumption made by Baffou, but taking into account a new parameter, the effective thermal conductivity of the entire host system, enabling to accurately determine its value for a generic system. In a system characterized by a huge number of AuNPs (i.e. $\approx 10^{10}$ NPs) homogeneously distributed, every AuNP can be interpreted like a star in the sky for the Olbers' paradox.[83]

The number of AuNPs at a distance r is $N(r) = 2\pi r/d$, grows linearly with r and from equation (2.15) $\Delta T \propto 1/r$, in order to consider the contribution of all AuNPs to the total temperature increase the equation (2.15) needs to be multiply with $N(r)$, obtaining:

$$N(r)\Delta T(r) \approx \frac{2\pi\, Q\, R_{NP}^3}{3\, d\, k_H} \tag{2.20}$$

so the $1/r$ dependence is deleted. Therefore, even the AuNPs located away from the laser beam center provide their contribution to the global temperature variation $N(r)\nabla T(r)$, exactly as in Olber's paradox the global brightness of the sky is dictated by the identical contribution of each single star.

Considering, the intra-particle distance $D \gg R_{NP}$ the coupling effect between AuNPs can be neglected and NPs can be treated ad point-like sources of heat.[69]

With a high number of heat nano-sources at different position a possible solution for the equation (2.19) is of the type:

$$\Delta T(r) = \sum_i \Delta T_i(r_i) = \sum_i \frac{c(\lambda) I(r_i)}{|r - r_i|} \tag{2.21}$$

i indicate the i-th AuNP placed at a position r_i distant $|r - r_i|$ from r and, the parameter $c(\lambda)$ provides the photo-heating effectiveness of the system and is equal to:

$$c(\lambda) = \frac{V_{NP} Im(\chi_{NP})}{2\lambda k_H \sqrt{\varepsilon_H}} \left| \frac{3\varepsilon_H}{2\varepsilon_H + \varepsilon_{NP}} \right|^2 \tag{2.22}$$

where $Im(\chi_{NP})$ is the imaginary part of the electric susceptibility.

The huge number of AuNPs and their homogeneous distribution makes suitable to assume the "continuum" approximation at the macroscale and obtain a simple formula to predict the temperature variations when the material parameters (R_{NP} and I) are known. On the NPs scale, the source density σ varies enormously from point to point, however when dealing with a large scale system (i.e. the beam waist w of the impinging beam) we can consider a surface element $dS = d^2r' = dxdy$ that can be quite small relative to the size of the system, although still large enough to contain many AuNPs. In this conditions, it is allowed to define a continuous source density σ such that $\sigma(r')d^2r' = \sum_i c(\lambda)I(r_i)$ and to change the sum of equation (2.21) into an integral. Therefore, in the bi-dimensional case, in the center of the circular area invested by a Gaussian laser beam, the equation (2.21) becomes:

$$\Delta T(r = 0) = \iint \frac{\sigma(r')d^2r'}{|r - r_i|} = \int_0^{2\pi} \int_0^{w} \sigma dr' d\theta = 2\pi\sigma w \tag{2.23}$$

where it is considered a cylindrical beam with a spatial average intensity I_0 and transversal section of radius w to write:

$$\Delta T(r = 0) = 2\pi\sigma w = 2\pi w c(\lambda) n_{NP} I_0 \tag{2.24}$$

Replacing $c(\lambda)$ expression (2.22):

$$\Delta T(r = 0) = 2\pi w \frac{V_{NP} Im(\chi_{NP})}{2\lambda k_H \sqrt{\varepsilon_H}} \left| \frac{3\varepsilon_H}{2\varepsilon_H + \varepsilon_{NP}} \right|^2 n_{NP} I_0 \tag{2.25}$$

From equation (2.25) several experimentally fundamental information emerge: (i) the temperature variation ΔT, induced by a huge number of AuNPs, is a linear function of the laser intensity $\Delta T = \beta I_0$, (ii) and the angular coefficient β contains the effective thermal conductivity k_H, that as described above, depends on both the substrate and the surrounding medium and that (iii) ΔT can be increased by increasing both the spot size of the laser beam w or the number of irradiated AuNPs, $\pi w^2 n_{NP}$.

As reported in the following experimental chapters, the thermographic analysis enables to evaluate temperature values on the entire area irradiated by the laser beam, empirically verifying the existence of the linear dependence between ΔT and the incident light intensity. This also leads to the simple derivation of the k_H value using a trivial inverse relationship, to deduce the angular coefficient of ΔT plotted as a function of I_0.

This theoretical model is valid for: (i) any collective thermal effect deriving from a huge number of NPs, and for (ii) any NPs spatial distribution that do not allow geometrical simplification, and can be easily extended to a (iii) 3D bulk distribution of AuNPs, thus further expanding its range of applicability.[83]

2.3 Photothermal effects and applications

Due to their large optical cross-section, compared with those of organic dyes commonly exploited for bioimaging and sensing, plasmonic AuNPs have been widely utilized for their light scattering as nanoantenna or contrast agent for surface Raman scattering and optical imaging such as dark-field.[68] In all these circumstances, the absorption of light by AuNPs and the consequent heat generation has long been considered only a side effect, to avoid or to be minimized,[11] and a lot of effort has been channelled towards the compensation of dissipative losses in plasmonic materials.[84] After the first demonstration of AuNP-based photothermal cancer therapy in 2003 by Halas and co-workers[85], the opinion regarding NPs as nano-sources of heat completely changed, turning the material losses into performance gain, exploring new avenues of research based on harvesting and using generated heat. From that moment on, many efforts have been made to translate this preliminary idea into clinical trials. Indeed it was more than clear that exploiting the strong LSPR absorption followed by the fast energy conversion and dissipation could be used promptly for the heating, at the nanoscale, of the local environment by using light radiation with a frequency resonant with the AuNPs LSPR band in order to destroy cancer cells.[86] This effect is at the basis of the PPTT and represents a potentially favourable alternative to traditional treatments of localized tumors such as chemotherapy, radiotherapy, and surgery. Nowadays, the photothermal effect of AuNPs, is widely applied not only for cancerous cells and tumors[8, 42, 87-89], but also to selective destruction of antibiotic resistant bacteria[16, 90-91], drug delivery[57, 92-94], gene therapy[95], and to the treatment of HIV[96]. Very recent applications of thermoplasmonics are involved in the battle against coronavirus. Some examples are mainly devoted to detecting the current pandemic (SARS-CoV-2), enabling a real-time and label-free detection of viral sequences [97-98]; other applications are aimed at realizing nano-based antimicrobial and antiviral formulations that are not only suitable for disinfecting air and surfaces but are also effective in reinforcing personal protective equipment such as facial respirators.[99] It is not surprising such massive use of AuNPs to eradicate viruses, in fact, many studies concerning the treatment of HIV are also reported.[96] Other emerging applications of thermoplasmonics are present also in non-biomedical field, such as energy[100], solar and thermal energy harvesting[101], nanofluidics[102], nanofabrication[103], nano-manipulation[104], heat-assisted magnetic recording (HAMR) for data storage[105-106], photonics and optoelectronics[4]. All these applications, in the most disparate fields, have given rise to the need to monitor the heat induced by the photothermal effect, not only at the nanoscale, but also at the macroscale generated by an ensemble of AuNPs.

PPTT and biomedical applications of thermoplasmonic heating will be extensively described in Chapter 4, with particular emphasis on the application of photothermal heating produced by AuNPs triggered by a suitable light source in the fight against antibiotic resistance and cancer-related diseases. The underlying scientific question behind this research, which represents one of the main objectives of the present work, is to seek a radically new precision medicine protocol to meet longstanding clinical needs for bacteria inactivation and cancer treatments.

Chapter 3

PROBING AND CONTROLLING PHOTOTHERMAL HEAT GENERATION IN PLASMONIC NANOMATERIALS

3.1 Introduction

Experimental research has been focusing on determining the photothermal efficiency of AuNPs immersed in various media, based on the monitoring of temperature changes under light illumination. Temperature measurements are carried out using various techniques, such as thermocouple thermometry [107-109], fluorescent thermometry[110-111], magnetic resonance imaging [112], scanning thermal imaging microscopy[113], and IR thermography[114-116]. Each technique possesses its own strength and weakness. On a nanoscale, mechanical thermal probes, like scanning thermal microscopy, a modified atomic force microscope to map temperatures with 50 nm resolution, require tip contact with the sample to measure the temperature. Optical thermal probes based techniques are noninvasive and benefit from the ability to combine them to ubiquitous optical microscopy, like Raman thermometry[117], photoacoustic thermometry[118],[119]. Particularly interesting is the thermometry method based on the measurement of fluorescence polarization anisotropy, by assessing the molecules' Brownian dynamics directly, enables mapping the local temperature near nanometer-sized heat sources with 300 nm spatial resolution and typical accuracy of 0.1 °C[120]. Another compelling solution for nanoscale heating detection can be obtained by monitoring optical transformations of the AuNPs surrounding matrix, exploiting the thermoresponsive properties of some materials, like thermotropic cholesteric liquid crystals (CLCs).[121] On a macroscale, IR thermography is a contactless, non-destructive, and inexpensive technique, which enables the measurement of the two-dimensional temperature distribution, providing a salient visualization of temperature changes, with sensitivity down to 50 mK (< 0,05 °C) and high spatial and temporal resolution.[115] In some cases, a macro-scale average temperature is not enough and may mask important information. Many fields would benefit from accurate and precise temperature measurements, like electronics, integrated photonic devices, and biology. In biology, temperature governs many vital cellular processes such as metabolism, division, and gene expression. The state of most biosystems can be easily controlled by controlling heating at the single-cell level. Indeed there are several photothermal-induced processes under investigation in literature, thermal-induced unfolding and denaturation of proteins[122], melting of DNA[123], phase transition of lipid membranes and vesicles[124-125], migration or fusion of living cells[126-127], and of course hyperthermia (temperature induced cell death)[79]. A strong limitation to applying AuNPs for hyperthermia for cancer therapy is that for temperatures above 42°C, cell death also occurs in healthy tissues near the tumor site. The main goal of PPTT is to thermally eradicate the tumor tissue without causing damage to the surrounding healthy tissue. Thus there is a clear need to investigate with high sensitivity (less than 0.5°C) the illuminated area's local temperature.[4] Indeed, the analysis performed using a thermal camera, despite its high sensitivity, is limited in spatial resolution. Accurate high-resolution monitoring of temperature could help understand cellular behavior and optimize externally induced procedures, such as PPTT. In the following paragraphs, we will discuss macroscale investigations of bulk temperature via IR thermography. Then it is presented the possibility of employing “smart materials” to study the heating process at the nanoscale. Specifically, the thermosensitive materials chosen to become familiar with the nanoscale thermometry technique are LCs as their spectral characteristics (width and position) can be controlled by changing the system temperature. Subsequently, to exploit the plasmonic heating from AuNPs for PPTT, the hydrogel was selected as the heat-responsive material to get closer to an environment as biocompatible as possible and emulate the physiological cellular environment with a water-based skin-equivalent model.

3.2 Macroscale Thermometer: IR Thermography

Bulk experiments are commonly used in literature to characterize plasmonic NPs and bulk photothermal efficiency. Therefore, and because for many applications, for instance, cancer therapy, the plasmonic NPs are administered at a relatively large concentration, it is relevant to elucidate their collective plasmonic properties.[80] In this thesis, to qualitatively and quantitatively monitor the heating characteristics of a large ensemble of AuNPs nanoheaters, suspended in a solution or stuck on a substrate, we use IR Thermography. Although the human eye cannot perceive infrared (IR) radiation, the IR camera can detect it and convert it into a visual image that represents thermal variations throughout or over a precise region of the sample.[128] Thermography has been proved to be a safe, reliable, sensitive, non-destructive, and non-contacting technique for precisely monitoring bulk temperature variations.[129] It is a versatile technique, which offers a plethora of possibilities, and for this reason, it is perfectly suited to different applications in various fields. In the past few decades, there has been increased interest in active infrared thermography for non-destructive imaging of industrial materials and art objects and medical diagnosis applications. Industrially, thermography is used in military, aerospace, power generation, and automotive industry applications to detect manufacturing and in-service environment-induced defects.[130-131] Recently, research was undertaken to apply thermal imaging in the field of art conservation to examine structures of panel paintings, marquetries, and other art objects for diagnostics and authentication purposes.[132]

Infrared (IR) imaging is based on the fact that any object at a temperature above absolute zero (−273°C) will emit IR radiation, even if only weakly, due to the collisions between molecules within the materials that release energy as photons. The extraordinary ability to detect passive infrared radiation makes thermal imaging cameras an indispensable tool in the field of thermometry.[133] For example, the human body has a low thermal emittance, radiating in a wavelength range that starts around 3μm and peaks in the vicinity of 10μm and trails off from this point into the extreme IR, negligibly, beyond it.[116] In the thermographic-based analysis, the emittance of the object is an important parameter to take into account. The emittance of a surface is defined as a ratio of the radiation flux per unit area of the emitter to that of a blackbody radiator at the same temperature and under the same conditions.[134] In particular, the emissivity of human skin has a known and almost invariant value in this wavelength region (0.98 for black skin and 0.97 for white skin),[135] that makes IR imaging and ideal procedure to evaluate the surface temperature of the human body, and allow to use skin-equivalent models with similar emittance value, for IR thermal evaluation.[134]

In this framework, thermography is receiving growing attention in the medical field. This technique is utilized to detect early caries in teeth with better sensitivity than radiography[136] and bone imaging with the aim of establishing a diagnostic technique for osteoporosis.[137] In breast thermal imaging, an abnormal infrared image is an effective marker for a high risk of developing breast cancer.[138-139] Currently, there is an interest in thermal imaging for fever screening. Following the respiratory "Coronavirus Disease 2019" (COVID-19), caused by the virus "SARS-CoV-2", thermal cameras are being implemented as a means of detecting people with fever-like symptoms in high-traffic areas such as hospital entrances, shopping malls, office buildings, and potentially mass-attendance events.[140]

3.2.1 Thermography for Plasmonic Photothermal Therapy (PPTT)

Thermal cameras have been extensively exploited for in vitro and in vivo temperature monitoring during PPTT. The realization of homogeneous heat distribution and therapeutic temperatures in the deep regions of target tumors has been a major problem in the successful thermotherapy of tumors using conventional thermotherapy systems. Excessive heat generation at the tumor sites can produce burns, blisters, and pain to adjacent normal tissues. Furthermore, an insufficient temperature rise in the deep regions of tumor tissue will result in treatment failure because of intact cancer cells' tumor regrowth.[141] Studies have shown that temperatures above 40 °C are sufficient for hyperthermia due to protein denaturation and temperatures above 85 °C induce conformational changes in DNA, and RNA.[142] Such temperatures would be extreme to use, even in hyperthermia treatment. They would not likely be achieved in cellular experiments, so it is essential to measure temperature increase during in-vivo in-vitro PPT experiments.

Thermography enables determinations of the bulk temperature distribution of colloidal solutions AuNPs dispersed, for example, in a liquid similar to human physiological fluids.[143] Wang et al.[114] recorded IR images of the aqueous suspensions of gold nanohexapods, nanorods, and nanocages, during laser illumination and evaluated their mean temperatures as a function of illumination time. But the technique allows measurements not only for AuNPs dispersed in solutions but also in animal models or 3D models. Maksimova et al.[144] and Terentyuk et al.[145] have measured the temperature distribution in colloidal Au solutions and on the animal skin surface, demonstrating the ability to detect the temperature changes in the interior of biological tissue by using thermograms of its surface. Lòpez-Varela et al. monitored the thermal response of AuNPs, immersed in skin-equivalent phantoms by dynamic infrared thermography, as an infrared imaging tool for realtime recording of the temperature increases (ΔT).[116] More recently, Xiao et al.[146] presented a new method, termed depth thermography, that enables volumetric temperature measurements.

In particular, FLIR camera models (FLIR System, Wilsonville, OR, USA) estimate temperature differences under 0.02 °C (20 mK), by offering quantitative and in-depth measurements to detect deepest body problems or skin in biomedicine.[147] Furthermore, the high performance of the thermal imaging camera depends on the excellent resolution. For example, the model we use FLIR A655sc is characterized by a very high resolution of the images of 640 x 480 pixels, equivalent to 307,200 pixels (i.e., like the simultaneous use of 307,200 IR thermometers or thermocouples). With the current technology, a single thermo-image may contain several thousands of temperature points, recorded in a fraction of a second.[148]

Thermal Radiation Principles

Cerruti et al. [149] presented a method to investigate the infrared emissivity of AuNPs deposited on ITO substrates, monitoring with an IR thermal-camera the response of AuNPs illuminated with a laser light tuned near the LSPR. They exploited the theory behind thermography, which is quite simple and is mainly related to the radiation emitted by a blackbody (a hypothetical perfect absorber and radiator of energy, with no reflecting power, at any wavelength) since IR cameras essentially detect irradiance, not temperature. When AuNPs are irradiated at a frequency that matches the LSPR, they absorb light and relax thermally, emitting IR radiation. Planck's law describes the amount of radiation emitted (or radiant power, W) at any frequency and temperature by a blackbody[150]:

$$W_v = \frac{2hv^3}{c^2} \frac{1}{e^{\left(\frac{hv}{kT}\right)} - 1} \tag{3.1}$$

where $c = 3 \times 10^8 m/s$ is the velocity of light, $h = 6.6 \times 10^{-34} Js$ is the Planck's constant, $k_B = 1.4 \times 10^{-23} J/K$ is the Boltzmann's constant. Actually, when dealing with a real case, the radiation emission from the body represents only a tiny fraction of the radiation emitted by an ideal blackbody. More specifically, real objects' emissivity coincides with the ratio between the radiant power from the object to that from a blackbody under the same conditions of temperature and frequency.

$$\varepsilon_v = \frac{W_{v,O}}{W_{v,b}} \tag{3.2}$$

Moreover, three processes need to be taken into account when dealing with real object temperature measurements. Indeed real materials can absorb α_{ν}, reflect ρ_{ν}, and transmit τ_{ν} light. For each wavelength and frequency, the sum of these three contributions must always verify the following relationship:

$$\alpha_{\nu} + \rho_{\nu} + \tau_{\nu} = 1 \tag{3.3}$$

For AuNPs, which are made up of opaque material, $\tau_{\nu} = 0$ and the relation (3.3 simplifies to:

$$\alpha_{\nu} + \rho_{\nu} = 1 \tag{3.4}$$

According to Kirchoff's law of thermal radiation, for any material, set the temperature and frequency to particular values, the emissivity and the spectral absorbance are the same, that is $\varepsilon_{\nu} = \alpha_{\nu}$. From this, the equation (3.4) for an opaque material can be written as:

$$\varepsilon_{\nu} + \rho_{\nu} = 1 \tag{3.5}$$

ε, is an indicator of a material's capacity to emit (emanate) infrared rays and varies according to the surface properties and material of the object considered: (i) for black bodies maximum emissivity: ε = 1 (100%), (ii) for real bodies ε <1, because not only emit, but they also reflect and eventually transmit radiation; (iii) for non-metallic materials (e.g., PVC, concrete, substances organic) the emissivity is high in the long-wave infrared range and does not depend on the temperature (ε ≈ from 0.8 to 0.95); (iiii) for metals, especially those with a shiny surface, the emissivity is low and varies with the variation of the temperature. So, for highly polished and perfectly reflecting materials (i.e. a perfect mirror), (with ε→ 0), $\rho_{\nu} = 1$. For a graybody radiator (ε <1, and same ε for all wavelengths) the Stefan-Boltzmann formula, obtained by integrating the Planck's formula from $\lambda = 0$ to $\lambda = \infty$, describes the relation between temperature and total emissive power:

$$W_{\nu} = \varepsilon\sigma T^{4} \tag{3.6}$$

which states that the total emissive power is proportional to the fourth power of its absolute temperature and depends on its emissivity.

All metals, including Au, are highly reflective of incident radiation below the plasma frequency, and consequently, ρ_{ν} is quite high and ε_{ν} is close to zero (in fact, ε_{ν} for Au varies between 0.03 and 0.06, depending on surface roughness)[149]. This implies that, even if Au NPs are optimal absorbers at a frequency close to their LSPR, the low emissivity reduces the re-emitted IR radiation as a consequence of the local heating induced by the absorption. This implies that the technique is not suitable for studying the temperature of a single isolated AuNP, but is very well suited to the study of AuNPs dispersed in liquids, biological tissue, or other materials.

The IR thermal camera detects the radiation from the analyzed sample, and the radiation from the environment that is reflected in the sample's surface. Both the emissivity ε (which values can be found in the IR camera manual) and the reflected temperature ρ can be set manually in the camera (often corresponds to the room temperature) since these parameters can dramatically affect the measurement, eventually leading to artifacts and misinterpretation of the temperature real values.

Main components and parameters of an IR thermal camera

An IR thermal-camera basically consists of: (i) a lens, (ii) a detector in the form of a focal plane array (FPA), (iii) a cooler for the detector, and (iv) the electronics and software for processing and viewing thermographic images.[128] Typically, detectors are sensitive to a wavelength range (900–14,000 nm or 0.9–14μm) narrower than the full IR range. Besides, in many experiments, the IR camera must detect the sample's temperature radiating through the atmosphere. Therefore, the detector response curve must coincide with a precise "atmospheric window", in other words, the range of IR wavelengths that propagate undisturbed through the atmosphere without being attenuated. These “atmospheric windows” are basically two (**Figure 3.1**): (i) the short/medium wavelength (SW / MW) IR band (2–5.6μm), and (ii) the long-wavelength (LW) IR band (8–14μm). To meet these criteria, specific materials are used to build sensitive detectors in these wavelength ranges.

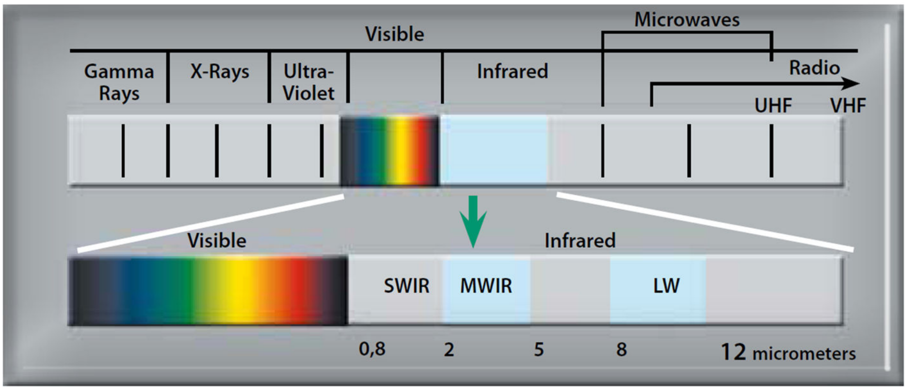

Figure 3.1 – An illustration of the IR portion of the electromagnetic spectrum seen by an IR thermal camera.

Furthermore, the materials of which the lenses of IR cameras are made are transparent to IR (they can transmit almost 100% of the incident radiation) and are opaque to visible light, such as silicon (Si) and germanium (Ge), and have an anti-reflective coating. Si is normally used for medium wavelength IR (MWIR) camera systems, while Ge is used for long wavelength (LW) cameras. [128] Furthermore, Si and Ge have good mechanical properties, are resistant to injuries and impacts, and are not hygroscopic.

The most common detector mounted by IR cameras is the microbolometer type. This means that inside of a thermal camera, there are a bunch of tiny measuring devices that capture IR radiation, the microbolometers, and each pixel has one. Microbolometer FPAs made up of metal or semiconductor materials, work according to non-quantum principles, so they react to radiant energy by inducing a change of state in the bulk material (i.e., the bolometer effect). Generally, microbolometers allow compact camera designs (handheld thermal imaging cameras), as they do not require the additional step of cooling. In practice, the operation at the base of the microbolometers consists of several steps: (i) the thermal radiation impacts on the detector, (ii) the detector sensors increase in temperature, (iii) there is a change in the electrical resistance of the sensor material, (iv) changes in resistance are interpreted by a processor generating an image on a display, finally (v) the detector constructs the thermogram. The whole process happens very quickly, with a rate of about 30 times per second.[151]

For experiments that require greater sensitivity to IR radiation, it is preferable to use quantum detectors, whose operation is based on an intrinsic photoelectric effect. These materials absorb IR photons, which lead electrons to a higher energy state, causing a change in conductivity, voltage, or current. By cooling these detectors to cryogenic temperatures, excellent IR sensitivity is achieved.[128]

In particular, the IR camera used, FLIR A655sc is equipped with an uncooled, Vanadium Oxide (VoX) microbolometer detector that works in the spectral range 7.5-14 µm and produces thermal images with a resolution of 640x480 pixels. A large number of pixels allows generating detailed and highly resolute images, from which it is easy to deduce the desired temperature information. In fact, the FLIR A655sc allows to clearly appreciate temperature differences up to 50 mK (<0.05 ° C), with high accuracy. This value is related to the thermal sensitivity or Noise Equivalent Temperature Difference (NETD) and describes the smallest temperature difference detectable with the IR camera.

When performing temperature measurements using an IR camera, another important camera specification is the smallest area of an object that can be accurately detected and measured at a given distance, i.e. the Field of View (FOV). This parameter, usually expressed in degrees (e.g. 25 ° × 19 °, 31 ° diagonal), is related to the camera lens and focal plane size, and considered a fixed distance, this indicates the dimensions of the total surface area "seen" by the instrument (see **Figure 3.2**). For example, a FLIR A655sc camera with a 24.6mm lens has an FOV of 0.44× 0.33 meters at a distance of one meter, and 4.4 × 3.3 meters at a distance of ten meters. While the Instantaneous Field of View (IFOV) provides information on the spatial resolution of a camera's focal plane array (FPA) detector, and the area covered by an individual pixel in the array. [128] The configuration of the FPA in the FLIR A655sc is 640 × 480 detectors, which makes a total of 307.200 individual picture elements (pixels). To correctly analyze, using a thermal-camera, an object placed at a distance of one meter; it is important to determine the IFOV. If the total FOV is 32 × 24mm at a distance of one meter, dividing these FOV dimensions by the number of pixels in a line and a row, respectively, turns out that the IFOV of a pixel is an area 0.05 × 0.05 mm. Such micro resolution dimensions can be reached due to the IR microscopic capability. A close-up IR lens, 2.9 × (50µm) mounted on the standard 24.6mm lens, lets the camera take images on a micro-scale. The Flir A655sc camera, with IFOV of 0.68 mrad/pixel, (with a 25° lens, f=24.6mm) has the pixel that, at a distance of 0.5m, covers an area of 0.35 × 0.35 mm. So, with the A655sc, at 0.5m distance, one could correctly measure an object's temperature no smaller than 0.35mm on each side.

Conventionally it is assumed that the object must cover at least 9 pixels (3 pixels per side), and must therefore be 3 times larger than the single pixel, in order not to measure the temperature adjacent to the object being measured. The minimum measurable area with FLIR A655sc (at a distance of 0.5m) is 1.05mm x 1.05mm. Therefore, it is important to compare the object of interest's size with the IFOV value before performing any temperature measurements. Furthermore, in the case of dynamic temperature measurements of a phenomenon that occurs over time, the acquisition rate of the thermal images acquired by the sensor must be considered. Also, the following technical specifications are given in the instrument manual: “the FLIR A655sc provides 14-bit data up to 50 frames per second at full frame 640 × 480 resolution; it has a high speed windowing function that increases the output frame rate up to 200 Hz at a 640 x 120 pixel window.” The complete technical specifications are given in **Tab 3.1**.

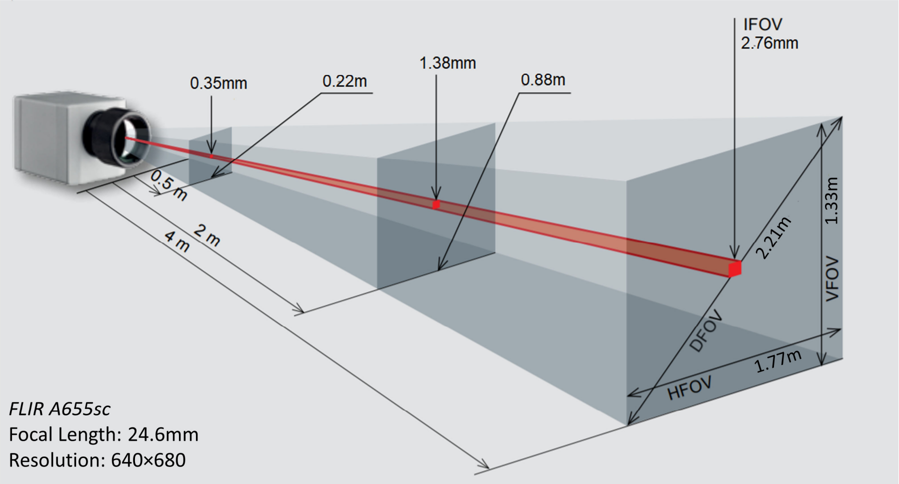

Figure 3.2 – *The thermal camera has a well-defined detection area, known as the field of view (FOV), distinguishable in its horizontal (HFOV), vertical (VFOV), and diagonal components (DFOV), on which the size of the individual pixels (IFOV) depends. The more distant the object is, the greater the observed area and, with it, also the area analyzed by the single pixel.*

Tab 3.1 *– Technical specifications of the infrared camera FLIR A655sc, with a close-up IR lens, 2.9× (50µm) mounted on the 24.6mm lens (FOV 25°× 19°), used in the experiments.*

Detector Type	focal plane array (FPA), uncooled microbolometer
Temperature range	–40°C to +150°C / 100 to +650°C
Thermal sensitivity/NETD	< 0.03°C at +30°C / 30 mK
IR Measurment Accuracy	±2°C or ±2% of reading
IR Spectral Range	LWIR (7.5-14 µm)
IR Resolution	640 × 480 pixels
Detector Pitch	17 µm
Field of view (FOV)	32 × 24 mm (40 mm diagonally)
Magnifying factor	2.9×
Min. Working distance	84 mm
Depth of field	0.65 mm
Focal Length	78 mm
Spatial resolution (IFOV)	50 µm
Frame rate (full window)	50 Hz
Max. Frame rate	200 Hz (640×120)
Dynamic range	14-bit

Experimental temperature measurements

Usually, the photothermal-setup consist of a CW pump laser, that can work in the VIS ($i.e. \lambda = 532nm$, for 20nm spherical AuNPs) or NIR region ($i.e. \lambda = 808\,nm$, for AuNRs), a series of mirror used to excite the AuNPs from the top impinging perpendicularly to the air/solution or air/substrate interface, a series of lens to adjust the beam spot size w and consequently the impinging intensity $I\ (Wcm^{-2})$, and an IR photothermal camera. It is important to point out that IR thermography is a valid method of measuring NIR irradiation as the excitation and emission wavelengths are not overlapped (for example excitation 808 nm, measurement band 7.5-13 μm).[152] This separation in wavelength allows for NIR excitation and mid-IR measurement with no overlap. However, the IR camera is commonly mounted at an angle of approximately 90° to the laser such that the sample was irradiated in an area coinciding with the active area of the camera while not interfering with the imaging. Furthermore, detecting sideways the temperature from the sample tube-like container (i.e. quartz Cuvette, Eppendorf vial, glass tube), with the laser radiation that propagates parallel with the sample container axis, allows obtaining a depth profile of temperature. Once the power laser is fixed, and the recording time is set, the IR camera records several thermographs at a certain imaging rate. During and immediately after the experiment, the first qualitative analysis of raw IR images aims to monitor the surface temperature changes in a continuous way. In this first step, before image processing, it is important to set the most suitable color palettes that can be different for different purpose. For example, in engineering applications, a color palette called ‘iron’ is used where yellow is hotter than red, and white is hotter than yellow, as found when iron is heated in a furnace. In medicine, where the temperature range is different, a ‘rainbow’ palette is preferred, with red as hot and blue/black as cold. In general, throughout this thesis, a slightly modified rainbow palette (called ‘1234’) is used, in which the color gradient starts from yellow, for the hottest point, to dark blue, for the colder one (**Figure 3.3**). These color scales may also be linear or logarithmic in distribution, and in some software packages, the user can generate his own color scale for a specific application if required. In general, the temperature color scale used at the time of image capture should be displayed alongside the final image (see **Figure 3.3**). Without this, the image is poorly defined since the range and level of temperatures are essential to the full information provided in the thermogram.[148]

Subsequently, the IR images are processed employing a custom analysis software, the ResearchIR thermographic data acquisition and analysis software, which can serve a wide variety of functions from real-time image acquisition to post-acquisition processing of thermographs. A Region of Interest ROI can be selected, allowing the analysis of a single points, line profiles, and averages of circle/rectangular areas. Both the sample positions with respect to the camera, and the location and shape of ROI has been shown to have a marked influence on both the accuracy and precision of temperature measurements obtained from thermal images.[148] Processing of IR image sequences aims to evaluate, for example, the temporal behavior and spatial distribution of the mean/max temperature. Furthermore, through the plot tools, it can be selected one of each plot type per Region (ROI). The plots available are: (i) the profile plot, (ii) the temporal plot, (iii) the histogram plot, and (iv) the oscilloscope plot. The profile plot creates a linear graph of the temperature data encompassed in a ROI, the temporal plot represents the temperature of a ROI as a function of time, the histogram plot shows the spatial distribution of temperature values within an ROI, and the oscilloscope plot (O-scope) gives an "edge-on" view of the image.

Figure 3.3 shows some examples of IR images acquired with our IR thermal camera and the plots obtainable of the temperature as a function of time or space.

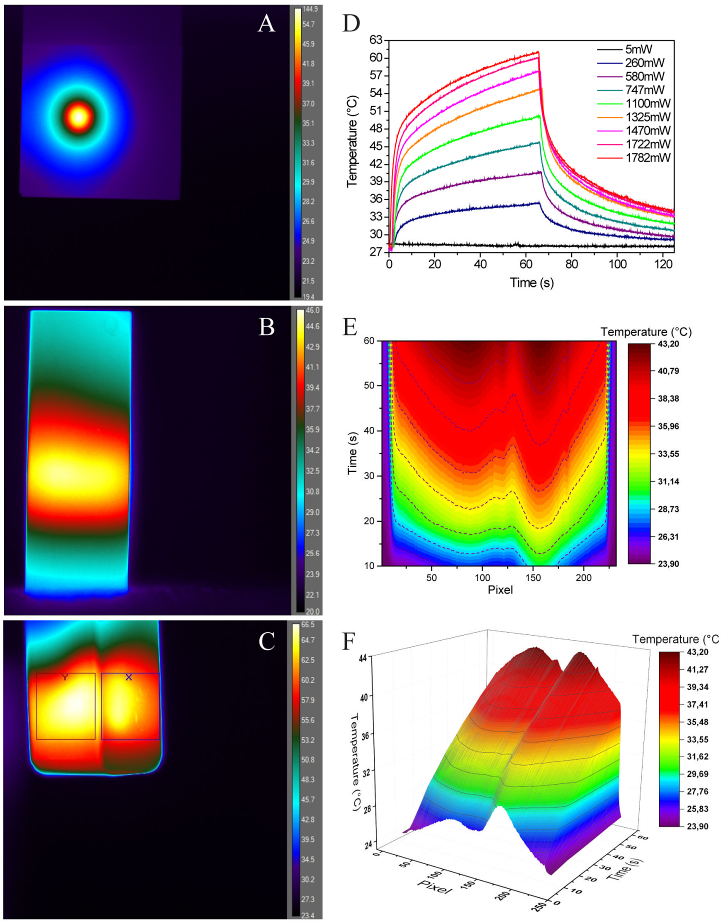

Figure 3.3 *–Representative IR thermographic images (color palette '1234') extracted from experiments conducted with (A) AuNRs deposited on a substrate, and colloidal solutions of AuNPs contained in a quartz cuvette (B, C), along with illustrative graphs of the temporal behavior (D), 2D spatial map (E), and 3D spatial distribution (F) of temperature.*

3.3 Nanoscale thermometers: thermo-responsive smart materials

The combined effects of thermal information at lower length scales and the unprecedented possibilities opened up by nanomaterials and nanotechnologies are paving the way for the development of nano-thermometry with high spatial resolution.[153] This paragraph shows the use of smart materials with thermo-responsive properties, thermotropic LCs, and thermoresponsive poly(N-isopropylacrylamide) (PNIPAm)hydrogels, for monitoring and controlling the heating induced at the nanoscale by AuNPs.

3.3.1 Thermotropic Liquid Crystals

LCs are a phase of the matter beneficial in several research fields such as biology, chemistry, physics, electronics, optics, and biomedicine.[154] The term “Liquid Crystal”, first used by O. Lehmann in 1890, designates a state of matter intermediate between the solid crystalline and the ordinary (isotropic) liquid phases.[155] LCs flow like ordinary liquids (e.g., they adopt the shape of their container). On the other hand, they exhibit anisotropic properties as do solid crystal. Their physical properties (optical, electrical, and magnetic) are dependent on the direction in which they are measured. LCs are also defined mesophases or mesomorphic phases, derived from the Ancient Greek word *mésos*, meaning ‘in-between’ or ‘intermediate’, because of their intermediate nature. Liquid crystallinity is exhibited by several naturally occurring materials, including DNA, proteins, cell membranes, and insects’ shell.[156]

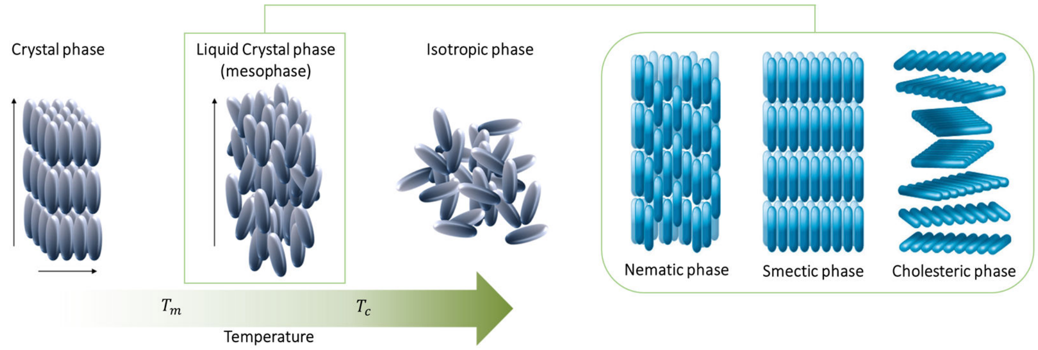

Figure 3.4 *– On the left, temperature-dependent transitions from the crystalline state through to the isotropic liquid state passing from the melting point (Tm) and clearing point (Tc). On the right, arrangement of molecules in the nematic, smectic, and cholesteric LC phase.*

Depending on the nature of the phases they form, LCs can be divided into two general classes: thermotropic and lyotropic LCs. The behavior of thermotropic LCs is dependent on temperature: they usually exhibit mesophases either on heating material from the crystalline solid state or on cooling from the isotropic liquid state (**Figure 3.4**). Lyotropic LCs, on the other hand, are formed on the change of concentration of amphiphilic molecules dispersed in an isotropic medium – for example, surfactant molecules dispersed in water.

There are three basic types of LCs phases exhibited by thermotropic mesogens, denominated as smectic, nematic, and cholesteric (**Figure 3.4**), following the classification proposed by Friedel[157]. In all three types of phases, the LC molecules are aligned along a preferential direction, known as the director **n**, which is the average orientation of the molecules within the phase. It is essential to quantify how much the molecules are ordered within a phase, and this is possible through the order parameter, S[154]:

$$S = \frac{1}{2}\langle 3cos^2\theta - 1\rangle \tag{3.7}$$

where θ represents the angle between the director and the long axis of an individual molecule. The order parameter is temperature dependent and is in the range $-\frac{1}{2} < S < 1$. Since the cosine of 0° is 1, perfect orientational order (all angle equal to 0°) results in S=1. In addition, in a liquid with no orientational order, S = 0.[158]

In the nematic phase, molecules possess long-range orientational order, but there is no positional order. Typically for a nematic phase, the order parameter *S* is between 0.4 and 0.7.[159] Smectic phases, like nematic phases, possess orientational ordering along the director. Compared to nematic phases, however, they have a higher degree of order. Molecules in the smectic phase are arranged in a layered structure with a well-defined interlayer spacing. The cholesteric, or chiral nematic phase, exhibits long-range orientational order, like the nematic phase, and a twisted structure, whereby the director rotates at an angle perpendicular to the director, to form a helical structure of a certain pitch length. The distance at which the director rotates a full 360° around the helical axis is called the pitch, p.

In a LC device, also known as a 'cell', it is possible to achieve a preferred orientation of the LC director by surface treatment of the glass substrates and this consequently determines the optical properties of the device. Two types of alignment are typically used when characterizing LC devices: planar alignment (sometimes referred to as 'homogeneous') and homeotropic alignment, both reported in **Figure 3.5**.

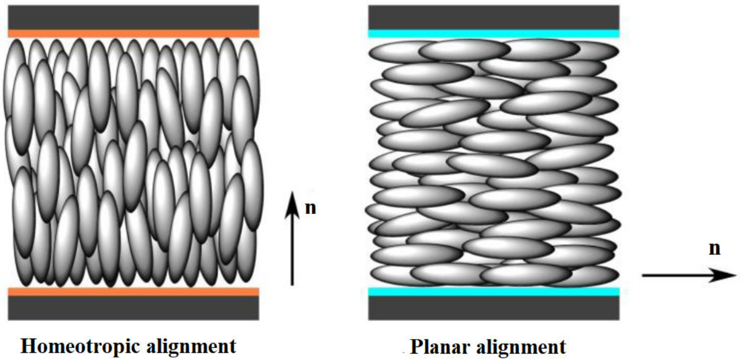

Figure 3.5 *– A diagram representing the orientation of the NLC director n in a homeotropic and planar cell.*

For a uniaxial NLC in a planar device, the LC director's orientation is parallel to the glass substrates. In a homeotropic device, the LC director is perpendicular to the glass substrates.

These alignments are generally achieved by depositing a thin polyimide layer onto the glass substrates' surface, which anchors the LC to the preferred alignment. To achieve a uniform preferred direction of the director, the polyimide layer can be rubbed with a velvet cloth, which creates grooves on the surface of the planar substrate and the director will lie along the direction of these grooves, i.e. along the 'rubbing direction'.[160]

Another important, non-contact, all-optical method used to align LCs is photoalignment.[161] A photosensitive film of polymer (Photo-Alignment Layer, PAL) is deposited on the surface of the glass substrate by means of a spin coating or spray coating. Then the substrate is exposed to linearly polarized UV light. Due to the dependence of the absorption of light by the molecules of the photosensitive film on the polarization direction, an anisotropic distribution of the orientation of the molecules of the alignment materials occurs; in this way, the induced degree of surface ordering on the layer is further transferred to the LC molecules, that become oriented. The few nanometers thick film act as a command layer for controlling the LCs order. As a matter of fact, PALs have generated interest as they possess significant advantages in comparison with standard rubbing treatments of LCs cell substrates, providing a: (i) non-contact method controllable by a suitable external light, (ii) reversible and reproducible aligning mechanism, (ii) simple processing by spin-coating.[62] A particular class of PAL materials is illustrated in the following paragraphs, the azobenzene-based photo-anisotropic materials as Photo-Alignment or command Layers (PALs) for LCs going into the details of its anisotropic thermal behavior.

NLCs and CLCs, have attracted much attention in both scientific studies and application among all the soft and smart materials thanks to distinctive features: the possibility of modifying their physical and optical properties using external stimuli,[162] and here we will focus on the effect of photothermal heating from AuNPs. This mutual effect between LCs and AuNPs turns out to be a new and interesting way to probe and control the nanoscale temperature. Indeed LCs have been exploited as active media for controlling the LSPR frequency of AuNPs and for detecting photo-induced temperature variation at the nanoscale.

The main characteristic of LCs to be considered is their optical anisotropy. The director's uniaxial symmetry in the NLC phase leads to an anisotropy in the refractive index, the dielectric permittivity, magnetic susceptibility, viscosity, and conductivity. All these physical quantities have different values, depending on the mutual correspondence between the external field polarization and the LC director. The anisotropy of NLCs causes light polarized along the director n to propagate at a different velocity than light polarized perpendicular to it; therefore, LCs are birefringent.[154]A uniaxial NLC has two principal refractive indices: the ordinary refractive index n_o and the extraordinary refractive index n_e (**Figure 3.6**).

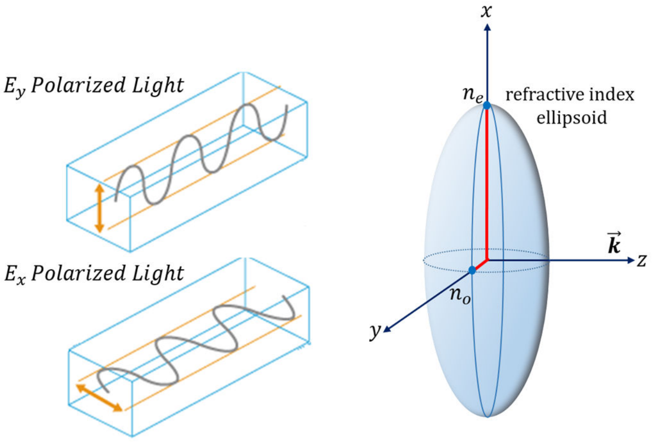

Figure 3.6 – Light propagation in NLCs parallel and perpendicular to the optical axis: n_e - extraordinary refractive index; n_o - ordinary refractive index.

The first one, n_o, is seen by the light wave whose electric vector is perpendicular to the optical axis (ordinary wave). The index n_e is seen by the light wave whose electric vector is along the optical axis (extraordinary wave). The birefringence is given by[163]:

$$\Delta n = n_e - n_o = n_\parallel - n_\perp \tag{3.8}$$

Where $n_\parallel$ and $n_\perp$ are the components parallel and perpendicular to the director, respectively. In the case of uniaxial NLCs the optical axis coincides with the direction of n and the indices n_o and n_e are measured for light propagating along or normal to the optical axis. In general, birefringence Δn of LCs decreases as the wavelength of the incident light or the temperature increases.

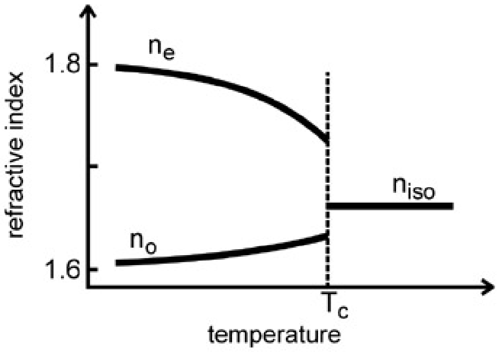

Figure 3.7 – Temperature dependence of the refractive index. T_c is the clearing temperature; n_{iso} is the isotropic LC refractive index.

Unpolarized light incident upon a NLC is split into an ordinary and an extraordinary wave, which travels with different velocities through the material.[164] The two waves, after having crossed the thickness d of LC, are out of phase by an amount equal to:

$$\Delta\varphi = 2\pi\Delta n d/\lambda \tag{3.9}$$

The birefringent nature of LCs is clearly evident when a LC cell is placed between crossed polarizers. Normally no light emerge, because the light emerging from the first polarizer is completely absorbed by the second polarizer. Insertion of an isotropic material does not change this because the polarization of light is unchanged as it travels through an isotropic material.

When the plane of polarized light from the first polarizer passes through the LC layer, it becomes elliptically polarized (diffracted) due to birefringence and, therefore, it can pass through the second polarizer (called the ‘analyzer’), which is aligned at a 90° angle to the first polarizer. As a result, colored textures that are characteristic of specific LC phases can be observed. These are best obtained when the LC material is cooled from its isotropic state. On the other hand, an isotropic liquid would appear black between crossed polarizers because the plane of polarized light from the polarizer would not get diffracted when passing through the liquid and, as a result, would get blocked by the analyzer.

LCs can align themselves homeotropically between two untreated glass substrates. In this case, the light passing through the polarizer experiences only one of the material’s refractive indices and does not get diffracted, as is the case for isotropic liquids. Therefore, the homeotropically aligned sample appears black. When the alignment direction of the planar cells is (i) parallel (0°, 90°) to either the polarizer or analyzer, the sample will appear dark for a nematic sample because the director lies along the alignment direction; (ii) tilted with angles different of 0° or 90°, the light is transmitted, with maximum transmission at 45°.

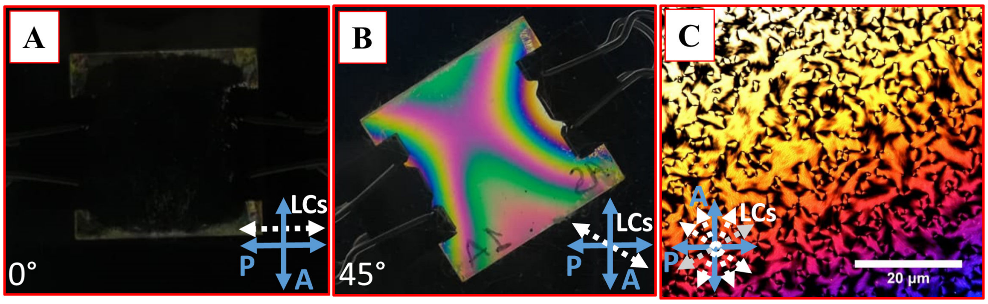

Figure 3.8 *– Two identical NLCs cells viewed between crossed polarizer, when the director is aligned parallel to P or A (A) and at alignment of 45° (B). Colored texture of the nematic phase when the LC is viewed between two untreated glass substrates (C).*

Figure 3.8 C shows the typical textures observed for a NLC between untreated glass substrates. The black lines represent schlieren textures and are observed when the LC director lies parallel to the crossed polarizers.

In the case of CLCs the optic axis coincides with the helix axis which is perpendicular to the local director; $n_e = n_\perp$, and n_o is a function of both $n_\parallel$ and $n_\perp$ and depends on the relative magnitude of the wavelength with respect to the pitch.

$$n_o = \left[\frac{1}{2}\left(n_\parallel^2 + n_\perp^2\right)\right]^{1/2} \qquad n_e = n_\perp \tag{3.10}$$

CLCs, due to their high birefringence and their helical configuration, exhibit two other fundamental characteristics: (i) selective reflection band; (ii) tunability of the helix pitch.

For light propagating along the helix axis, CLCs exhibit a Bragg reflection ($\boldsymbol{\lambda_B}$) band for circularly polarized light with the same handedness as the helix over the wavelength range $n_oP<\lambda<n_eP$. Light of opposite handedness propagates through the CLC film without being affected.

$$\lambda_B = p\bar{n} \tag{3.11}$$

Where $\bar{n}$ is the average refractive index of CLC, defined as $\bar{n} = (n_e + n_o)/2$.

The pitch p of a CLC film is sensitive to temperature variations allowing a simple probe of average temperature caused by LSPR induced heating. The experimental applications resulting from these characteristics will be illustrated in detail in the following paragraphs.

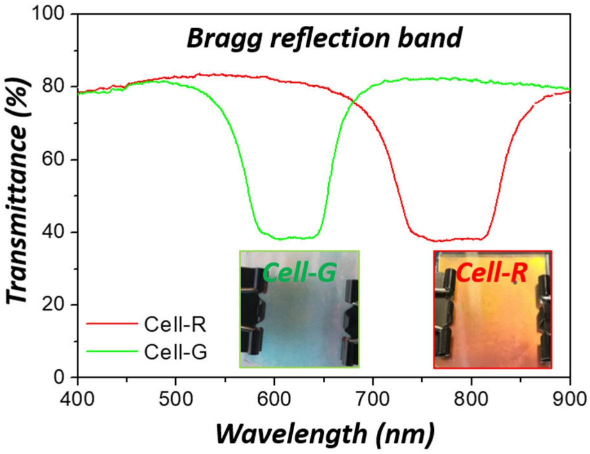

Figure 3.9 *– Bragg reflection band shift, due to the CLC pitch stretching as the temperature increases, which results in a color change of the CLCs cells.*

3.3.1.1 Application 1: A command layer for anisotropic plasmonic photo-thermal effects in liquid crystal

In this section, the photo-anisotropic properties of a particular LCs command layer, based on azobenzene material, are exploited to control the photo-thermal response of a single layer of homogeneously and uniformly distributed AuNPs, immobilized on a glass substrate. The intrinsic anisotropy of the azobenzene-based photo-alignment layer (PAL) can influence the photo-thermal response of plasmonic systems. As already discussed in the previous chapter, the resonant absorption of radiation by plasmonic subunits, the AuNPs, is followed by a noticeable increase in their temperature. Although, the thermal response observed in presence of a homogeneous and random array of AuNPs directly exposed to air or embedded in ice is typically isotropic; depositing a homogenous, yet thin, coating of a PAL on a large-area carpet of AuNPs, influences their thermal response in an anisotropic way related on the alignment direction of the command layer molecules. This effect makes the command layer of particular interest for its capability to drive intriguing optically induced 'thermal-reorientation' effects in a LC film.

Realization of the hybrid device

The fabrication of this device was conceived in a layer-by-layer way. The first step is the synthesis (exploiting a slightly modified Turkevich method [165]) and deposition of a colloidal solution of AuNPs on a glass substrate. The glass substrate surface has been properly functionalized in order to obtain positively charged surfaces; then, the process of NPs deposition has been realized by dipping the substrates in a solution of colloidal AuNPs for 50 min. In order to evaluate the active role of a single NPs layer a peel off of the NPs from one side is performed.

The second step is the deposition of the azobenzene-based PAL by means of a spin coater (2000 rpm @ 30 s). The AuNPs layer has been covered with a thin film of PAL, made of randomly aligned molecules of azo-dye (PAAD-27 by BeamCo), dissolved in dimethylformamide, which possesses a broad absorption band centered at 415 nm.

The elongated molecules of PAAD-27 exhibit the feature that, when acted on by a polarized UV light for a suitable time interval (typically 10 min), they reorient perpendicularly to the light polarization direction in order to minimize the absorption cross section. By simply varying the polarization direction of the impinging UV light, it is, therefore, possible to reorient the PAL molecules, along with the molecular director of a NLC that the PAL is, possibly, put in contact with.[62]

Morphological and spectral analysis

Once the device is assembled, the morphological and spectral analysis of the AuNPs sample before (sample A) and after (sample B) the PAL deposition was carried out. The atomic force microscopy (AFM) analysis (**Figure 3.10**) reveals: (i) in sample A, a uniform distribution of well-dispersed AuNPs with a surface density of $355 NPs/\mu m^2$ and an average height of $(30 \pm 6) nm$ (ii) in sample B, a planarization of the surface due to the presence of the PAL that is interposed between the NPS, average height of $(10 \pm 6) nm$.

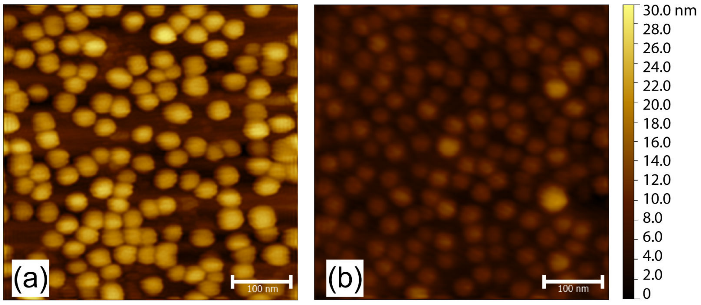

Figure 3.10 *– AFM topography of the AuNPs sample (a) before (sample A) and (b) after (sample B) the PAL deposition.*

The spectral analysis of sample A shows the typical LSPR band of spherical AuNPs in the green region of the spectrum, centered a λ_{LSPR} =533nm (**Figure 3.11 a,** black curve), while sample B (AuNPs+PAL, **Figure 3.11 a**, red curve) shows an absorption increase of about 11% and a red shift of the LSPR of about 13 nm (λ_{LSPR} =546nm). The modification of the spectral response is due to the change in the refractive index of the surrounding medium, from the air value ($n_a = 1$) to the PAAD-27 value ($n_{PAL} = 1.73$), as extensively explained in the theoretical Chapter 1 (paragraph 1.5.3). This experimentally observed result is confirmed by a theoretical prediction (**Figure 3.11 b**), based on the Mie Theory which provides an analytical solution of Maxwell's equations for the scattering/absorption of an electro-magnetic radiation induced by small and isolated AuNPs.

Furthermore, similar behaviors, due to the presence of the PAL layer, have also been observed in other previous works[162], which confirm the occurrence of a red shift ($\cong 12nm$) in the λ_{LSPR} and the planarization effect observed in **Figure 3.10 b**, induced by the PAL that is distributed among the AuNPs, making the surface uniform.

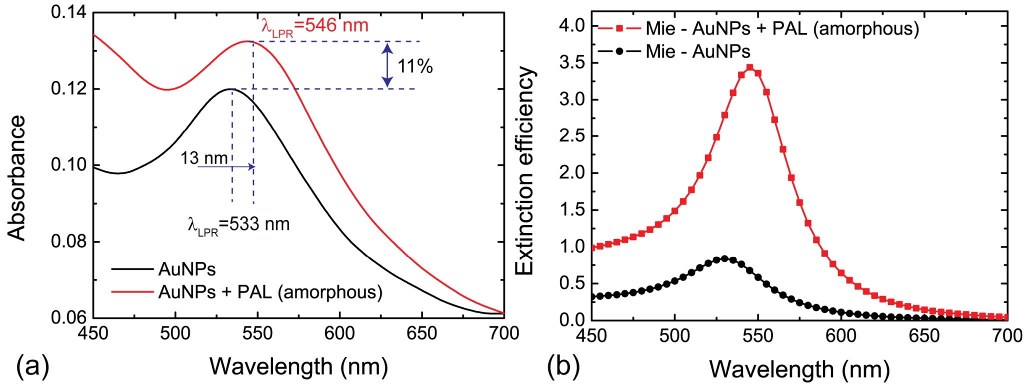

Figure 3.11 *– Spectral response (a) and theoretical prediction (Mie theory) (b) of the extinction efficiency of the AuNPs sample surrounded by air (black curve), and PAL (red curve).*

Photo-thermal analysis

To evaluate the photo-thermal efficiency of the sample, a CW green laser emitting at λ = 532 nm, with a spot size of 0.21 cm^2, is used as pump; measurements are performed at power intervals of 200 mW in the range 0.2–1.2 W, corresponding to intensity variations from 1.0 W cm^{-2} to 6.0 W cm^{-2}. Thermographic analysis is performed at a small angle with respect to the pump beam (that impinges perpendicularly to the sample) by means of a thermocamera (E40 by FLIR) characterized by an accuracy of ± 1.0°C and a spatial resolution of 2.72 mrad. Control parameters are appropriately set to take into account both environmental and material properties; reflected temperature was set to T_0 = 20°C, emissivity of glass to ε = 0.83, and the working distance between camera and object was adjusted to the allowed minimum value, that is, less than 10 cm.

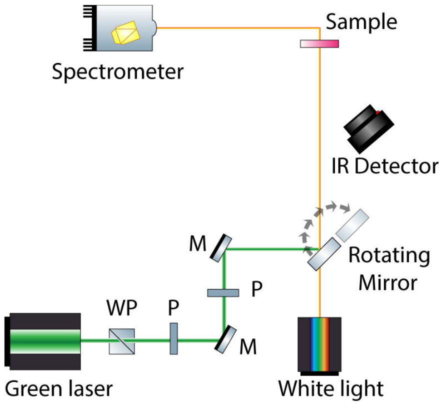

Figure 3.12 *– Sketch of the thermo-optical setup. WP: waveplate, P: polarizer, M: mirror.*

By monitoring temperature values of the central pixel of each hot-spot of the thermographic images (**Figure 3.13**), which corresponds to the warmest point, we plot the temperature variation ΔT = T − T_0 versus the impinging power (T_0 is the sample temperature when the pump beam is off, see **Figure 3.13 e, f**). Measured ΔT values show a linear increase as a function of the pump power; in particular, the ΔT corresponding to the maximum power (1.2 W) for the sample A is ΔT = (15.1 ± 1.0) °C, while the ΔT is equal to (27.3 ± 1) °C in the case of sample B.

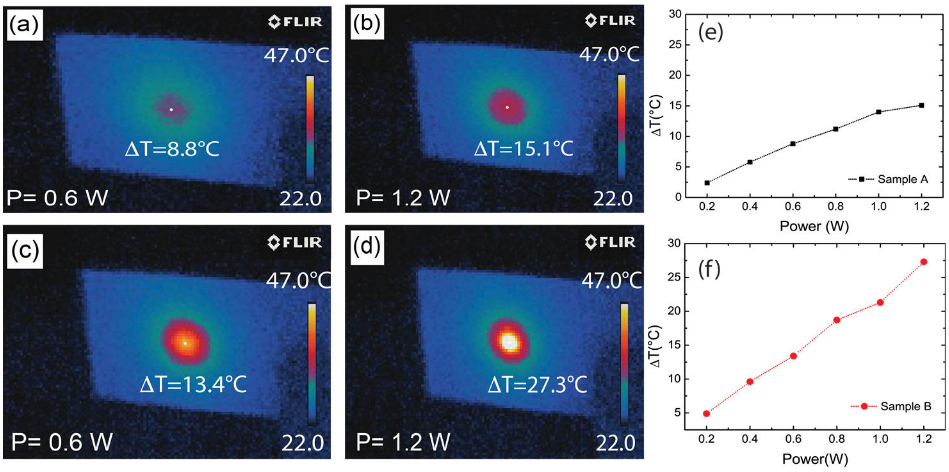

Figure 3.13 – *Thermographic images of sample A (a, b) and sample B (c, d), for different power values of the pump beam. Temperature variation versus pump beam power for (e) sample A (black curve) and (f) sample B (red curve).*

Once the photo-thermal response of samples has been estimated, the impact of the different alignment of the PAL is investigated. After exposing sample B to the UV-polarized light, indicated by 'Ex aligned' we repeated the spectral analysis on sample B, observing an increase of the plasmonic band intensity of about 10% and no shift of the position of the LSPR peak. By exposing again sample B to the polarized light after rotating of 90° the polarizer with respect to the previous one (we indicate by 'Ey aligned' the new polarization direction), we obtain the same spectral response in the whole area of the plasmonic band (**Figure 3.14**).

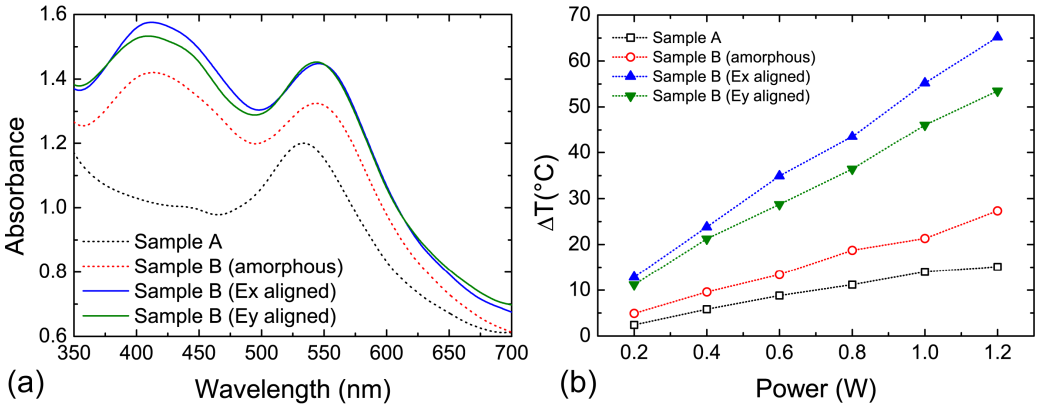

Figure 3.14 – *Spectral response of the samples A and B in the case of Ex-polarized aligning blue light (blue curve) and Ey polarized blue light (green curve) (b). Temperature variations of the samples B for the two different orientation alignments.*

The observation that the LSPR band does not change for the two different alignments indicates that there are no variations in the refractive index of the PAL. Indeed, same λ_{LSPR} means same Fröhlich condition (equation (1.12)), which implies the absence of changes in the host medium dielectric permittivity. Furthermore, for the two different Ex and Ey alignments, we observe not only the same resonance wavelength but also the same absorbance value; however, this overlap of the absorption spectrum does not correspond to an overlap of the detected temperature variations. Although the optical response of sample B does not change, its thermal response (**Figure 3.14 b**) turns out to be very different for the two different PAL alignments.

This can be explained by observing that the system absorbance depends on the polarizability α (1.11) whose denominator determines the Fröhlich condition $Re[\varepsilon(\omega)] = -2\varepsilon_m$, while temperature variations depend also on the thermal conductivity. Thus, we can argue that the three different PAL alignment conditions (amorphous, Ex aligned and Ey aligned) induce different thermal conductivities, though they induce the same optical response of the sample. Furthermore, we can say that the 'Ex aligned' and 'Ey aligned' conditions induce a reversible and repeatable thermal anisotropy due to an induced change of the thermal conductivity of the PAL, which depends on the polarization direction of the resonant impinging light.

As previously specified, from equation (2.25) it is possible to calculate the thermal conductivity k_H from a simple inverse relation in which the angular coefficient of ΔT versus intensity I_0 is calculated. The thermal conductivities K_H of the PAL in the three cases are measured as: 0.77 W(°K m)$^{-1}$ for the amorphous PAL, 0.32 W(°K m)$^{-1}$ for the Ex aligned PAL, and 0.40 W(°K m)$^{-1}$ for the Ey aligned PAL.

These results demonstrate that: (i) thermal conductivity is strongly dependent on the PAL orientation confirming the anisotropy of the material; (ii) the temperature increase can be controlled by varying the orientation of the PAL molecules; (iii) is possible to drive the thermal behavior of PAL materials through polarized light to obtain different thermal responses of a new smart LC device.

3.3.1.2 Application 2: Dynamic optical properties of gold nanoparticles/cholesteric liquid crystal arrays

In this section, it is shown the possibility of fabricating a thermoresponsive large-area plasmonic architecture (1 inch^2) of randomly distributed gold NPs (GNPs) immobilized on a glass substrate and covered with a CLC as an active over layer for controlling simultaneously both the photonic and plasmonic properties of the hybrid system. A photo-thermal heating effect due to the localized surface plasmonic resonance (LSPR) mechanism is generated by pumping the GNP array with a resonant light beam. The photo-induced heat, propagating through the CLC layer, induces a gradual phase transition from the cholesteric to isotropic phase. Both the plasmonic and photonic properties of the system as both the selective reflection properties and frequency of the LSPR are modulated. The interplay between photonics and plasmonics allows detecting plasmonic heating via LCs thermometry.

Realization of the hybrid device

As in the previous case, the device is realized in a layer-by-layer methodology, starting from the synthesis with a slightly modified Turkevich method[165], then a monolayer of GNPs is electrostatically immobilized on a BK7 glass substrate.

It is important to remark that we have chosen spherical GNPs because they are more stable than other shapes (e.g., nanorods) and easier to prepare. Moreover, we remind that the photo-thermal efficiency (μ) of GNPs can be expressed through the following equation $\mu = \sigma_{abs}/(\sigma_{abs} + \sigma_{sca})$. It has been shown[36] that if the NP size is about 10–20 nm, σ_{sca} is negligible, thus $\mu \approx 1$. On the other hand, the synthetic path for realizing very small GNPs (e.g., <10 nm) is experimentally challenging and time consuming. For this reason, we chose a NP size (20 nm) to maximize the photo-thermal efficiency while ensuring a simple and reliable synthetic protocol.

At the same time, a CLCs phase is obtained by adding to a NLC (5CB, 4-cyano-4'-pentylbiphenyl, by Merck) a small amount of chiral dopant (20% of left-handed chiral dopant), giving chiral properties to the NLC with a helix pitch length of about 440nm (more chiral dopant results in reduced CLC length pitch). The 20wt.% of chiral dopant is necessary to finely tune (red shift) the CLC reflection band, thus minimizing the overlap between the CLC reflection band and the GNPs plasmonic peak, centered at 600nm and 515nm, respectively. The 5CB NLC is accurately selected for its low transition temperature ($T_{nematic-iso} \approx 38°C$), that is equal to the one obtained for the CLC. The PAL, as in the previous showed work, is a commercially available azo dye (PAAD72 by BEAMCo) with a $\lambda_{max} = 430nm$.

Morphological and spectral analysis

Again, a morphological and spectral analysis was performed.

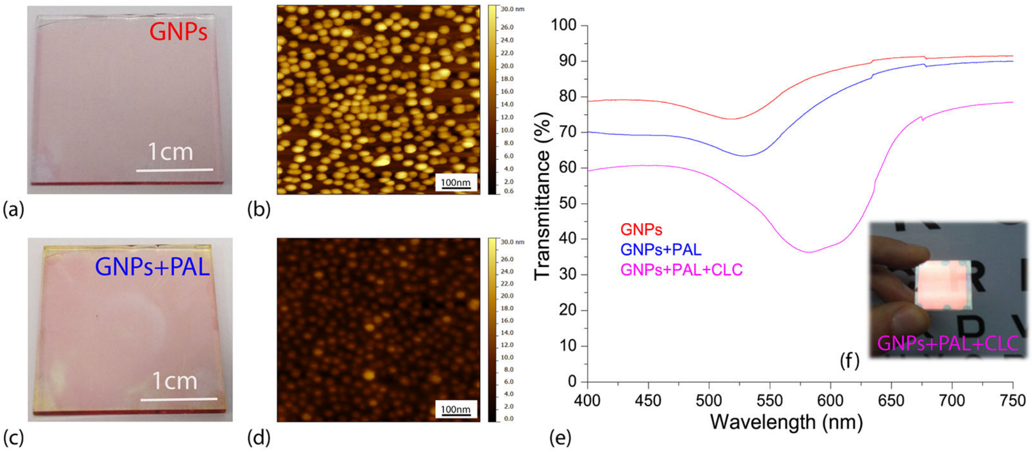

Figure 3.15 *– Photo of the GNP array immobilized on a glass substrate surrounded by air (a) and PAL (c) along with the corresponding AFM topography (b, d). Spectral response of the sample (e) for unpolarized visible light surrounded by air (red curve), PAL (blue curve), and PAL + CLC (magenta curve) along with a photo of the fabricated sample (f).*

As is possible to see in **Figure 3.15 b**, the GNPs substrate exhibits a pinkish tint with an absorption peak at λ_{LSPR} =515nm. After the PAL deposition (spin-coating at 3000rpm for 30s) the substrate undergoes a slight color change **Figure 3.15 c** and the absorption peak experienced a red shift from 515nm (red curve) to 533nm (blue curve) induced by the variation of the refractive index, as shown before.

In order to confirm that the approximation of small and isolated GNPs is valid, the GNPs monolayer was examined by means of an AFM, showing also for this sample a monodisperse status for GNPs with an average diameter of about 20nm and a layer thickness of about 30nm. The PAL, once again, induces a planarization effect (the PAL thickness is about 27nm).

Then, the CLC is "sandwiched" between one substrate possessing the treated GNPs/PAL and a second substrate treated with rubbing to induce the planar alignment of the CLC molecules (CLC helix axis oriented perpendicular to the glass surface). The two substrates are spaced by a 10µm glass microspheres and the CLC is introduced by capillary flow at room temperature. **Figure 3.15 f**, shows the CLC cell highlighting a reddish color due to its selective reflection. For unpolarized light, the spectral response of the sample (**Figure 3.15 e**, magenta curve) shows a broad dip in the transmission curve due to the overlap of the LSPR absorption and the CLC reflection centered at 600nm.

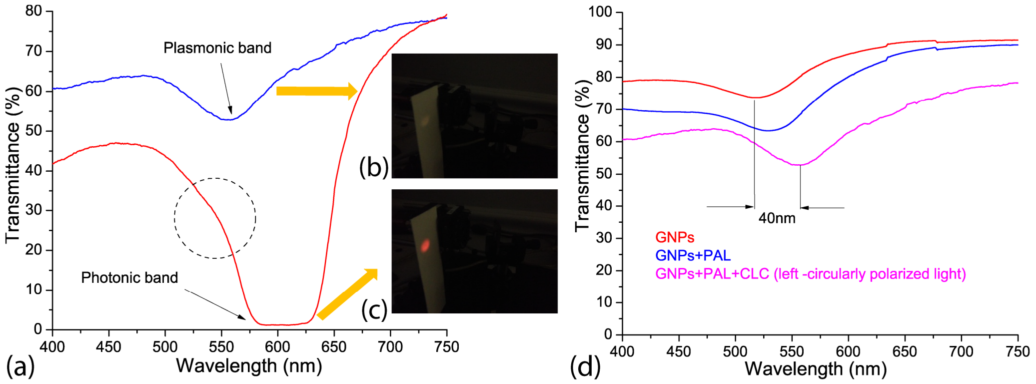

Figure 3.16 *– Spectral response of the sample (a) for left (blue curve) and right (red curve) circularly polarized light along with corresponding photos (b, c) of the back-reflected component. Spectral response of the NPs arrays (d) surrounded by different media, air (red curve), PAL (blue curve), PAL +CLC (magenta curve). The magenta curve in d has been acquired for light left circularly polarized.*

In order to study independently the photonic and plasmonic properties of our hybrid system (to overcome the partial overlap between the LSPR absorption and CLC reflection band), polarized spectral characterization of the samples was done.

As already anticipated before, in the LCs section, for a CLC layer in a planar configuration, circularly polarized light of the same handedness (right circularly polarized, in the actual case) as the helix and having wavelengths between n_oP and n_eP is reflected by the CLC layer (**Figure 3.16 a**, red curve). This is confirmed by visualizing the far field back-reflected component (see reddish spot in **Figure 3.16 c**). Light of the opposite handedness (**Figure 3.16 a**, blue curve) propagates through the CLC film without being affected (the whitish back-reflected spot shown in **Figure 3.16 b** is due to the Fresnel reflection of the glass substrates). Both spectra reported in **Figure 3.16 a** (red and blue curves) have been acquired at normal incidence while the two far field back-reflected spots (**Figure 3.16 b**, **c**) have been acquired by slightly tilting the CLC sample.

It is worth noting that in the blue curve (**Figure 3.16 a**) the LSPR absorption is visible with a remarkable red shift compared to PAL (**Figure 3.15 e**, blue curve). On the other hand, the LSPR absorption is slightly visible in **Figure 3.16 a**, red curve (see dashed circle) due to the overlap between the LSPR absorption and CLC reflection band. Indeed, due to the increasing value of the refractive index surrounding the GNPs [from the PAL layer to the CLC film ($n_{average}$~1.61)], the LSPR frequency is further red-shifted by approximately 28 nm (**Figure 3.16 a**, blue curve). Note: the refractive index of the CLC in cholesteric phase has been calculated as follows: $n_{average}$ (cholesteric)=(n_e+ n_o)/2, where $n_e \approx 1.68$, $n_o \approx 1.52$ are the extraordinary and ordinary refractive indices of the LC, respectively.

To visualize the overall red shift of the sample, the spectral response of the GNP array (**Figure 3.16 d**, red curve), GNP array covered with PAL (**Figure 3.16 d**, blue curve), and GNP array coated with PAL and CLC (**Figure 3.16 d**, magenta curve) is shown. The last one has been acquired for left circularly polarized light to remove the presence of the CLC reflection band. There is a total red shift of the LSPR frequency of about 40nm.

Basically acting on the polarization it is possible to switch from plasmonic to photonics.

Photo-thermal analysis

The key point of this experimental study is to exploit the thermosensitive behavior of the thermotropic CLC. The CLC pitch is sensitive to temperature variations allowing a simple probe of average temperature variations induced by LSPR-induced heating.

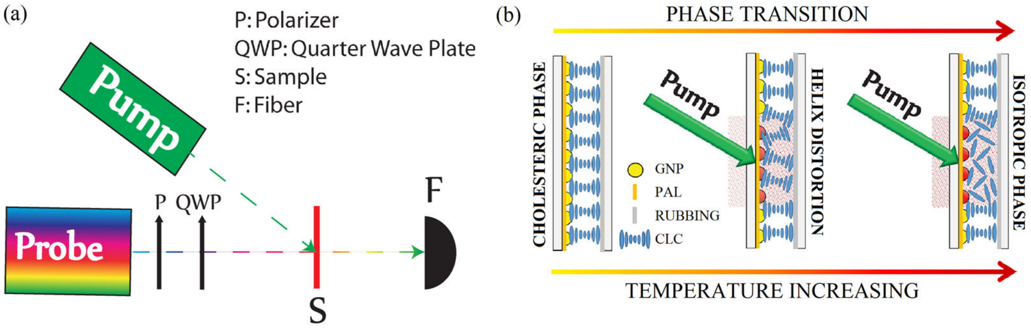

Figure 3.17 *–All-optical setup (a) for sample characterization. Schematic of the sample (b) with the pump beam turned OFF (left) and ON (middle and right) at different power levels.*

So the all-optical setup schematized in **Figure 3.17 a** was used to probe time/temperature/exposure relationships. This setup utilizes a collimated white source (400nm< λ<750 nm) for monitoring the spectral transmission properties of the CLC configuration, and a CW pump laser emitting at λ=532 nm (P_{pump}= 60 mW/cm^2) in the high absorption range of the GNPs surrounded with PAL and CLC. When the pump beam is off, the CLC is planar aligned as sketched in **Figure 3.17 b**, left image.

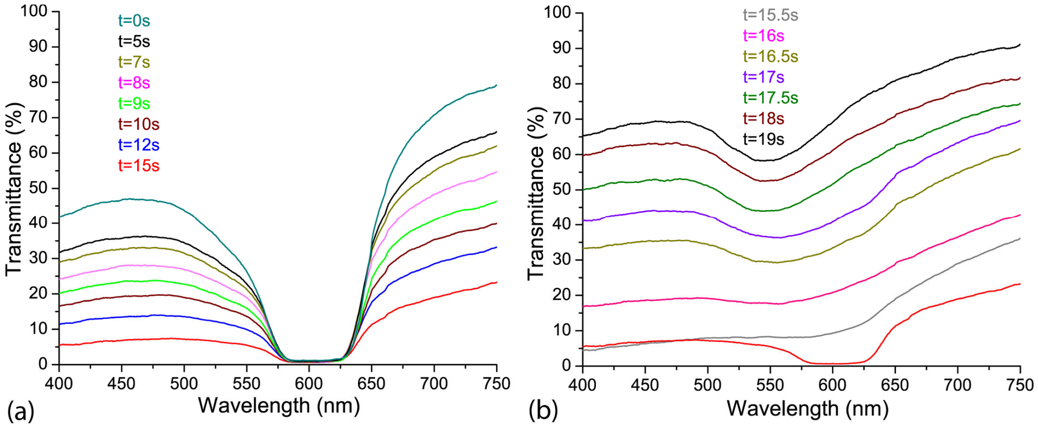

***Figure 3.18** – Spectral response of the sample (probe light right circularly polarized) for different values of the illumination time. For sake of clarity the spectrum is divided in two different spectra having fast (a) and slow (b) back relaxation.*

By gradually photo-exciting the sample (from 0s to 15s) from the GNPs substrate side, there is an electric-driven Joule heating of the GNPs and dissipation of that heat into the surrounding CLC medium (the PAL layer does not change its optical properties with temperature). The local heating induces a deformation/distortion of the CLC alignment (**Figure 3.17 b**, middle image) resulting in attenuation (≈80%) and broadening (≈5nm) of the reflection band (**Figure 3.18 a**). The attenuation is due to a large increase in scattered transmitted light while the broadening is due to a slight chirping of the CLC pitch profile through the thickness of the cell (hot to cold). Continued illumination from 15s to 19s results in the CLC undergoing a phase transition (**Figure 3.17 b**, right image) restoring (**Figure 3.18 b**) the broadband transmitted light intensity (the isotropic CLC does not scatter the impinging radiation). Noteworthy, when the CLC is in isotropic phase the reflection band is completely erased, while the LSPR absorption is clearly visible (**Figure 3.18**, black curve).

In order to check the reversibility and the repeatability of the reported effect, we have performed reflection dynamic experiments by using a low power red probe light (λ=633nm, in the middle of the reflection band). By utilizing a photo-detector, we have monitored the reflection component while turning on and off the pump laser beam (λ=532nm, P_{pump}=60mW/cm^2). In the time interval 0-15s, the CLC configuration is partially deformed (see configuration reported in **Figure 3.17**, middle image) due to induced photo-thermal heating (pump beam on). When the pump beam is turned off, the CLC restores to its initial geometry (**Figure 3.17**, left image) in less than 1s. Conversely, in the time interval 15-19s, since the CLC undergoes a phase transition (and is eliminated) (**Figure 3.17**, right image), when the pump beam is turned off, the CLC takes several minutes to relax back to its initial configuration (**Figure 3.17**, left image). We have repeated the same experiments by photo-heating the samples from the glass side observing the same behavior with a longer time interval (the CLC went to the isotropic phase after 26s).

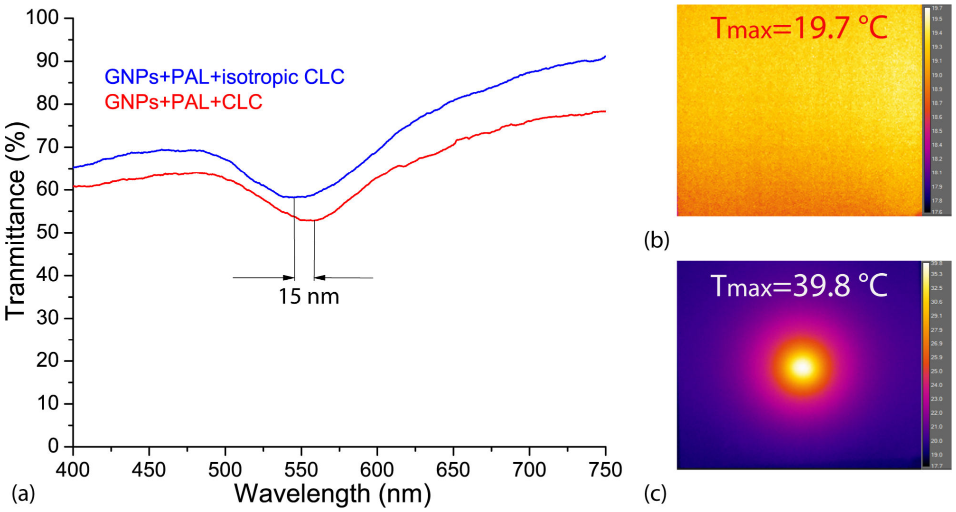

Figure 3.19 *– Spectral response (a) of the sample for left (red curve) and right (blue curve) circularly polarized light having the CLC is the cholesteric and isotropic phases, respectively. Thermographic images of the sample (pump laser beam on) acquired at t =0s (b) and t =20s (c).*

In order to quantify the influence of the CLC refractive index variation on the spectral position of the LSPR peak, the transmission curves of the sample when the CLC is in the cholesteric (**Figure 3.16 d**, magenta curve) and isotropic (**Figure 3.18 b**, black curve) phases can be compared. **Figure 3.19 a** shows a blue-shifted (≈15 nm) LSPR peak due to the decreasing of the refractive index surrounding the GNPs [from cholesteric ($n_{average}$~1.61) to isotropic ($n_{average}$~1.57)], again in agreement with theory. *Note: the refractive index of the CLC in the isotropic phase has been calculated as follows:* $n_{average}$ *(isotropic)* = $(2n_o + n_e)/3$. The photo-induced temperature variations between the two CLC configurations (cholesteric and isotropic phases) were monitored with a high-resolution thermographic camera (FLIR A655sc, resolution 640 × 480 pixels). **Figure 3.19 b** shows a uniform temperature distribution (T ≈ 20°C) at t = 0 s, while **Figure 3.19 c** shows a noticeable temperature increase (T ≈ 40°C, under the irradiated area) at t = 20 s due to photo-induced thermal effect. The control experiment (same experimental conditions) performed on a regular CLC sample did not show any significant temperature variations. This result is incontrovertible evidence that the photo-induced heat generation can only be associated with the LSPR mechanism (plasmonic-assisted photo-thermal heating). Noteworthy, the reported blue shift (**Figure 3.19 a)** shows the possibility to realize an LC-based plasmonic device having a light controllable plasmonic resonance. Moreover, the same system can be integrated into modern photonic devices such as controllable light filters and smart mirrors.

3.3.2 Thermoresponsive Hydrogel

Temperature-responsive hydrogels have been used extensively in recent years for numerous bio-based applications. Hydrogels are now widely used as biomaterials. These materials are biocompatible because their physicochemical properties are similar to those of the living tissues, e.g., high water content, soft and rubbery consistency, and low interfacial tension with water or biological fluids. Among them, poly(N-isopropylacrylamide-co-N-isopropylmethacrylamide) P(NIPAm-co-NIPMAm) is a water-based, temperature-sensitive material that undergoes in reversible phase transitions (coil-to-globule type transition)[166] (**Figure 3.20**) at critical temperatures.[167] PNIPAM has been used for drug-release experiments[168] due to its capacity to become hydrophobic from hydrophilic above a critical temperature (≈ 37°C).[169] Combining the strengths of hydrogel and AuNPs, with unique stimuli responsivity, PNIPAM microgels have found numerous biomedical applications, such as biosensing and PPTT[94]. PNIPAM embedding AuNRs has been synthesized[170] to develop theranostic nanoplatforms with photothermal and thermo-responsive properties for novel tumor-targeting strategies.

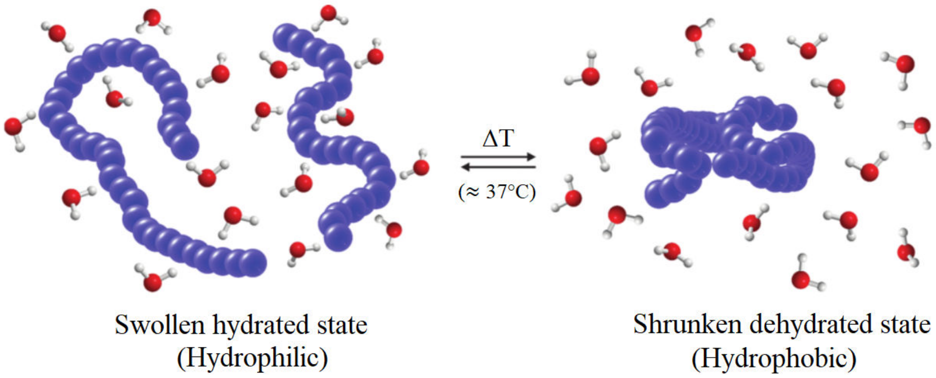

***Figure 3.20** – Scheme showing a thermoresponsive polymer reaction in aqueous solution.*

Differently from other classes of hydrogels, the hydrogel family based on poly (N-isopropylacrylamide), like P(NIPAm-co-NIPMAm), is well known for its chemical and structural stability even at elevated temperatures, thus exhibiting a very long shelf life.[171]

For this reason, P(NIPAm-co-NIPMAm)-based materials have found applications in other research fields where robustness and mechanical stability are required such as optics,[172] solar energy,[173] electronics,[174] catalysis,[175] and sensing.[176]

The unique combination of Au nanostructures' optical properties and the smart behavior of thermosensitive polymer in the form of Au-hydrogel is increasing its demand continuously.[177] In the next section, a few mm thick, optically clear, and light-responsive hydrogel composed of gold NPs uniformly dispersed in a P(NIPAm-co-NIPMAm) film will be illustrated. The polymer, changing from the hydrophilic to the hydrophobic state, due to the presence of AuNPs nanoheaters, undergoes a release of water inducing a drastic change in the optical transparency (from clear to opaque) of thin films. This film is optically activated/deactivated by exploiting the photothermal properties of AuNPs, enabling the development of an efficient light-triggered and dynamic optical beam attenuator, as well as the possibility to control and detect the photo-induced heat from the dispersed AuNPs.

3.3.2.1 Application: Thermoplasmonic-activated hydrogel based dynamic light attenuator

In this section, it is shown how the light-induced thermoplasmonic heating of GNRs can be used to control the optical scattering of an initially transparent hydrogel poly(N-isopropylacrylamide-*co*-N-isopropylmethacrylamide) P(NIPAm-*co*-NIPMAm) film. A hydrated P(NIPAm-co-NIPMAm) film is optically clear at room temperature. When heated to temperatures over 37°C via light irradiation with a resonant source (λ=810nm) to the GNRs, a reversible phase transition from a swollen hydrated state to a shrunken dehydrated state occurs (**Figure 3.20**). This phenomenon causes a drastic and reversible change in the optical transparency from a clear to an opaque state. A significant red shift (≈30nm) of the longitudinal band can also be seen due to an increased average refractive index surrounding the GNRs. This change is in agreement with an “ad-hoc” theoretical model that uses a modified Gans theory (see paragraph 1.5.2) for ellipsoidal NPs. This smart device can be easily integrated into several modern optical applications such as smart windows and light-responsive optical attenuators, at the same time used to control and monitor the photothermal heating at the nanoscale.

Realization of the hybrid device

In this work, we used rod-like GNPs (GNRs) instead of nanospheres as in the previous works shown above. Citrate-stabilized, water-based, GNRs were synthesized using a slightly modified protocol for the seed-mediated synthesis reported in detail elsewhere.[178]

A hydrogel (poly(N-isopropylacrylamide-co-N-isopropylmethacrylamide) (P(NIPAm -co-NIPMAm))) made of 95 wt% water and 5wt% of polymer was used. The precursor solution (4 ml) consisted of 231.25 mg of NIPAm (Poly(N-isopropylacrylamide), from Sigma-Aldrich), 6.25 mg of NIPMAm (N-isopropylmethacrylamide, from Sigma-Aldrich), 12.5 mg of BIS (N,N’-methylene bisacrylamide, from Roth), and 50.0 mg of Irgacure 2959 UV photo-initiator (from Sigma-Aldrich). The solution, placed in a glass vial and protected from ambient light, was stirred overnight. Subsequently, 1.0 ml of the GNRs solution was added to the polymer precursor solution.

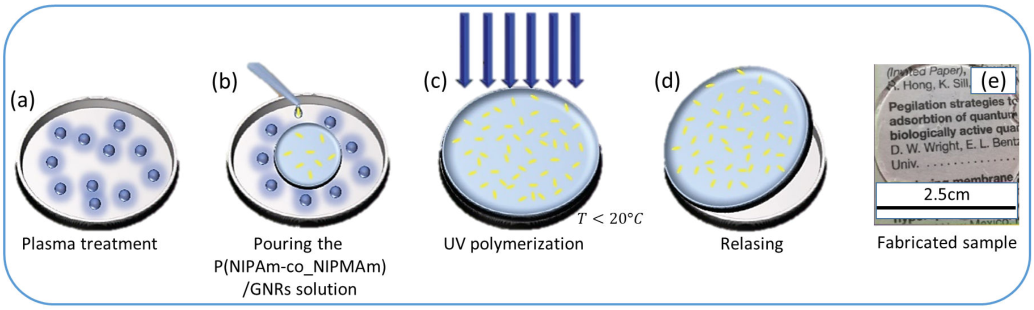

Figure 3.21 *– Step by step fabrication process of the P(NIPAm-co-NIPMAm)/GNRs sample.*

In order to fabricate flat discs with excellent optical quality, Petri dishes (WillCo-dish ®, GWSt-5030) with 30 mm diameter were treated using an oxidation plasma (by Diener Electronic GmbH-Co. KG, Zepto) for 15 min (**Figure 3.21 a**).

The P(NIPAm-co-NIPMAm) /GNRs solution was deoxygenated for 10 minutes via Argon bubbling, and then 0.5 ml of solution was poured into each Petri dish (**Figure 3.21 b**). To keep the temperature below 20°C during the photopolymerization process, the Petri dishes were put into an ice bath before illuminating (**Figure 3.21 c**) the samples from the top for 1 minute by UV light (by Dymax Europe GmbH, 5000-PC). The P(NIPAm-co-NIPMAm)/GNR discs were gently detached (**Figure 3.21 d**) from the Petri dishes and stored in water at room temperature. **Figure 3.21 e** indicates excellent optical transparency of the sample deposited on a glass substrate (the text behind the sample can be easily read).

Morphological and spectral analysis

Figure 3.22 a shows the absorption spectrum of the GNR solution ($C=3.2\times10^{-9}M$) with longitudinal (λ_L) and transversal (λ_T) LSPR bands centered at 775nm and 524nm, respectively. **Figure 3.22 b** shows the free charge distribution in an elongated NP associated with the LSPR mechanism. **Figure 3.22 c** is a representative high-resolution transmission electron microscope (TEM) image of GNRs. They are highly monodisperse with an average aspect ratio of around 3.6.

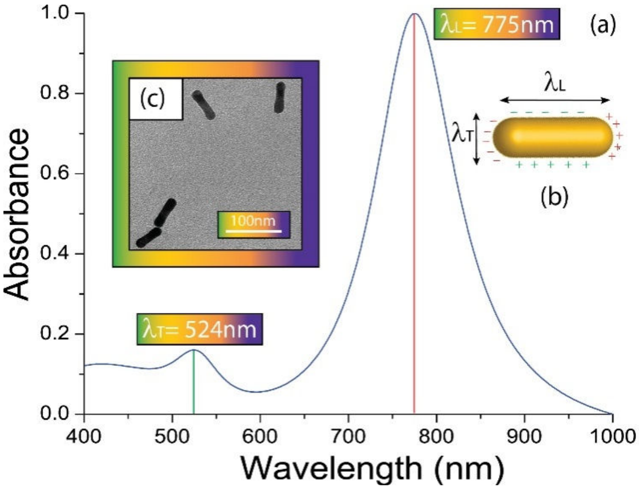

Figure 3.22 *– Absorption spectrum of a water-based GNR solution (a) along with a schematic representation of the LSPR mechanism in GNRs (b). High-resolution TEM image of GNRs (c).*

The morphology of the P(NIPAm-co-NIPMAm)/GNR samples (**Figure 3.21 e**) was investigated employing a field emission scanning electron microscope (FE-SEM, Nova NanoSEM 450, FEI) operating at an accelerating voltage of 10 kV. Samples were freeze-dried and coated with an 8 nm-thick gold layer before their characterization, to minimize charges. In order to study the GNRs distribution, samples were inspected by a transmission electron microscope (TEM, FEI Talos F200X - 200 kV). Samples were first freeze-dried, then the lyophilized materials were cut into small pieces, immersed in ethanol, and placed on a copper mesh with an amorphous carbon membrane. The samples were dried in a vacuum for 4h.

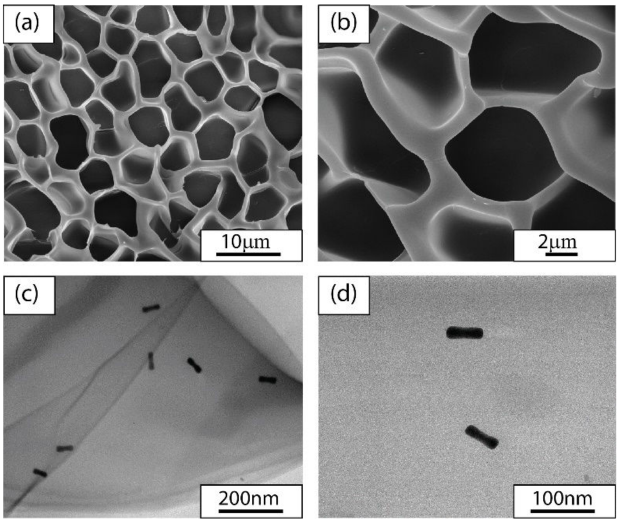

***Figure 3.23** – FE-SEM (a, b) and TEM (c, d) analysis of the P(NIPAm-co-NIPMAm)/GNRs sample for different magnifications.*

Figure 3.23 a-b show FE-SEM micrographs indicating a honeycomb-like architecture composed of uniformly distributed pores with an average size of a few microns. The presence of GNRs does not affect the conventional morphology of the P(NIPAm-*co*-NIPMAm) film as this morphology is similar to the previously reported system without GNRs.[179] **Figure 3.23 c-d** show TEM images indicating well dispersed and randomly aligned GNRs within the P(NIPAm-co-NIPMAm) matrix, without the evidence of GNRs agglomeration. In order to check the stability of the P(NIPAm-co-NIPMAm)/GNR samples after a prolonged storage time in water, we performed a detailed characterization of the morphological and optical properties (as shown in the last section).

Photo-thermal analysis

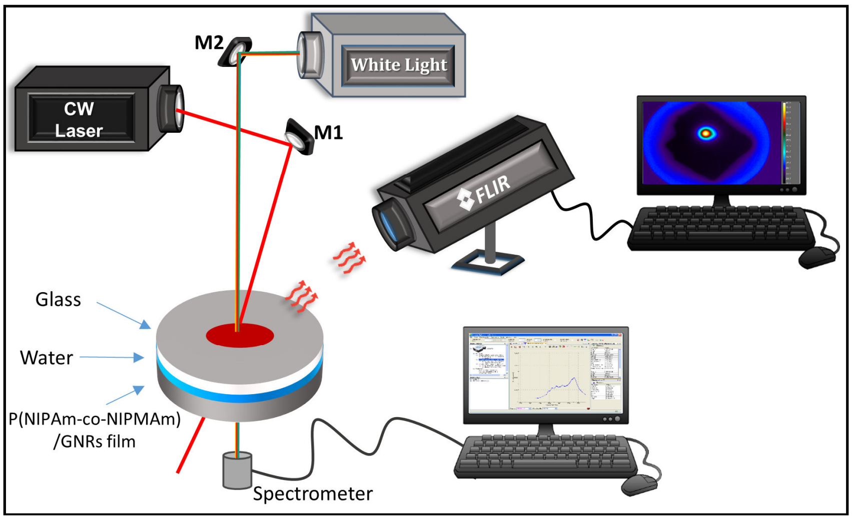

***Figure 3.24** – Thermo-optical setup for sample characterization.*

Light-triggered experiments were conducted using the thermo-optical setup illustrated in **Figure 3.24**. This setup uses a CW pump laser (Coherent Inc.) operating at 810 nm (within the LSPR of these GNRs (**Figure 3.22 a**)), a collimated white light source (CLS 100, Leica), a spectrometer (USB 2000, Ocean Optics) for monitoring both spectral response and light attenuation behavior, and a thermal camera (A655sc, FLIR) for mapping and measuring temperature changes in the sample under laser beam illumination.

The P(NIPAm-co-NIPMAm)/GNR samples were covered with a glass slide (100 µm thick) and the gap, controlled via 50 µm glass microspheres, was infiltrated with water. The water film acts as a reservoir to keep the samples hydrated, which is a requirement for their functionality as optical components.

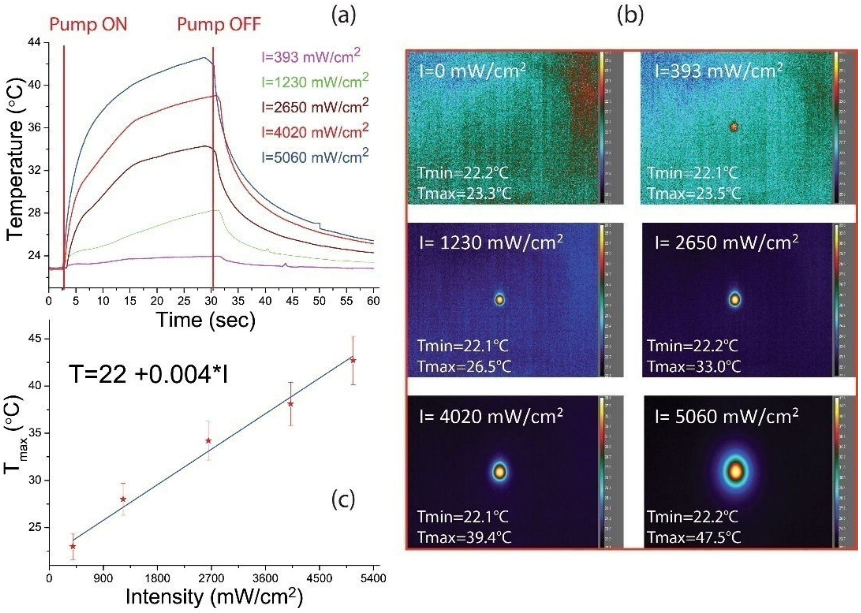

***Figure 3.25** – Time-temperature dependence of the P(NIPAm-co-NIPMAm)/GNRs sample under pump beam illumination (a) along with the corresponding thermographic view (b). Linear fit of the maximum temperature versus the intensity of the pump beam (c). T_{min} and T_{max} indicate the maximum and minimum temperature of each color scale reported in (b).*

Figure 3.25 a shows that there is a significant and gradual temperature increase up to 44°C upon illumination (Pump ON) at different intensity values of the pump beam (from 393mW/cm^2 to 5060 mW/cm^2) because of the photo-thermal conversion of GNRs. The sample cools back down to room temperature as soon as the pump beam is turned off (Pump OFF). The curves shown in **Figure 3.25 a**, were obtained by processing the thermal images in **Figure 3.25 b** with a proprietary software program (FLIR Research IR Max). **Figure 3.25 c** shows a linear correlation between the maximum temperature (obtained from the curves shown in **Figure 3.25 a**) and the intensity of the pump laser. This linear behavior is well in agreement with the theory reported in detail in paragraph 2.2, equation (2.24).

Temperature values were obtained by measuring the temperature with the thermal-camera (see the thermo-optical setup in **Figure 3.24**) on the surface of the glass slide (100 µm thick) covering the P(NIPAm-co-NIPMAm)/GNR samples. Samples are quite thin (few millimeters thick), and for this reason, we are confident that the difference between the temperature of the surface and that in the bulk of the sample is less than few degrees. The additional experiments (not shown here), performed without GNRs on similar samples, did not show any significant temperature change, thus confirming the capability of GNRs to convert the incident, resonant, light into heat.

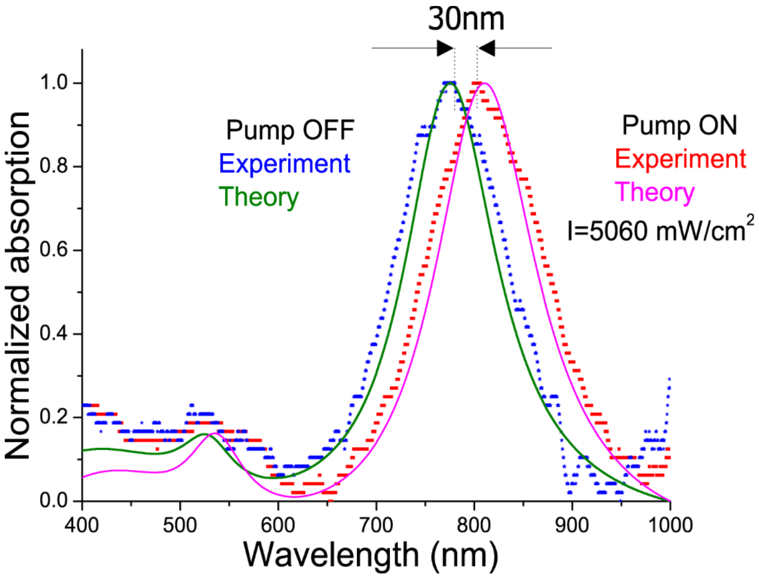

Figure 3.26 *– Theoretical (green and magenta) and experimental (blue and red) absorption spectra of the P(NIPAm-co-NIPMAm)/GNRs sample without (green and blue) and upon (magenta and red) pump beam irradiation.*

In order to understand the influence of the photo-thermal heating on the spectral position of LSPR bands, the spectral response of the samples was investigated. When photo-heated to temperatures above 37°C a significant red shift (≈30nm) (**Figure 3.26**, blue and red curves) of the longitudinal band, due to an increase in the average refractive index of the medium surrounding the GNRs (from hydrated n≈1.4 to dehydrated P(NIPAm-co-NIPMAm) n≈1.5), can be observed. At room temperature with the water reservoir keeping the P(NIPAm-co-NIPMAm)/GNRs film hydrated, the refractive index was roughly estimated as an average between the refractive index of the water (n≈1.3) and that of the P(NIPAm-co-NIPMAm)/GNRs composition (n≈1.5). Upon illumination (I= 5060 mW/cm^2) a phase transition from a swollen hydrated state to a shrunken dehydrated state occurs, producing an increased refractive index (1.5 instead of 1.4). This result is in agreement with the theoretical model which uses a slightly modified Gans theory[180], that start from equation (1.27) and consider the average absorption cross section $\langle C_{abs} \rangle$ for a 3D configuration[35], for ellipsoidal, NPs (randomly oriented) (**Figure 3.26**, magenta and green curves). It is worth pointing out that because of the low sensitivity to refractive index variations, the transversal band is red-shifted by only a few nanometers.

Light attenuation analysis

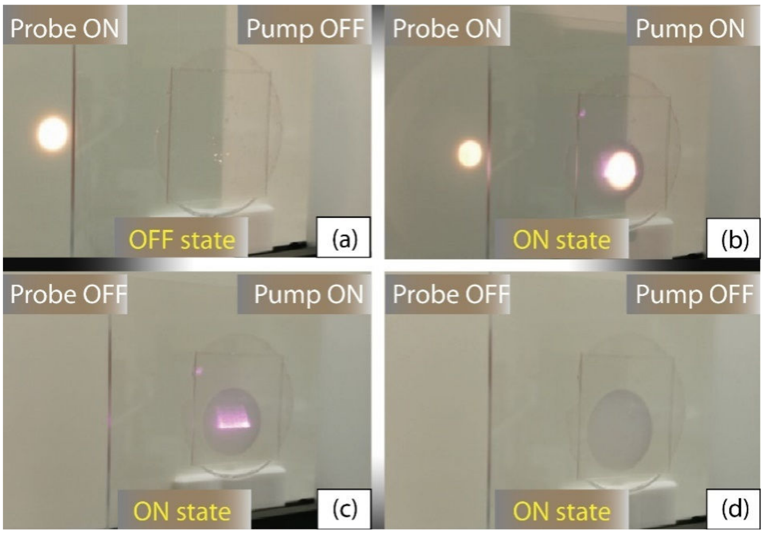

Figure 3.27 *– Photos of the P(NIPAm-co-NIPMAm)/GNRs sample in the OFF (a) and ON (b, c, d) states for different combinations of the probe and pump beam.*

The ability of these films to work as a dynamic attenuator was tested by probing the samples with a collimated white light source while turning the pump beam ON and OFF on the same probed area. These experiments were performed using the optical setup illustrated in **Figure 3.24**. It makes use of a CW laser operating at 810 nm (pump beam) and a collimated white light source (probe beam). With the pump beam OFF (**Figure 3.27 a**) the sample is optically clear, and all the incident probe light is transmitted producing a visible white spot on the post-mountable view screen. When the pump beam is turned ON (I=5060 mW/cm^2) there is a drastic change in the optical transparency due to the scattering of the incident probe light (**Figure 3.27 b**). The photo-thermal-induced phase transition is driven by a morphological change of the P(NIPAm-co-NIPMAm) film which transforms from a straight to a shrunken conformation of the chains at temperatures above 37°C.

The photo-thermal-activated area of the sample is more evident in **Figure 3.27 c** and 7d, where the probe beam and the probe/pump beams were turned OFF, respectively. Note: the photo shown in **Figure 3.27 d** was quickly acquired immediately after the pump beam was turned OFF. Samples show excellent optical reversibility and start to go back to the initial (transparent) state as soon as the pump beam is turned OFF.

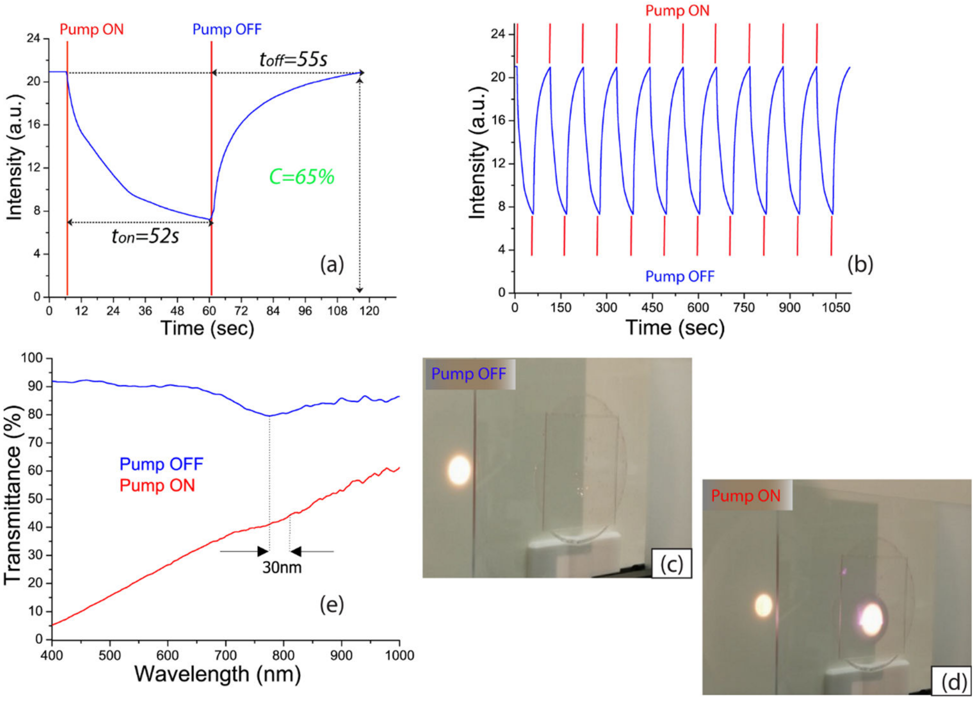

Figure 3.28 *– Reversible change of the transmitted intensity (a, 1 cycle), (b, 10 cycles) induced by turning the pump beam ON (c) and OFF (d). Transmission spectra of sample (e) by turning ON (red curve) and OFF (blue curve) the pump beam.*

Figure 3.28 a shows the transmission dynamic response of the sample obtained by measuring the transmitted probe light intensity while turning the pump beam ON (I= 5060 mW/cm^2) and OFF. The contrast ratio (C) – defined as the ratio of the transmitted intensity with the pump beam OFF (**Figure 3.28 c**) to the incident intensity with the pump beam ON (**Figure 3.28 d**) – in percentage, is 65%. Response times (on and off) are 52 s and 55 s, respectively. **Figure 3.28 b** shows the exceptional reversible and repeatable change of the optical response of the sample induced by a sequence of pump beam light pulses (10 cycles). Moreover, it is worth pointing out that the optical response of the P(NIPAm-co-NIPMAm)/GNR samples shows good reversibility even after a long storage time in water (as shown in the next paragraph). Transmission spectra reported in **Figure 3.28 e** acquired by turning ON (red curve) and OFF (blue curve) the pump beam (I=5060 mW/cm^2) evidence the capability of the sample to attenuate the incident (unpolarized) probe white light in a relatively large spectral range (from 400 to 800 nm) with an average C of about 65%. In addition, as previously discussed (**Figure 3.26**), there is an evident red-shift (≈30 nm) of the longitudinal λ_{LSPR}. Noteworthy at room temperature (**Figure 3.28 e**, blue curve) the transmission of the sample is higher than 90%, thus confirming its extraordinary optical quality in terms of optical transparency; in this condition, the transmission does not depend on the wavelength. Conversely, when the sample, triggered by the laser pump (**Figure 3.28 e**, red curve), becomes opaque, Rayleigh scattering occurs. Therefore the more the wavelength increases, the less the material scatters the light and vice versa. The spectral properties of the P(NIPAm-co-NIPMAm)/GNR samples are not affected by the prolonged hydration. A detailed characterization of the sample properties for different hydration times (up to 45 days), and different photo/switching cycles, is reported below.

P(NIPAm-co-NIPMAm) and GNRs stability analysis

The stability of the P(NIPAm-co-NIPMAm) /GNR samples after a prolonged storage time in water was verified by performing a detailed characterization of the morphological and optical properties. Four identical samples were fully immersed in distilled water and investigated at t= 0 days, t= 1 day, t= 30 days, t= 45 days by a: i) field emission scanning electron microscope (FE-SEM); ii) UV-Vis spectrophotometer; iii) pump-probe optical setup. Moreover, Samples were inspected by TEM in order to verify if the light-induced thermal heating can produce detectable changes (reshaping) of GNRs.

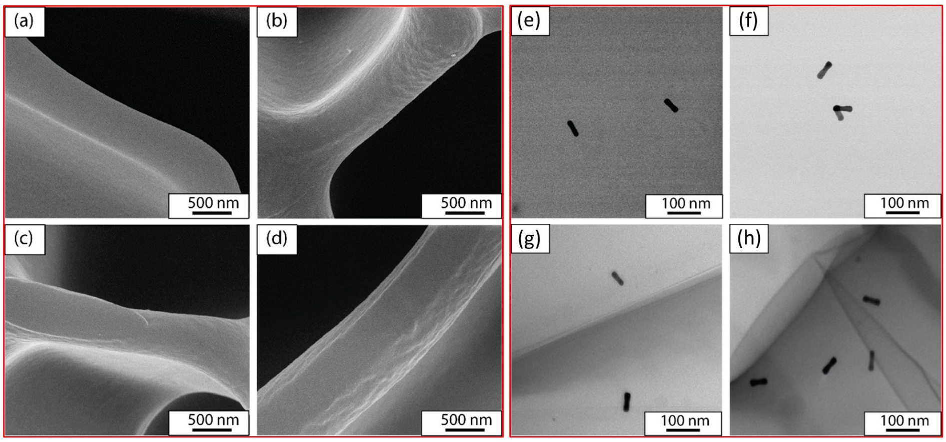

Figure 3.29 *– (a-d) FE-SEM analysis of the samples at different hydration times: t= 0 days (a), t=1 day (b), t=30 days (c), t=45 days (d). (e-h) TEM analysis of the samples after different cycles of photo-switching experiments: (e) 0 cycles; (f) 1 cycle; (g) 5 cycles; (h) 10 cycles.*

Figure 3.29 (**a-d**) clearly shows that the prolonged immersion in water does not affect the morphology of the P(NIPAm-co-NIPMAm) film. Indeed, no presence of structural defects is visible at this level of magnification, thus highlighting the extraordinary capability of the P(NIPAm-co-NIPMAm) material to retain its morphological properties even after 45 days of continuous hydration. **Figure 3.29** (**e-h**), confirms that even after cycling the samples up to 10 times (**Figure 3.29 h**), the shape of GNRs turns out to be very similar to the one observed before the photo-switching experiments (**Figure 3.29 e**). This is clear evidence that GNRs are stable under the resonant light beam illumination and the reshaping process of GNRs is completely absent.

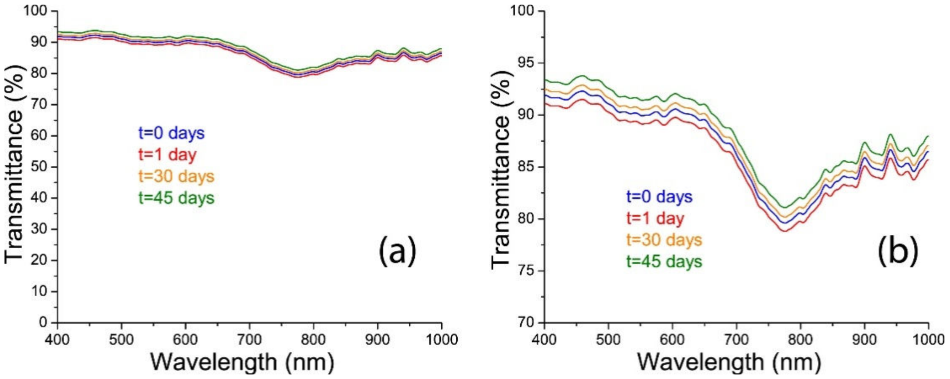

Figure 3.30 *– Spectral response of the samples at different hydration times (a) along with a detailed view of the same graph (b).*

The spectral response (**Figure 3.30**) confirms that the transmission properties of the samples are not affected by the prolonged hydration. As such, the change in the transmittance is less than 2-3% and this small change can be ascribed to the intrinsic experimental error of the utilized optical setup. This result clearly evidences that there is no evidence of critical instability of P(NIPAm-co-NIPMAm) material after prolonged storage times in water.

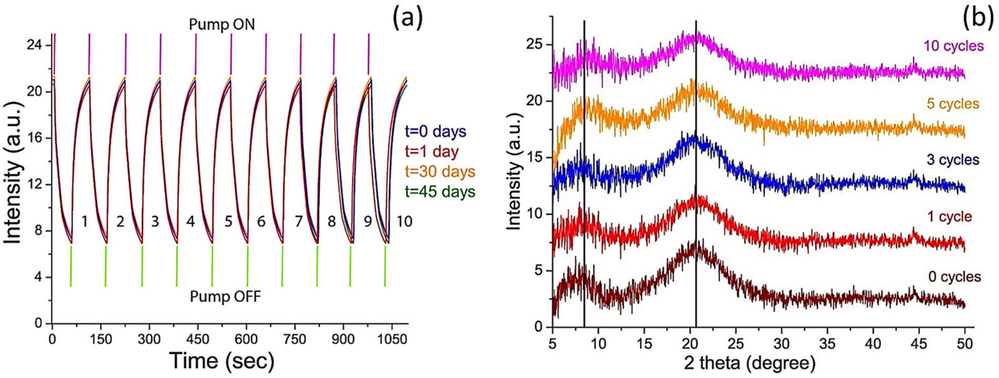

Figure 3.31 *– (a) Reversible change of the transmitted intensity of the samples induced by cycling (from 0 to 10) the pump beam ON and OFF. (b) Wide angle X-ray scattering (WAXS) samples analysis at different cycles of photo-switching experiments.*

Photo-switching experiments (by cycling the sample up to 10 times) at each hydration time were conducted using the optical setup described in **Figure 3.24**.

Figure 3.31 a shows notable reversibility of the transmitted intensity and no change in the optical properties in terms of response times and optical contrast is observed for all the investigated samples. It is worth pointing out that the small offset between the four curves reported in **Figure 3.31 a** can be attributed to the experimental difficulty to set the same initial intensity value for each measurement.

In order to investigate the chemical structure of the P(NIPAm-co-NIPMAm) material and detect any potential change in matrix structure after different irradiation cycles, wide angle X-ray scattering (WAXS) analysis was performed by means of a Bruker D8 Discover diffractometer. Measurements were carried out in reflection mode, using Bragg-Brentano geometry in the angular range (2 theta) between 5 and 50 degrees, with a step of 0.02 degrees. The time of data accumulation at a particular angular point was 1.0 s. **Figure 3.31 b** (wine curve) shows the WAXS diffractogram of the sample before any photo-thermal experiment. The sample exhibits two wide peaks centered at 8°and 21° which can be attributed to the amorphous structure of the polymer.[181] Further measurements performed on the same sample after some cycles of illumination show identical WAXS patterns, thus confirming that there has been no change in the structure of the P(NIPAm-co-NIPMAm) material. It is worth mentioning that the WAXS characterization does not show any peak related to the presence of GNRs because the utilized concentration is under the limit of detection of the instrument.

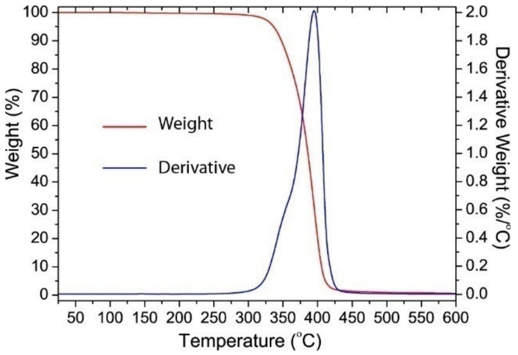

Figure 3.32 *– Thermogravimetric analysis of the sample reporting the weight loss (red curve) and its derivative (blue curve).*

Lastly, in order to stress out the excellent stability of the P(NIPAm-co-NIPMAm)/GNRs samples, a thermogravimetric analysis (TGA) was performed. TGA was carried out by using a TA Instruments SDT Q600 to investigate the thermal stability of the plasmonic hydrogel. The TGA analysis was performed placing around 5.0 mg of sample in an Al_2O_3 pan. The test was carried out by increasing the temperature from 25 °C to 600 °C at a rate of 10 °C/min under a nitrogen flow (100 ml/min) and weighing the sample simultaneously. **Figure 3.32** shows that the sample is completely stable up to 300 °C. After that point, there is a noticeable weight loss (red curve) which is evidenced by the increase of its derivative (blue curve).

In conclusion, the proposed P(NIPAm-co-NIPMAm)/GNRs optical attenuator offers flexibility, light responsivity, optical transparency (OFF state), mechanical stability, long-lasting functionality, reversibility, and last but not least does not require any electrical power. Moreover, thanks to the presence of an integrated water reservoir, we have faced one of the main issues of hydrogel-based materials. Indeed, the water layer keeps the P(NIPAm-co-NIPMAm) film in a hydrated state (OFF state) at room temperature while it acts as a well to run out water from the film (ON state) at high temperature (44 °C), thus enabling a long-lasting functionality and reversibility. Furthermore, the use of a thermosensitive polymer has allowed not only to exploit the photothermal heat but also to monitor it with precision at the nanoscale.

Chapter 4

PLASMONIC PHOTOTHERMAL HEATING BIO-APPLICATIONS

4.1 Plasmonic Photothermal Therapy

Thermoplasmonics has turned metal losses, long assumed to be one of the major drawbacks of plasmonics, into an advantage.[7] And in particular, Plasmonic PhotoThermal Therapy (PPTT) exploiting AuNPs, completely transformed material losses into a powerful nano-heating weapon.

The possibility to exploit AuNPs as nano-sources of heat remotely triggered by light has, nowadays, impacted a wide range of research activities, including nanomedicine, cell biology, photothermal and hot-electron chemistry, solar light harvesting, soft matter, and nanofluidics.[7]

The two main articles that triggered the interest of the scientific community in nanoplasmonic heating for PPTT of cancer were published in 2003.[85, 182] PPTT is a minimally invasive therapeutic strategy in which photon energy from light is converted into heat to destroy cells, avoiding severe infection-related complications that are commonly encountered after surgery, and circumventing the side and non-specific effect of using a toxic drug like in chemotherapy.[86] These two pioneering works relying on specifically delivering plasmonic NPs to cancer tissue and using a subsequent light exposure to induce a local increase in temperature, sufficient to engender cancer cell death while not substantially affecting surrounding healthy tissue. The simplicity of the idea, along with first encouraging preclinical results, rapidly made this concept very appealing.

However, hyperthermia therapy in medicine was already a fairly well-known field. All building blocks of living cells are highly temperature-responsive: lipid layers can undergo phase transitions, proteins can unfold, DNA can melt, and so on. Depending on the induced temperature increment magnitude, heat triggers different biological and physiological mechanisms: from the stimulation of the immune system and partial cell damage to denaturation of proteins and DNA damage. Different thermal treatments and related effects of cancerous tumors can be classified as summarized in **Figure 4.1**.[79]

Over the years, different heat sources have been considered (electrical, microwave, focused ultrasounds, and so on), but one had to wait until the 1960s, after the laser's invention, to see photothermal therapy emerge, an approach that exploits natural light absorption of tissues. In this context, thermoplasmonics can artificially boost light-to-heat conversion in the near-infrared (NIR) region of the spectrum where tissues are more transparent, the so-called biological window.[183] The presence of several absorption bands is used to define two main biological windows: (i) the first biological window (700nm-980nm) corresponds to the spectral range defined between the visible absorption band of hemoglobin and the characteristic 980 nm absorption band of water; (ii) the second biological window (1000nm-1400nm), both limits corresponding to water absorption bands.

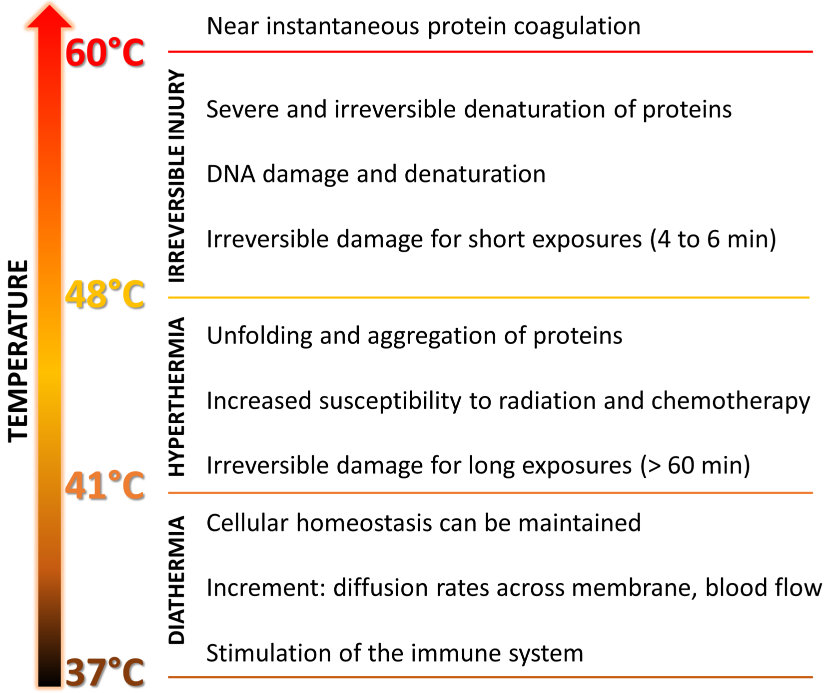

Figure 4.1 *– Schematic diagram of the various effects caused by the different thermal treatments as classified by the corresponding operating temperature.*

AuNPs, as an efficient localized light-to-heat nano-converter, offers several benefits compared with external macroscopic heating. The main incentive for using AuNPs as photothermal agents is to generate heat in nanoscale volumes efficiently within reduced timescales. This asset stems from the combination of four properties of plasmonic materials: (i) the absence of thermo-/photobleaching (unlike common dyes), (ii) a high density of free electrons due to their metallic nature, (iii) low losses for noble metals, (iv) the existence of resonances that enhance light-matter interaction.[7]

These unique properties, combined with the fact that AuNPs are chemically inert, high biocompatible, easy to synthesize, and offer a simple functionalized surface, with optical and physical tunable, make them the best candidates for biomedical applications requiring spatially confined heating, like in PPTT.[86]

Finding the most suitable thermoplasmonic NPs for a specific application is not a trivial task. It often requires compliance with several constraints that can be physical, chemical, or biological. To meet these constraints, there are three free parameters to adjust: the NP size, its shape, and internal/external composition.

A common goal for all applications of thermoplasmonics is to maximize the light-to-heat conversion of the NPs. The optimization of light-to-heat conversion, however, has to compromise with other requirements. Biological and biomedical applications require combining sizes of a few tens of nanometres, which favor cellular uptake, with low toxicity, chemical, physical, thermal stability, and resonances in the NIR biological transparency window.

It must be emphasized that although, thanks to the EPR effect (enhanced permeability and retention) AuNPs with a diameter between 60 and 400 nm can penetrate solid tumors, thus exploiting a passive selectivity mechanism (passive targeting); it is more convenient to generate selective cell targeting, functionalizing the AuNPs surface with appropriate targeting vectors that favor its concentration in the tumor. They have been used in this regard a variety of small molecules and reactive functional groups such as proteins, peptides, antibodies that bind to cancer cells overexpressing receptors.[184]

Interestingly, the photothermal effect can indirectly improve the cellular uptake of AuNPs, increasing both vascular and cell membrane permeability, using local heating. [185] Although PPTT alone is sufficient for medical treatment, synergetic therapies with different therapeutic methods such as radiotherapy, immunotherapy, and chemotherapy have been recently investigated to extremely enhance the therapeutic efficacy of PPTT.[68, 186]

PPTT has recently proven to be useful beyond oncology, like for sterilization and disinfection. Similar to cells, most bacteria viability is altered when experiencing a temperature greater than 45°C. Several methods were proposed to selectively kill bacteria in vitro, based on targeting their wall with bio-conjugated AuNPs, or to eradicate bacterial colonies in the form of biofilms using colloidal solutions of AuNPs or directly anchoring them on a surface.[15, 90, 187] This concept is particularly relevant in the field of disinfection of surgical implants, sterilization of medical instruments,[14] solar inactivation of bacteria in drinking water,[48] and other major health issues arising from the emerging antibiotic resistance.[188]

Almost two decades of research in PPTT have led to great advances. After some first clinical trials for head and neck cancer that were not so conclusive[189], promising prostate cancer outcomes have recently been reported, both in large animals[9] and patients.

However, several major limitations remain to be addressed for in-vivo applications: (i) low targeting specificity that is hindered by protein corona effect that tends to annihilate the specificity of antibodies and other ligands;[190] (ii) low targeting yield that can only rely on the higher permeability of cancer tissue (EPR effect); (iii) AuNPs clearance from filtering organs, especially liver and spleen.

There is a need for more elaborated 3D models based on human tumors grown, which account for key parameters such as tumor vascularization and damage of adjacent healthy tissues and living organs. Simultaneously, there is the need to develop smart and innovative AuNPs, with enhanced targeting capabilities, implemented by combining the inorganic material with compatible and biomimetic biomolecules and improved overall efficacy.

In this chapter, two important applications are presented concerning using AuNPs for PPTT in two different fields. The first application concerns the antimicrobial effect of easy to synthesize, suitably purified, water-dispersible AuNRs on *Escherichia coli* bacteria. The second application instead focuses on a new generation of biomimetic AuNPs capped with keratin (Ker-AuNPs), tested as a promising new tool in the field of biocompatible photo-thermal agents for PPT treatments against human glioblastoma cell line (i.e., U87-MG).

4.2 PPTT as a solution to antibiotic resistance

Antibiotic resistance refers to when microorganisms survive and grow in the presence of specific antibiotics, a phenomenon mainly related to the indiscriminate widespread use and abuse of antibiotics. Currently, multidrug resistance (MDR) has become a serious global health problem, with devastating consequences for patient care.[191]

Therefore, it is mandatory to identify effective strategies for controlling bacteria growth and related consequent diseases. Bacterial infections in humans are mainly caused by mesophilic bacteria that find their optimal growth temperature around 37°C, the regular human body temperature. However, moderate temperatures (30-45°C) have been demonstrated still suitable to promote the mesophilic bacteria growth while higher temperatures (>45 °C) are known to inactivate bacteria viability or proliferation. Therefore, currently, exposure to high temperatures is considered a well-established methodology for disinfecting medical tools and laboratory equipment (e.g., using dry ovens).[192] The same highly efficient approach cannot be translated for treating human (or animal) diseases caused by pathogenic bacteria due to the difficulty to increase body temperature upon suitable activation locally. In this framework, nanotechnology offers the design and fabrication of original bioconjugated, engineered, and actively functionalized AuNPs, a powerful weapon against several diseases such as pathogenic illness.[16, 193-194] In most cases, the anti-microbial effect of NPs is due to their toxicity, which can be intrinsic (due to the NPs effect directly: Ag or TiO_2) or due to a coating effect. Indeed, commercially available AuNPs are typically stabilized with cationic surfactants (e.g., cetyltrimethylammonium bromide, CTAB), which, unfortunately, exhibit a very high intrinsic toxicity.[195]

To overcome these issues, here we propose a simple and effective methodology based on capped GNRs, obtained upon a suitable purification from the excess of CTAB used as a capping agent that aims at investigating the potential hold by GNRs in the development of light assisted antimicrobial therapies. To validate the proposed approach, a strain of *Escherichia coli* (E.coli) has been selected as a representative type of bacteria, having a great impact. It causes severe illness in humans since it is found in the lower intestine of warm-blooded organisms. In particular, an effective approach has been designed and realized to minimize the concentration of GNRs and, accordingly, of CTAB associated with the nanostructures, and still obtaining dispersible GNRs and a sufficiently high temperature (≈ 50°C) suited to reduce the E.coli population of about 2 log CFU. Such a result not only represents an excellent starting point for realizing in vivo light assisted antimicrobial therapies but also demonstrate to be fully compliant to the typical standard[196] required for antimicrobial treatment in health care facilities.

4.2.1 Thermo-Plasmonic killing of *Escherichia-coli* TG1 bacteria

Herein, we demonstrate an antimicrobial methodology based on the properties of gold nanorods (AuNPs or GNRs). Under resonant laser irradiation, GNRs become highly efficient light to heat nano-converters extremely useful for PPT applications. The concept here is to assess the antimicrobial effect of easy to synthesize, suitably purified, water-dispersible GNRs on E. Coli bacteria. A control on the GNRs concentration used for the process has been demonstrated critical to rule out cytotoxic effects on the cells, and still, to be able to generate, under a NIR illumination, an adequate amount of heat suited to increase the temperature up to ≈ 50 °C in about 5 minutes. Viability experiments evidence that the proposed system accomplishes a killing efficiency suitable to reduce of about 2 log CFU (Colony-Forming Unit) the E. Coli population.

Gold Nanorods and E.Coli Bacteria

Cetyltrimethylammonium bromide (CTAB) capped, water-dispersible, GNRs have been synthesized employing a seed-mediated protocol reported in detail elsewhere.[197] Shortly here, we report that the GNRs samples (C = 3 x 10-9 M, determined by utilizing a standard spectroscopic (absorption) technique) have been carefully purified from the excess of CTAB by several centrifugation cycles to reduce the intrinsic cytotoxicity, mainly exhibited by the non-conjugated CTAB.

Escherichia coli TG1 (E.coli), has been selected as Gram-negative bacterium. E.coli has been grown aerobically at 37 °C with shaking in sterile Luria Bertani (LB) broth (normal rich growth medium: NaCl 5 g/L; yeast extract 5 g/L; trypton 10 g/L). E. coli solution has been diluted (1:100 v/v) in 20 mL of fresh LB liquid medium to restart the cell cycle. After 3 h of incubation at 37 °C the cells have been synchronized at the log phase of the growth curve, featured with the optical density at 600 nm (OD600) of 0.4-0.6. At this OD value, the growth rate is constant, and the cells are already dividing and result metabolically active. 5.9 µl of GNRs have been added in 195.5 µl of E.coli (C = 106 CFU/mL) so that the final concentration of GNRs was about 8.76 x 10^{-11} M. The culture has been kept for 6 h at 37 °C. At 1, 2, 3 and 6 h serial dilutions of the culture have been made, and 50 µl of each dilution have been cultured onto sterile LB agar (LB broth + agar 16 g/L) and incubated at 37 °C. After 16-18 h, the number of colonies on each plate has been determined to get the corresponding concentration of living bacteria. The log N cells has been calculated by counting the CFU and using the formula: CFU/mL = (N° of colonies x dilution factor) / volume of culture spread. The same assay procedures have been used as those described above for the strain cultures without GNRs.

Morphological and spectral analysis

Morphological experiments performed with a transmission electron microscopy (TEM, by Jeol JEM-1011 microscope, Jeol, Peabody, MA, USA, operating at 100 kV) indicated that the NP population consists of GNRs (14 x 70 nm) with an aspect ratio of about 5.1. As anticipated in the material and methods section, the GNRs were purified from the excess of CTAB by several centrifugation cycles to reduce the intrinsic cytotoxicity, mainly exhibited by the non-conjugated CTAB. To do so, we have prepared three different

GNRs solutions labeled A, B, C through subsequent post-synthesis washing/centrifugation cycles at 6000 rpm, using MilliQ water as a washing agent. In particular, the solutions A, B, and C were obtained from the as-synthesized GNRs upon 1, 2 and 3 washing/centrifugation cycles, respectively, to progressively remove the non-conjugated CTAB molecules used to stabilize the GNRs surface.

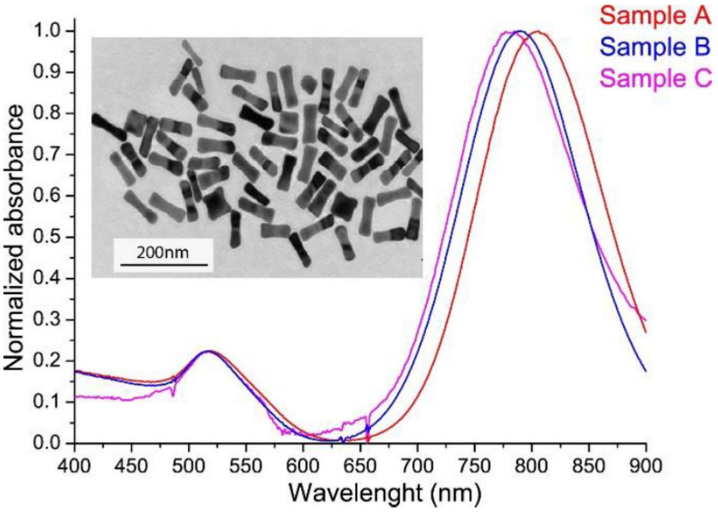

***Figure 4.2** – Samples normalized spectral response along with a representative TEM image.*

The three solutions were step by step characterized by absorption spectroscopy and their surface charge was measured by Z-potential analysis.

***Tab 4.1** – Zeta-potential of the samples along with the wavelengths of the transverse and longitudinal LSPR peaks.*

Sample	Zeta potential (mW)	Transverse LSPR peak (nm)	Longitudinal LSPR peak (nm)
A	27.7	517	804
B	9.7	517	788
C	-6.3	517	779

The absorption spectra of the three solutions (C = $3x10^{-9}$ M) reported in **Figure 4.2** evidenced the presence of two distinct bands corresponding to the transverse and longitudinal LSPR peaks. Particularly, the longitudinal peak exhibited a progressive blue shift from 804 nm (**Figure 4.2**, sample A, red curve) to 779 nm (**Figure 4.2**, sample C, magenta curve) while the transverse peak did not exhibit any relevant shift. This behavior could be explained by considering that the optical properties of ellipsoidal NPs were predicted using the Gans theory (see **Section 1.5.2**) framework. The wavelength shift could be explained by taking into account that the longitudinal band of GNRs is very sensitive to the refractive index of the medium surrounding the GNRs. In the actual case, by progressively removing the residual CTAB there is a gradual reduction of the average refractive index surrounding the GNRs. The blue shift of about 25 nm (see **Tab 4.1**) was consistent with the removal of residual CTAB. Indeed, the refractive index of CTAB was 1.4 while that of water was 1.33. Due to the low sensitivity to refractive index variations, the transverse band did not exhibit any visible shift; thus, this behavior highlights the high sensitivity of the longitudinal LSPR band to variation of the refractive index of the surrounding medium. **Figure 4.2** (inset) shows a representative TEM image, it indicates that the NP population consisted mainly of GNRs with a 5.1 ± 0.3 aspect ratio. The Z-potential values reported in **Tab 4.1** evidenced a variation of the electrokinetic charge from +27.7 mV (sample A) to –6.3mV (sample C), confirming the removal of the positive charged CTAB molecules.

The influences of GNRs on the E.coli morphology has been investigated by means of a SEM. Samples for field emission scanning electron microscopy (FE-SEM Zeiss-Sigma, operating at 10KV, Working distance 3.9 mm) have been prepared by dehydrating both E.coli and E.coli/GNRs solutions on silicon chips, using 70, 80, 90, 95, and 100% ethanol, respectively, for 10 minutes steps. Subsequently, samples have been fixed by using a 3% Glutaraldehyde in PBS, pH 7.3 solution, and let to dry overnight. Finally, a thin layer of Au (15 nm) has been sputtered just before inserting the samples in the SEM vacuum chamber for reducing the charging effect because of the electrons beam accumulation.

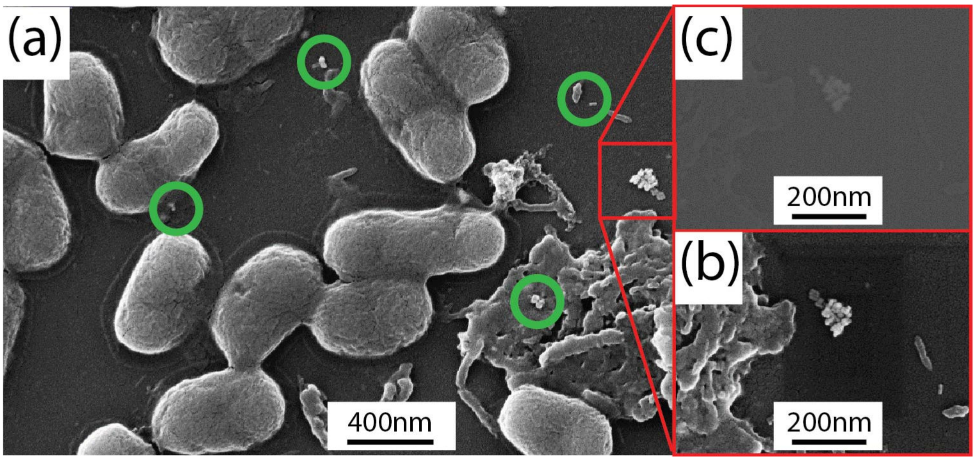

Figure 4.3 *– SEM micrograph of the E.coli/GNRs solution deposited on a silicon chip (a) along with a higher magnification micrograph acquired with the in-lens (b) and BSE (c) detectors, respectively, in split operational mode.*

In **Figure 4.3**, the SEM micrograph of the E.coli/GNRs sample shows the typical elongated shape of E.coli. The average longitudinal dimension is 1.4 ± 0.4 μm (for 90 counts), compatible with the values found in a similar investigation performed on dehydrated E.coli.[198] In **Figure 4.3 a** isolated GNRs are evident (green circles and red square) placed quite far away from bacteria. A higher magnification observation performed in correspondence of red squared region, with both “in-lens” and backscattered electrons (BSE) detectors, in split mode, results in the micrographs reported in **Figure 4.3 b** and **c**, respectively. Since BSE signal strongly depends on the average atomic number (Z) of the specimen, the presence of gold (Z ≈ 80) results in a contrast higher than that of the surrounding bacteria (Z ≈ 20) and therefore the GNRs aggregates (**Figure 4.3** (**a**), red square) appear brighter in **Figure 4.3 c**. Significantly, no GNR has been detected at the bacteria surface, while only few GNRs are detected in the area, without any concomitant relevant alteration of E.coli morphology induced by the exposure to the GNRs. The presence of only few GNRs (**Figure 4.3 a**) can be reasonably accounted by the loss of a large fraction of GNRs as a consequence of the multiple washing cycles performed with ethanol in order to completely dry the bacteria.

Biocompatibility assessment

The toxicity of GNRs has been investigated by performing viability experiments, with and without GNRs. **Figure 4.4 a** shows a comparison of the cell viability between the E.coli (red curve) and E.coli/GNRs (blue curve) at different incubation times. In both cases, regular cell growth is evident, thus pointing out that under the tested experimental conditions cell viability and proliferation do not appear to be significantly affected either by GNRs concentration value and the CTAB molecules present at their surface. A detailed characterization of the E.coli viability in presence of GNRs at different stages of their purification level of residual CTAB is reported in the inset of **Figure 4.4 b**. Results evidenced that, although the first purification cycle, sample A (red curve) still exhibited very high cytotoxicity due to the high concentration of residual CTAB. Samples B (blue curve) and C (magenta curve) did not affect (at all) both cell viability and proliferation. It is important to say that for our experiments we have used the sample labeled B because it exhibited both low concentration of residual CTAB and positive Z-potential, ensuring both negligible toxicity and high colloidal stability.

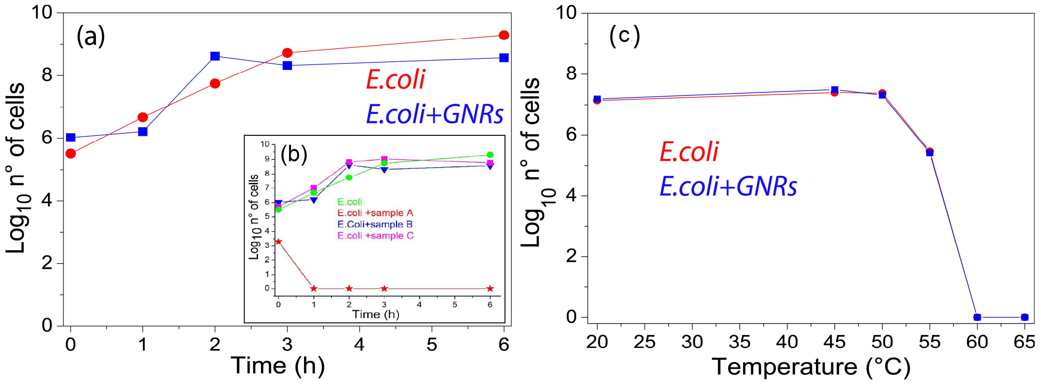

Figure 4.4 *– (a) Viability experiments without (red curve) and with (blue curve) GNRs ($C=8,76x10^{-11}M$) at different incubation times. In the inset (b) viability experiments without (green curve) and with (red, blue, and magenta curves) the three different GNRs solutions at different incubation times. Viability test (c) without (red curve) and with (blue curve) GNRs at different temperatures after 5 minutes of incubation time.*

Thermal treatment experiments have been performed in order to investigate the influence of temperature on cell viability. For this purpose, 500 µl of 1.38 x 10^7 CFU/mL E.coli have been deposited on glass slides undergoing a gradual temperature increase from 20°C to 65°C by using a hot-plate, without, however, considering the temperature interval from 25°C to 40°C, where bacteria are expected to grow.

At each scheduled time interval, a defined volume of E.coli solution has been withdrawn from the glass slide and a series of dilutions (from 10^{-1} to 10^{-5}) has been made by using LB broth. Subsequently, 50 µl of each diluted sample have been cultured out onto sterile LB agar and incubated a 37 °C to investigate cell viability. **Figure 4.4 c** (red curve) shows the typical curve the E.Coli temperature-dependent growth. As the temperature increases, exceeding the optimum growth temperature (≈ 37°C), a decrease in the cell number is observed until they reach a death-point at about 60°C, induced by the rapid denaturation of proteins. The same experiment performed in presence of GNRs does not show any significant difference, since the two curves almost overlap (**Figure 4.4 c**, blue curve). Overall the bacterial growth seems no to be affected after the incubation with the GNRs (**Figure 4.4 a**).

Photo-thermal analysis

The thermo-optical setup (**Figure 4.5**) used for this purpose is based on a CW diode laser (Coherent Powerline, I=6.3 W/cm^2) operating at 810 nm in the high absorption region of GNRs spectrum, corresponding to the $\lambda_{LSPR,longitudinal}$=788nm. The laser beam has been focused using a 10 cm focal length lens in the central part of the Eppendorf tube (spot size ≈ 2 mm). A high-resolution thermal-camera has been used for mapping and identifying (side view) both the heating spatial distribution and the temperature profile under top-pumping laser illumination.

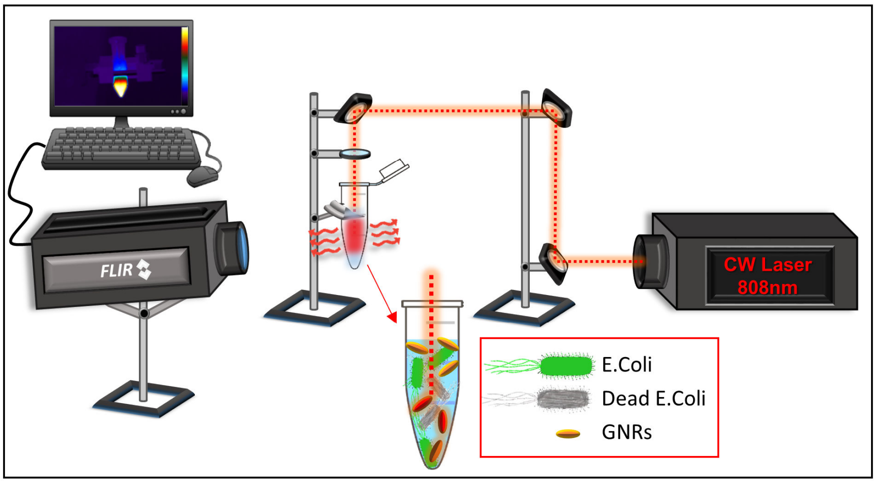

Figure 4.5 *– Schematic representation of the thermo-optical setup.*

The thermographic analysis has been carried out by using a FLIR (A655sc) together with its proprietary software (FLIR Research IR Max) that enables recording and processing of the thermal data acquired. Camera control parameters have been set such that sample emissivity is 0.89; camera-sample distance 50 cm and time resolution: 2.67 frame/sec.

Photothermal experiments have been performed to assess whether the GNRs concentration (C = 8.76 x 10^{-11}M) can induce thermo-plasmonic heating suited to affect the E.coli population. **Figure 4.6** shows the time-temperature profiles along with the corresponding thermographic pictures at 3 increasing illumination times (7.5, 15, and 30 minutes) for both E.coli and E.coli/GNRs samples. The temperature plots have been obtained by selecting, through the control software, an elliptical region of interest (ROI) which includes the illuminated area center.

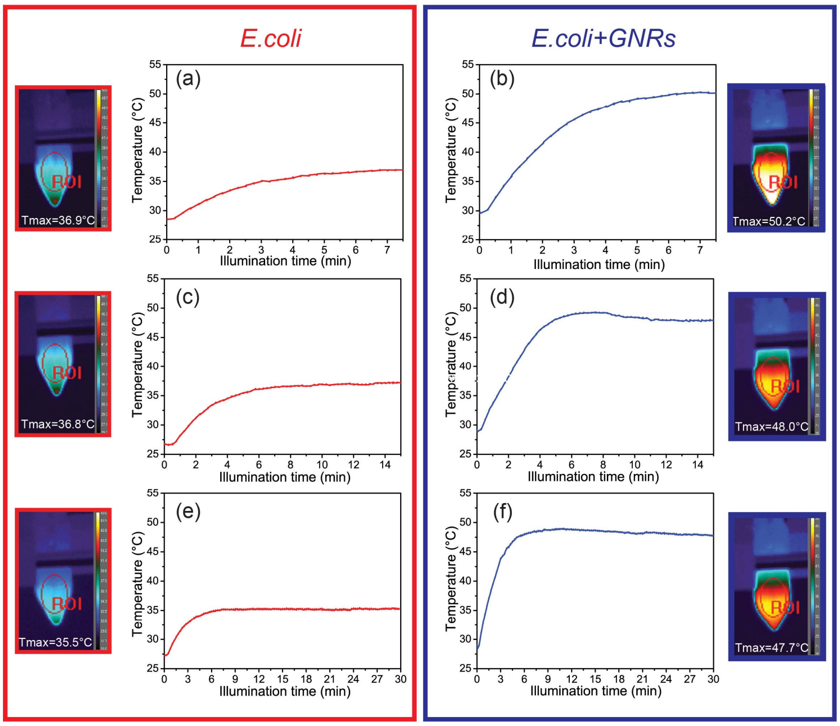

Figure 4.6 *– Temperature profiles of the E.coli (a), (c), (e), and E.coli/GNRs (b), (d), (f) samples for different illumination times along with the corresponding thermographic view of the sample in the Eppendorf tube.*

Figure 4.6 a, **c**, **e** show that upon illumination of the E.coli samples, the thermo-camera detects only a relatively low increment of temperature (up to 7-8 °C). Conversely, upon exposure of E.coli/GNRs, the absorbed light is efficiently converted into heat because of the PPT heating from the GNRs, and the thermo-camera detects a significant temperature increase, as shown in **Figure 4.6 b**, **d**, **f**. Indeed, after 7.5, 15, and 30 minutes of irradiation, a temperature increase from 20 °C to 50.2 °C, 48.0 °C, and 47.7 °C, respectively, has been detected, that corresponds essentially to the same temperature value, within the experimental variability. The relatively long exposure times (7.5, 15, 30 minutes) ensure a uniform distribution of the photo-induced heat (see thermal images reported in **Figure 4.6**). Importantly, all the temperature profiles reported in **Figure 4.6** show the same trend. After a rapid temperature increase in the first 5-7 minutes, a steady-state condition is observed.

E.coli viability test with and without GNRs, upon laser irradiation, have been performed at each scheduled time interval (7.5, 15, and 30 min). Namely, samples obtained upon serial dilutions from each tube have been cultured onto LB agar and incubated at 37 °C overnight. Afterward, the log N cells has been calculated through the plate count method. The viability results for both E.coli (red column) and E.coli/GNRs (blue column) samples (**Figure 4.7 a**) point out that the laser irradiation does not affect the viability of E.coli even after 30 minutes of continuous illumination (**Figure 4.7 b** (red curve).). Conversely, a significant increase of the killing efficiency (defined as the difference between the bacteria population at t = 0 min and t = 7. 5 min), of about 2 log CFU, is observed in presence of GNRs as shown in **Figure 4.7 b** (blue curve). It is worth pointing out that data reported in **Figure 4.7 a** have been normalized for every experiment to the bacterial population at each specific time interval to take into account the intrinsic cell proliferation.

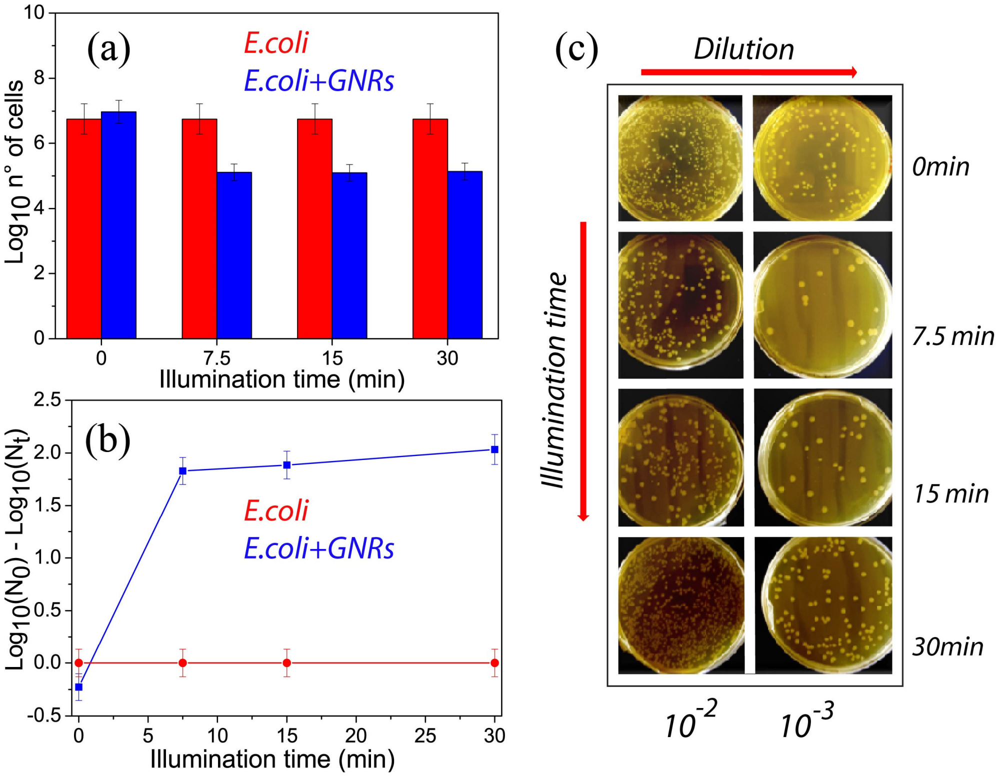

Figure 4.7 – (a) Results of the viability experiments and (b) plot of killing efficiency, carried out with (blue) and without (red) GNRs at different illumination times. (The reported data are an average of three independent experiments). (c) Pictures of the petri dishes containing the E.coli /GNRs colonies at increasing illumination times and different dilutions.

Moreover, it is important to point out that the protocol followed in the experiments for bacteria growth and counting has been highly standardized. Indeed, the bacteria population at different illumination times is confirmed to be essentially the same (**Figure 4.7 a**, red histogram plot), thus highlighting the capability to control the bacteria growth with high reproducibility. This, finally, turns in the same deviation, and hence in the same extent of the error bars for the results reported in **Figure 4.7 a**, and for those reported in **Figure 4.7 a**. To reliably count the E.coli colonies, the samples have been diluted with LB broth, and the pictures of the plates obtained from the exposed solutions as prepared and after dilution, in presence of GNRs, is reported in **Figure 4.7 c**. The plate count method has been successfully applied on the cultured diluted samples (**Figure 4.7 c**, right row), where well-distinguished colonies are present, while the high density colonies visible in the cultures of the less diluted samples (**Figure 4.7 c**, left row).

For sake of simplicity photos of the petri dishes containing the E.coli culture without the GNRs at different illumination times and dilution factors are compared with the culture with GNRs at t = 0 min.

It is important to point out that to clarify whether the light-driven thermo-plasmonic process explored so far is bacteriostatic or bactericidal, a more careful analysis of the experimental data reported in **Figure 4.7 a** is required.

It turns out that in presence of GNRs there is a reduction of about 2 log CFU of E.coli population (higher than 90% in terms of viability reduction) after 7.5 minutes of laser illumination. On the other hand, no further reduction in E. coli population is observed after 15 and 30 minutes of laser exposure, in presence of GNRs. This behavior can be explained by considering that after 15 minutes the bacterial cells have already implemented the molecular response mechanisms to environmental stress such as the PPT heating with possible DNA lesions and thus adapted to the new external conditions.[199] As a consequence, we can safely state that up to 7.5 minutes of laser irradiation the light assisted thermo-plasmonic heating results in a bactericidal effect, in agreement with the accepted definition of bactericidal property.[198, 200] After 7.5 minutes of laser illumination, the bacteria population remains constant (**Figure 4.7 b**, blue curve). This evidence suggests that the light-to-heat conversion due to the presence of highly efficient nano-converters (GNRs) ensures a bacteriostatic condition. Furthermore, in order to confirm a long term-effect of the bacteriostatic condition, we have performed a comparison between the bacteria population immediately and several hours after the end of the illumination process, being in the meanwhile the solution incubated at 37 °C (data not shown because are very similar to that reported in **Figure 4.7 a**). No change in the bacteria population has been measured.

Significantly, the outcome of the viability tests performed on the system that is photo-thermally heated at 50 °C (**Figure 4.7 b**) results in a much higher reduction of the bacteria viability than that found for the system heated up to the same temperature, but macroscopic (**Figure 4.4 c**, blue curve). Such a difference can be explained by considering that the photo-thermal heating due to the presence of the highly efficient nano-sources of heat represented by the GNRs, induces a localized temperature variations, while the thermal-camera is able to only detect the temperature variations at the glass/air interface of the Eppendorf tube. Moreover, the heat generation at the nanoscale is followed by other secondary mechanisms such as the formation of sound waves and generation of nano-bubbles which, in their turn, may contribute to the E.coli killing.

The remarkable achievement of a killing efficiency of 2 log CFU in a short time interval (7.5 min.) could be improved even more, by engineering the GNRs properties in terms of surface chemistry functionalization, aspect ratio, and concentration, thus possibly further increasing the temperature to value (e.g. 60 °C) sufficiently high to completely kill all the living bacteria, therefore representing a real breakthrough towards the realization of light assisted antimicrobial technologies based on the capability of GNRs to convert a NIR radiation into heat.

4.3 PPTT as an alternative to conventional cancer therapies

Cancer remains one of the leading causes of death [201]. Unfortunately, due to cancer's heterogeneous nature, there are currently no fully comprehensive approaches for treatment. One of the most promising solutions arises from the use of nanotechnologies for high precision applications in biomedicine.

Biomedical applications of plasmonic NPs such as AuNPs and AgNPs have steadily grown in the past 10 years. In particular, the ability of NPs to convert light into thermal energy (photo-thermal effect) has been exploited to develop a non-invasive, drug-free therapy defined plasmonic photo-thermal therapy (PPTT)[8, 42-43, 88-89, 202] as already explained at the beginning of this chapter.

NPs-mediated PPTT has also been thoroughly investigated for tumor ablation in animal models, reaching in some cases the clinical trial stage.[203-205] This strategy allows the precise localization and controlled heating in the area surrounding the tumor [68, 87], producing irreversible cell damage mediated by membrane disruption as well as proteins and/or DNA denaturation.[206]

In this framework, PPTT has paved the way for an undoubtedly efficient and unique approach for cancer-related diseases treatment, with innumerable advantages over conventional therapeutic methods, such as chemotherapy, radiotherapy, immunotherapy, and surgery. The advantages mainly concern the spatiotemporal selectivity, high sensitivity, side effect mitigation, non-invasiveness, speed of treatment, and relatively low cost.[68]

The ideal NP formulations for PPT applications have to provide exceptional optical properties (i.e., excellent photo-thermal conversion efficiency and long-lasting photo-stabilities), colloidal stability, biocompatibility, and a preferential uptake pathway with carcinogenic cells.[68] From this standpoint, AuNPs are suitable candidates for PPT applications because of their chemical/biological stability, small size, strong and tunable LSPR frequency, high level of biocompatibility, and easy surface functionalization and modification.[94, 184]

As already mentioned before, commercially available AuNPs are typically stabilized with CTAB, which exhibits a very high intrinsic toxicity towards cells. Intrinsic CTAB cytotoxicity can be reduced by utilizing a centrifugation process of AuNPs dispersions, which removes the excess of non-conjugated CTAB[207], a methodology similar to that used in the work shown in the previous paragraph. Another commonly used protocol to reduce the CTAB toxicity is replacing the CTAB layer with poly (ethylene glycol) (PEG).[202, 208-210] Unfortunately, pegylated NPs exhibit reduced cellular uptake [211] along with the intrinsic toxicity related to the residual CTAB.

The most promising alternatives derive from hybrid and synergistic combinations of inorganic NPs (like AuNPs) coated with biomolecules, as shown in detail in the next section.

4.3.1 Biomimetic Keratin AuNPs-mediated in Vitro PPTT on Glioblastoma Multiforme

Biomaterials, and proteins, in particular, are excellent candidates for realizing a new generation of functionalized NPs with improved biocompatibility, biodistribution, stability, and half-life.[212]

AuNPs capped with endogenous proteins such as bovine serum albumin (BSA) and human serum albumin (HSA) showed both surface shielding and functional ligand incorporation.[212-216] To the best of our knowledge, among the different proteins used to functionalize the surface of AuNPs, keratin is still unexplored, and no studies reporting its utilization in the field of PPT-based applications have been found. Keratins are a family of proteins found in several animal tissues such as hair, hooves, skin, and claws, providing mechanical reinforcement to tissues. There are several different types of keratins, which all share extensive hydrogen bonds and a high amount of cysteine and disulfide bridges.[217] Keratin has an intrinsic biological activity and biocompatibility,[218] and has been studied as a biomaterial platform with applications ranging from wound healing [219-220] to drug delivery.[217, 221-225] Water solutions of keratin proteins can be easily obtained and processed in the final material or device in mild conditions. These features are enticing for the use of keratin as a stabilizer (or capping agent) for NPs, coupling the intrinsic biocompatibility of Au and its value as nanotherapeutic with the interesting properties of keratin. A few studies have reported the utilization of keratin as a capping agent for AgNPs, primarily utilized as antimicrobial agents.[226-228] Here, we report the synthesis, application, and characterization of a new generation of keratin coated AuNPs (Ker-AuNPs) as a highly efficient photosensitive platform for PPT applications. The biomimetic properties of Ker-AuNPs derive from the combination of inorganic AuNPs (synthetic nanomaterials) and a biocompatible coating made of a keratin layer (natural material).[229] This powerful combination entails the benefits of two worlds: i) AuNPs are excellent nano-sources of heat; ii) keratin provides a protein-based interface for the AuNP to interact with the biological environment, similar to the naturally occurring protein corona effect.[230-231]

We validate the exceptional biocompatibility of Ker-AuNPs and perform PPT experiments on a human cell line (U87-MG) derived from glioblastoma, a brain tumor of glial origin, one of the most aggressive and currently untreatable cancer.[232-233] Despite the best of the cares, which are represented by accurate surgical resection, radio- and chemotherapy, the median survival is about 14.6 months [232]. This is mainly due to the high capacity of glioblastoma cells to migrate and invade the near parenchyma, to resist conventional therapies, as well as to the low drug delivery efficiency [233]. In light of these considerations, it becomes of fundamental importance to find novel strategies to improve the treatments of this devastating tumor.

Keratin-AuNPs and U87-MG cells sample preparation

According to a previously reported protocol, the water solution of keratin was obtained from wool fibers.[234] Olimpia s.r.l kindly donated Argentinian sheep wool (Ponzano Veneto, TV, Italy). Briefly, wool fibers were cleaned using a 1:1 methanol/acetone solution under agitation overnight and rinsed twice with clean solvents then twice with Milli-Q distilled water. Cleaned fibers were dried overnight at room temperature. Keratin was extracted from wool fibers with a water solution containing 7M urea, 0.05 M sodium dodecyl sulfate (SDS), and 1.1 M 2-mercaptoethanol. The extraction was performed with 10 grams of wool in 180 ml of solution at 60 °C for 5h. Afterward, the solution was filtered with a 50-mesh stainless steel grid and dialyzed against Milli-Q distilled water for three days with seven water changes. The resulting solution was centrifuged to remove undissolved fiber residues. The protein concentration was measured by drying a known volume of the solution and weighing the dried residue. When necessary, the solution was concentrated by partial water evaporation.

AuNPs were synthesized according to the Turkevich method,[165] using sodium citrate as a reducing agent. To produce the Ker-AuNPs, AuNPs solution, 1.5 mM Au, was mixed with the keratin solution in order to have a 1:100 weight ratio between Au and keratin. In carrying out keratin's bioconjugation on AuNPs, an amount of keratin three orders of magnitude higher than what was expected to be conjugated was used. This large excess of keratin was used to ensure that all the AuNPs binding sites were saturated. Similarly, a water solution of CTAB was added to the AuNPs to allow CTAB to bind to the AuNPs. The synthesis protocols for Ker-AuNPs and CTAB-AuNPs were performed with the same w/w ratio to have a similar functionalization. The solutions were gently shaken overnight, then AuNPs were centrifuged twice at 14300 g and resuspended in MilliQ water to remove unbound keratin or CTAB. To produce the fluorescent Ker-AuNPs (Ker*-AuNPs), keratin was first labeled by using the FluoReporter FITC Protein Labeling Kit (ThermoFisher, Waltham, MA) following the manufacturer's instructions. In particular, a buffer solution of $NaHCO_3$ 1 M, pH 9, was prepared. 1955 µL of buffer and 45 µL of keratin solution 44 mg/mL were mixed to obtain 2 mL of solution with a final keratin concentration of 1 mg/mL. FITC powder was dissolved in 10 µL of DMSO. The solubilized FITC was added to the buffered keratin solution and mixed under stirrer for 1 hour in dark condition at room temperature. The keratin-FITC solution was dialyzed in a dialysis cassette with a molecular weight cut off (MWCO) of 3500 kDa for three days against MilliQ water. Ker*-AuNPs were synthesized using the same protocol used for Ker-AuNPs.

The synthesis of Ker-AuNPs is easy and fast, and no limitations for large scale production are foreseen. Having all the processing done in water and in mild conditions, makes it easy to combine keratin with AuNPs and preserve the inherent biocompatibility of keratin. Moreover, the synthesis protocol used takes already into account a sustainable approach by using a reduced number of components, all non-toxic and non-hazardous.

U87-MG glioblastoma multiforme cell line was purchased from CLS (Cell Lines Service GmbH, Eppelheim, Germany). It was grown in Dulbecco's Modified Eagle Medium (DMEM) supplemented with 10% heat-inactivated Fetal Bovine Serum (FBS, Sigma–Aldrich St. Louis, MO), 100 IU/ml penicillin G, 100 µg/ml streptomycin, 1% L-glutamine, 1% nonessential amino acids, and 1mM sodium pyruvate at 37°C in a 5% CO_2-

humidified atmosphere. The medium was changed twice weekly, and the cells were subcultured only when confluent. In general, for all the experiments, U87-MG cells ($5x10^5$) were incubated in suspension in 15ml polypropylene tubes with 50µM Ker-AuNPs at 37°C in a 5% CO_2-humidified atmosphere for 24h. Then, cells were washed in PBS, and resuspended in PBS, 2% FBS and irradiated (details on the photo-thermal experiments are reported below). After irradiation, cells were centrifuged at 250xg for 5 min, resuspended in DMEM medium supplemented with 10% FBS, and grown at 37°C in a 5% CO_2-humidified atmosphere. All the biological and technical details relating to the U87-MG/Ker-AuNPs sample preparation, for the various analyses carried out (MTS assay, Immunofluorescence staining, TEM imaging, Cytometric analyses, Trypan blue exclusion assay, Dynamic light scattering and ζ-potential, UV-Vis, and Infrared spectroscopy, X-ray Photoelectron Spectroscopy (XPS), are reported in the Materials and Methods of our article 7, present in the list of publications.

Optical and morphological properties of AuNPs

Optical, spectroscopic, and morphological analysis of both as-synthesized and keratin-coated AuNPs was performed to characterize the keratin's binding to the AuNPs and its effect on optical and structural properties. **Figure 4.8 A** shows the absorption spectra of the spherical AuNPs (blue curve) and Ker-AuNPs (red curve) dispersed in water. A red-shift of the LSPR frequency from 522 nm to 527 nm is observed because of the change of the local refractive index surrounding the AuNPs.

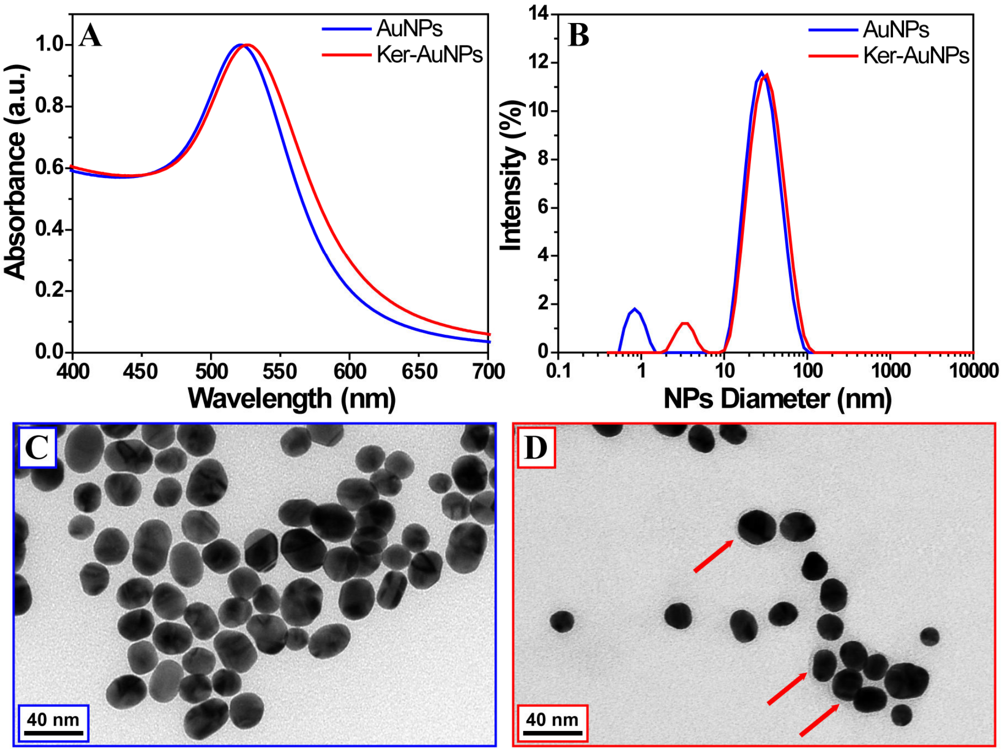

Figure 4.8 *– UV-Vis absorption spectra of AuNPs (A, blue curve) and Ker-AuNPs (A, red curve), along with their corresponding DLS measurements (B, blue curve), (B, red curve). TEM images of AuNPs (C) and Ker-AuNPs (D).*

A simplified simulation using the Mie theory for LSPR (**Figure 4.9**) shows that a 5 nm red shift is compatible with an increase of the local refractive index of 0.07 refractive index units. **Figure 4.8 B** shows the DLS measurements, evidencing a variation of the hydrodynamic diameter from 28.2 nm (AuNPs, blue curve) to 32.7 nm (Ker-AuNPs, red curve), thus confirming the presence of a thicker (keratin) layer surrounding the AuNPs. TEM characterization performed on both AuNPs (**Figure 4.8 C**) and Ker-AuNPs (**Figure 4.8 D**) solutions, besides highlighting the spherical geometry and a moderate size-distribution of both NP populations, confirms the presence of a halo around the AuNPs after the functionalization with keratin (**Figure 4.8 D**).

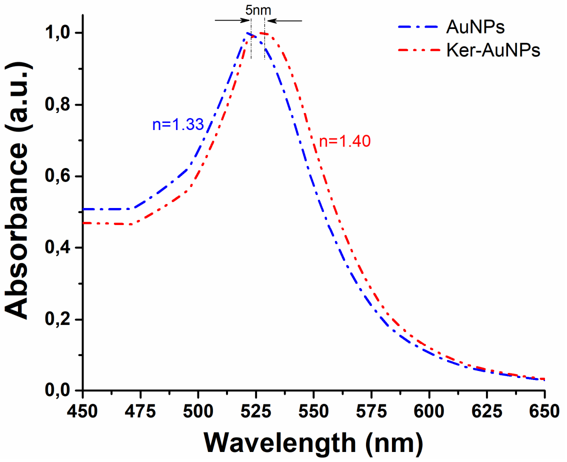

Figure 4.9 *– Theoretical absorption spectra of the AuNPs (blue) and Ker-AuNPs (red). We have assumed water (n=1.3) as a medium surrounding the AuNPs.*

The absorption spectra of Ker-AuNPs dispersed in PBS and in the presence of cells (U87-MG) are reported in (**Figure 4.10 A**). The spectral curves are unchanged. Only a small spectral shift (3 nm) is present, proving the stability of the AuNPs and showing the stability/response of Ker-AuNPs to the change of the surrounding medium produced by the presence of U87-MG cells. Besides, absorption spectra at different temperatures (**Figure 4.10 B**) were acquired, evidencing a perfect spectral overlap after all the heating experiments, thus demonstrating the thermal stability of Ker-AuNPs.

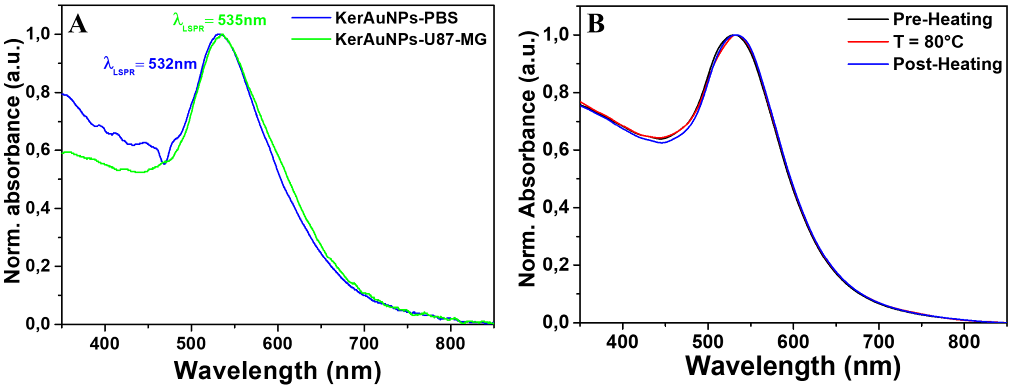

Figure 4.10 *– UV-Vis absorption spectra of Ker-AuNPs in different media (A), at different temperature steps (B).*

To further highlight the improved stability provided by keratin, plain AuNPs, CTAB-AuNPs, and Ker-AuNPs were dispersed in a physiological water solution (100 mM PBS at pH 7.4) (**Figure 4.11**). The plain AuNPs and CTAB-AuNPs showed a drastic color change due to AuNPs aggregation. In contrast, the Ker-AuNPs maintained their original ruby red color thanks to the keratin layer's extraordinary stability present on the AuNPs surface.

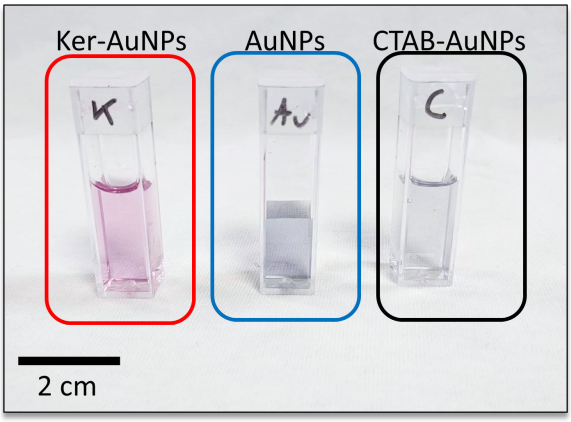

Figure 4.11 *– AuNPs with different coatings dispersed in a PBS water solution: Ker-AuNPs, plain AuNPs, CTAB-AuNPs. The blue-gray color of plain AuNPs and CTAB-AuNPs is associated with aggregation of the NPs, while Ker-AuNPs' solution maintained the original color, confirming the excellent stability offered by the keratin coating.*

FTIR analysis in **Figure 4.12** evidences the presence of keratin proteins attached to the AuNPs.

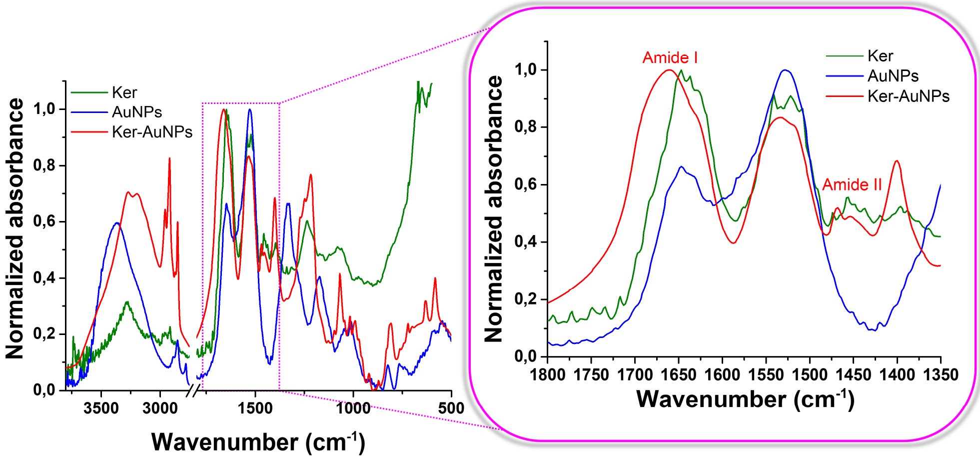

Figure 4.12 *– FTIR spectra of Ker (green), AuNPs (blue), and Ker-AuNPs (red). Amide I and Amide II bands of proteins in the highlighted graph.*

The peaks at 1600 cm^{-1} and 1450 cm^{-1} are the Amide I and Amide II bands of proteins. The deconvolution of the amide I absorption band, using a previously reported procedure,[235-236] shows that when comparing keratin self-assembly on AuNPs and freestanding films, Ker-AuNPs showed a higher % of alpha-helices (15% on Ker-AuNP vs. 6% on keratin films) and a lower amount of compact beta sheets (23 % on Ker-AuNP vs. 35% on Keratin films). This different self-assembly reflects a more loosely organized structure of keratin on the AuNPs than, freestanding films, probably due to the presence of Cys-Au bonds that prevent more compact self-assembly.

The successful conjugation between the keratin molecules and the AuNPs surface influences the ζ-potential of the AuNPs. Indeed, AuNPs dispersed in water exhibit a ζ-potential of (-42 ± 4) mV, whereas for the Ker-AuNPs (-18 ± 2) mV, confirming the change of the chemical environment surrounding the AuNPs. The zeta potential of CTAB-AuNPs is (+33.6 ± 2 mV). Similarly, also XPS analysis supports the presence of keratin proteins in the Ker-AuNPs sample.

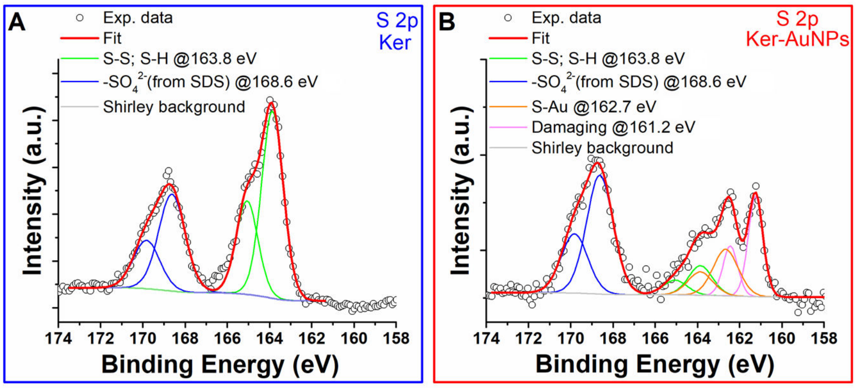

Figure 4.13 *– XPS spectra. S 2p signal of Ker (A) and Ker-AuNPs (B).*

Indeed, the sample shows the presence of nitrogen and sulfur signals[237] typical of the peptide bonds and disulfide bonds of keratin, that are not present in the AuNPs sample. A closer look at the S 2p signal **Figure 4.13** suggests that the interaction between AuNPs and keratin is mediated by the sulfurs, as the Ker-AuNPs show signals that could be assigned to the formation of S-Au bonds.[238]

Photo-thermal properties of Ker-AuNPs

Light-triggered photo-thermal experiments were carried out using the thermo-optical setup sketched in **Figure 4.14**.

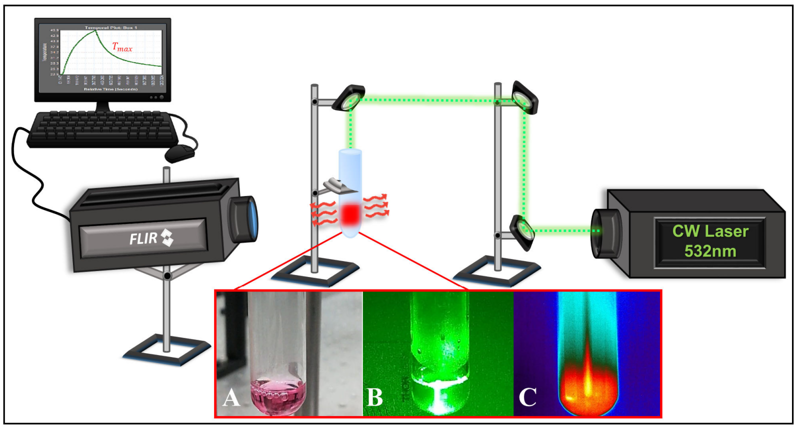

Figure 4.14 *– Schematic representation of the thermo-optical setup used for sample characterization. M1, M2, M3 are the mirrors. The inset shows a glass tube containing the U87-MG+Ker*-AuNPs sample used to conduct the photo-thermal experiments, before irradiation A, during irradiation B, along with the corresponding thermographic view C.*

It makes use of a resonant CW green laser (gem532, Laser Quantum), operating at 532 nm in the high absorption band of Ker-AuNPs. The laser beam was directed perpendicularly (from the top) to the air/solution interface, using three mirrors, in the central part of a glass tube.

A high-resolution thermal-camera was used to map and identify (side view) both the spatial heating distribution and the temperature profile under top-pumping laser illumination. The dynamic IR thermographic analysis was carried out using a FLIR (A655sc) thermal-camera (FLIR System, Wilsonville, OR, USA), suitably equipped with a close-up IR lens characterized by a magnifying factor of 2.9x, a spatial resolution (IFOV) of 50 μm and a reduced working distance. To measure the maximum and mean temperature values reached in the whole sample volume, a circular region (1.76 cm^2) of interest (ROI), encompassing the irradiated volume, was selected on thermographic images. The camera works seamlessly with proprietary software (FLIR Research IR Max, FLIR System, Wilsonville, OR, USA) that enables recording and processing the camera's thermal data. Camera control parameters were set, such that sample emissivity was 0.89 (glass tube) and camera-sample working distance 12 cm. Data collection and analysis were based on the careful evaluation of representative IR image sequences acquired during the laser irradiation.

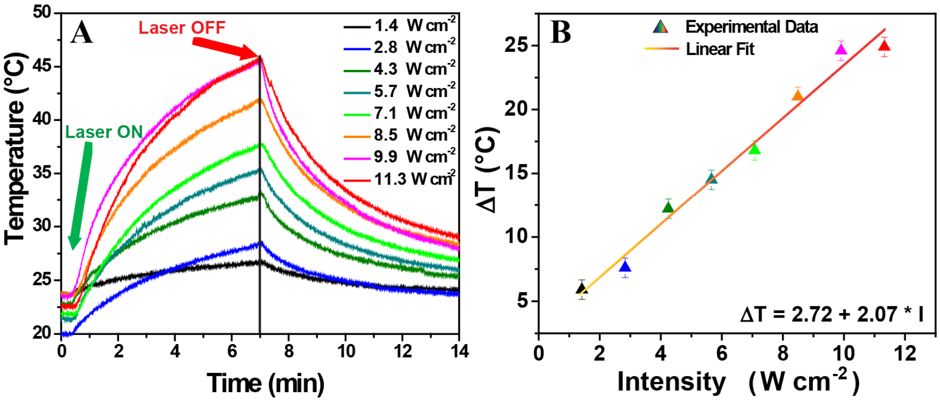

Figure 4.15 *– (A) Time-temperature dependence of Ker-AuNPs dispersed in water under pump beam illumination along with the linear fit of the temperature variation versus the intensity of the pump beam (B). The goodness of the fit is highlighted by the coefficient of determination* $R^2=0.98$.

Ker-AuNPs dispersed in water ($2.25 \cdot 10^{-3}$ M in Au) were exposed at different intensity values of the pump beam (from 1.4 W/cm^2 to 11.3 W/cm^2) for 7 min. **Figure 4.15 A** shows that upon illumination (laser ON) there is a gradual and significant temperature increase up to 45 °C because of the PPT heating of Ker-AuNPs. The sample starts to cool back down to room temperature as soon as the pump beam is switched off (laser OFF). The temperature profiles reported in **Figure 4.15 A** were obtained by processing the corresponding thermal images as previously detailed. **Figure 4.15 B** evidences a linear correlation between the temperature variation ($\Delta T = T - T_0$, where T_0 is the initial sample temperature when the pump beam is OFF) and the intensity of the pump beam, confirming the expected behavior according to theoretical predictions (2.25, paragraph 2.2). Control experiments realized with a water solution of keratin did not show any significant temperature increase (data not shown), supporting that the observed temperature increase (**Figure 4.15 A**) can be attributed to the photo-thermal properties of AuNPs.

It is worth pointing out that the light-heat conversion property of the Ker-AuNPs is retained even after performing several illumination cycles (8) as shown in **Figure 4.15 A**, hence underlining the excellent photo-thermal stability of Ker-AuNPs, which is a mandatory requirement for thermal dosimetry and treatment planning in PPT-based applications.

3D photo-thermal characterization

Further photo-thermal characterization was carried out to investigate the uniformity of temperature distribution and the laser beam's penetration depth, focusing the analysis on a 3D ROI correspondent to an ideal 1cm^2 cube of U87 cells + Ker-AuNPs. To conduct a 3D analysis of the sample, the optical setup was slightly modified (**Figure 4.16**) to direct the laser beam in the middle of the cube, entering in one side of the quartz cuvette, while the thermal-camera was recording the temperature variation in a 45° configuration, analyzing in total three sides (side1, side2, side3) of the cuvette in two different configurations, for simplicity, only the first configuration is shown with the thermal imaging camera positioned at 45 ° with respect to side 1 and side 2 of the cuvette (**Figure 4.16**).

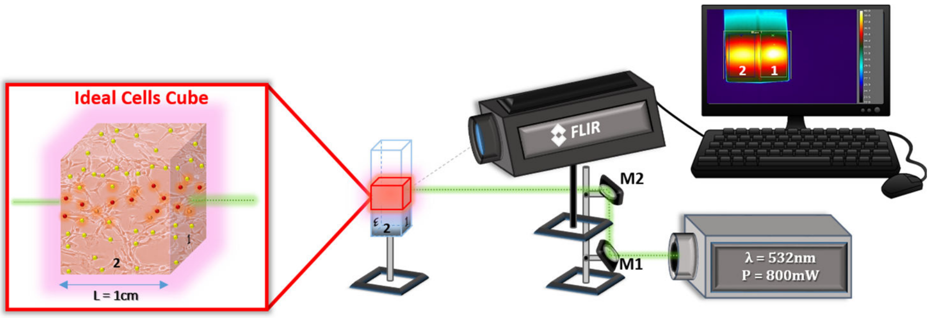

Figure 4.16 *–Thermo-optical setup used for the 3D sample characterization.*

This ideal "cube of cells" was irradiated with a 0.8 W laser beam for 10 minutes, and the corresponding temperature variation was monitored through the IR thermal camera. Plots reported in **Figure 4.17**, show thermal data from a box profile, with thermographs extracted using the FLIR software at a time interval of 60 s.

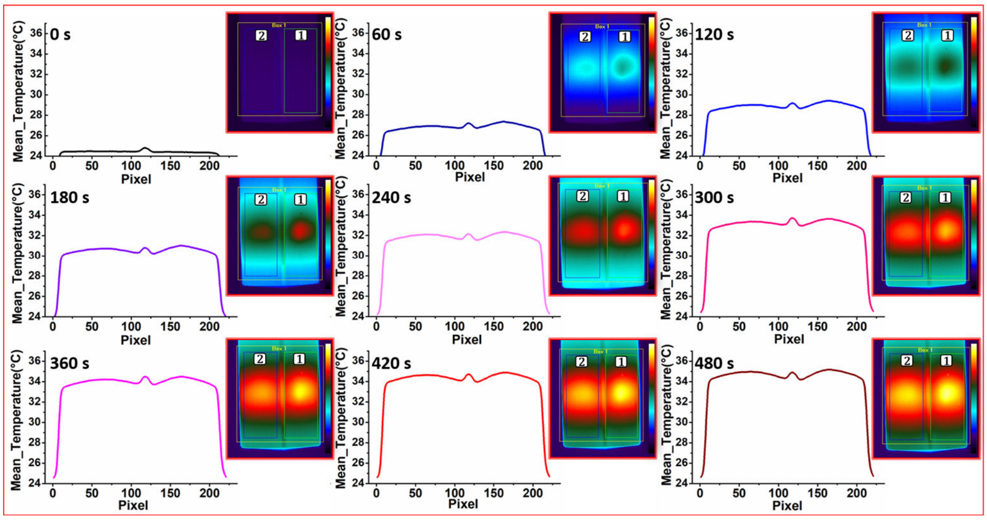

Figure 4.17 *– (A) Mean temperature profiles as a function of the pixels showing the uniformity of the mean temperature inside the cube, at temporal intervals of 60s. (B) Along with the corresponding thermographic view of the sample in the quartz cuvette.*

Looking at the thermal profiles, along with the corresponding thermographic view of the sample in the quartz cuvette (**Figure 4.17**), it is possible to see that after irradiation of about 7min (P=0.8W) the temperature distribution appears to be uniform within the whole ideal 1cm^2 cube of cells (the two humps of the curve have reached the same height). The thermographic images extracted from the 45 ° analysis provide an immediate qualitative analysis of what happens in terms of macroscopic temperature increment. In particular, the thermographs in **Figure 4.17** show the temperature distribution in the sample at different times. It clearly can be observed that not only the incident laser area (side 1) has been heated, but also there is a radial propagation by diffusion of the generated heat; thus, there is energy transmitted to the adjacent regions due to the immersed NPs. Moreover, it can be seen that the temperature increment follows a rapid dynamic in the first seconds immediately after turning ON the laser and gradually slows down to reach a stationary condition and a uniform temperature distribution throughout the cube analyzed in 7-8 min.

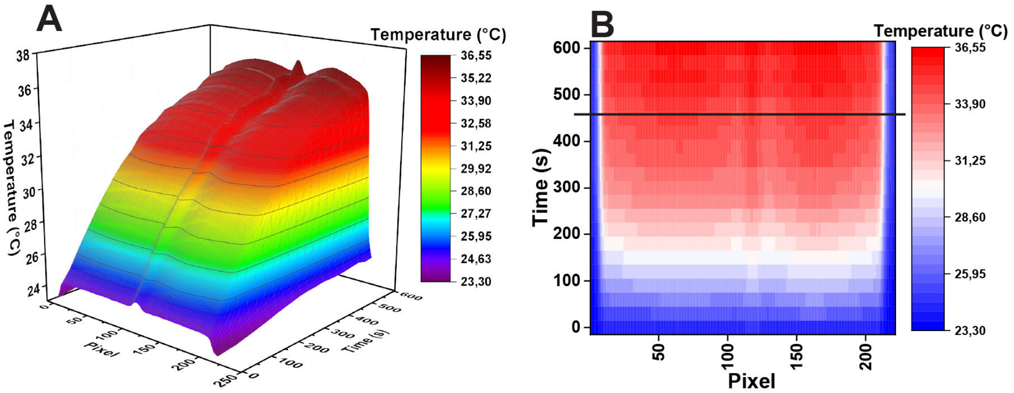

Figure 4.18 *– (A) 3D temperature distribution and (B) heat map of Ker-AuNPs/U87 cells sample.*

Also, from the 3D spatial thermographic profile and the heat distribution map (**Figure 4.18**), a uniform distribution of heat within the sample is evident. Looking at the heat map **Figure 4.18 B**, two other aspects can be deduced: i) the heat is confined within the analyzed volume, ii) the heat is not generated by heating the surrounding container and transferred to the medium but is generated internally by the excitation of the NPs; iii) all the NPs in the volume absorb radiation and re-emit energy in the form of heat and equally participate in the heating generation, resulting in a macroscopic temperature rise of about 15°C. This temperature increment, generated in this Ker-AuNPs/U87 ideal cube, used as a biological environment simple model, satisfies the biomedical requirement for treating superficial diseases (mycoses, fungal infections, and many different types of skin cancer). [239]

Biocompatibility of Ker-AuNPs

To evaluate the biocompatibility of Ker-AuNPs, a dose-response assay on human glioblastoma cell line U87-MG was performed. Experiments were performed by utilizing AuNPs, CTAB-AuNPs, and Ker-AuNPs. **Figure 4.19** summarizes the viability results of U87-MG cells incubated with different concentrations (0-50 μM) of AuNPs (green curves), CTAB-AuNPs (red curves), and Ker-AuNPs (blue curves) at different incubation times (A, 24h; B, 48h; C, 72 h). As expected, the capping agent plays a decisive effect on cell viability. Indeed, CTAB-AuNPs were found to be very toxic to cells, causing a reduction in cell viability depending on both concentration and incubation time. In particular, incubation with CTAB-AuNPs at the highest concentration of 50 μM for 72h reduced U87-MG cell viability down to 20%. Conversely, both Ker-AuNPs and AuNPs were completely biocompatible, exhibiting viability of about 100% for concentrations up to 50 μM.

It is noteworthy that AuNPs, despite their good biocompatibility, are difficult to use in real applications because of the weak stabilizing effect of citrate molecules that is replaced by proteins and other biomolecules as soon as the NPs enter the biological environment.[240] Indeed, plain AuNPs in solution are stabilized by electrostatic repulsion, making them stable only at deficient concentrations. In the viability experiments (**Figure 4.19**), larger volumes of plain AuNPs solution were utilized to achieve the same quantities used for Ker-AuNPs (50μM). Besides, plain AuNPs require a coating to allow their functionalization with fluorescent molecules and are therefore not suitable for detection with fluorescence microscopy and flow cytometry. Conversely, the keratin coating provides improved stability at the higher concentration, a mandatory requirement for performing PPT experiments at physiological pH and salt concentration used for in vitro studies. Moreover, the keratin layer's presence easily allows the post-functionalization process with other molecules (e.g. fluorescent FITC tag). Ker-AuNPs, on the other hand, possess a very similar biocompatibility profile of AuNPs (see **Figure 4.19**C) with a protein coating that provides improved stability in the biological environment, significantly improving their utilization as nanotherapeutic agents.

Because no significant reduction in cell viability was observed using the maximum concentration of 50 μM of Ker-AuNPs, this value was utilized for all the experiments reported below. The utilized concentration value allows from one side, maximizing the photo-thermal properties while from the other side minimizing the utilized amount of the Ker-AuNPs solution, a condition highly required in PPT-based treatment planning.[86]

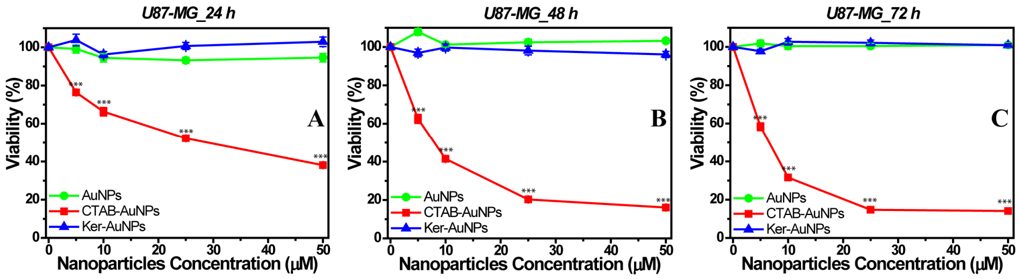

*Figure 4.19 – Effects of AuNPs (green curves), CTAB-AuNPs (red curves), and Ker-AuNPs (blue curves) on the viability of U87-MG cells. MTS assay shows the viability (expressed as percentage vs control) of U87-MG cells incubated with increasing concentrations (0-50 µM) for 24h (A), 48h (B), and 72h (C). (***: $p<0.001$).*

Interaction between Ker-AuNP and U87-MG cells*

U87-MG cells co-stained with Phalloidin-Texas Red and DAPI were incubated with and without FITC-labelled Ker-AuNPs (Ker*-AuNPs) for 24h. **Figure 4.20** shows the fluorescence microscope images of U87-MG cells without (top images) and with (bottom images) the presence of Ker*-AuNPs. It is worth noting that the Ker*-AuNPs green signal colocalizes with both Phalloidin-Texas Red and DAPI signals suggesting that Ker*-AuNPs physically interact with U87-MG cells.

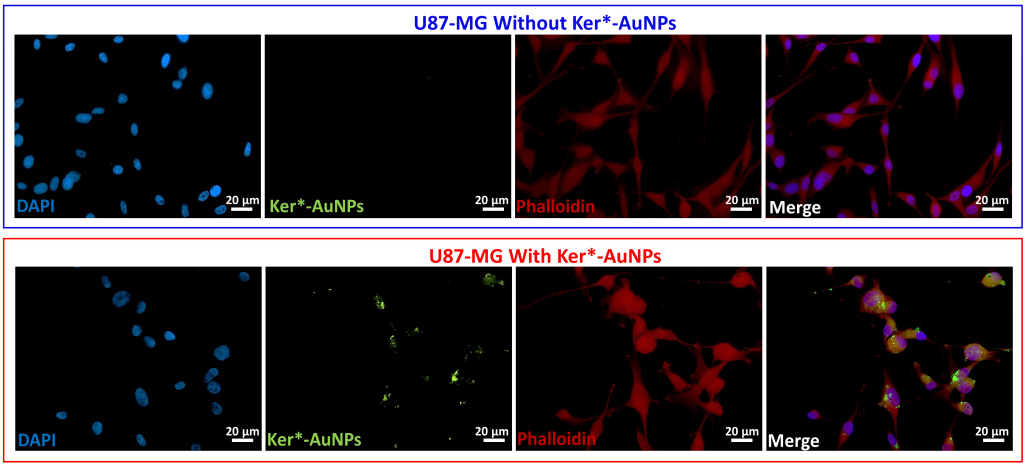

Figure 4.20 – Immunofluorescence staining of U87-MG cells alone and incubated with Ker-AuNPs. Photographs show nucleus (DAPI, blue), Ker*-AuNPs (green), the cytoskeleton (Phalloidin, red), and the merged channels (Merge) in control cells (without Ker*-AuNPs, upper images) and Ker*-AuNPs -treated cells (lower images).*

Moreover, to quantitatively understand the dynamics of U87-MG cells + Ker*-AuNPs interaction, a cytofluorimetric analysis of U87-MG cells was incubated with 50 µM Ker*-AuNPs for 0, 2, 4, 6, 24, and 48h was performed. During the first 6 hours, the percentage of U87-MG cells loaded with Ker*-AuNPs (shortly defined positivity) is about 3.5% (**Figure 4.21 B**, **C**, **D**). Interestingly, as shown in **Figure 4.21 E**, **G**, after 24h of incubation, the positivity raises to ≊ 23%, reaching a positivity of about 68% after 48h, whereas no significant variation was observed at longer incubation times.

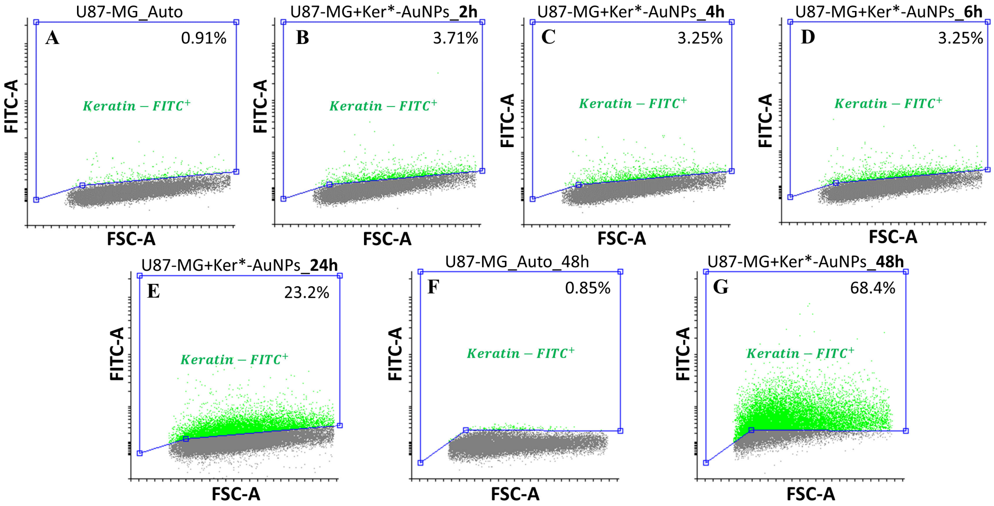

Figure 4.21 *– Cytofluorimetric analysis showing U87-MG cells positivity (expressed as percentage of Keratin-FITC$^+$ cells) to Ker*-AuNPs after 2h (B), 4h(C), 6h(D), 24h (E) and 48h (G) of incubation time along with their respective controls (A, F).*

The kinetics of Ker-AuNPs cellular uptake rate was fitted using a logistic model by utilizing the following equation:

$$FITC^{+}cells = \alpha\left[1-\frac{1}{1+\left(\frac{t}{t_0}\right)^{\beta}}\right] \tag{4.1}$$

Where $\alpha = 100$ is the threshold value, $t_0 = 36.5h$ is the time value at which the uptake is at 50%, and $\beta = 2.8$ represents the growth rate of the uptake curve. The fit goodness is estimated from the Coefficient of determination $R^2 = 0.989$.

The logistic model is commonly used to describe the self-limiting growth of a biological population. The graph of this model used to fit the experimental data, yields a Sigmoidal-shaped curve (**Figure 4.22**). It is a more realistic model for cellular uptake kinetics than exponential growth since exponential growth is possible only when infinite Ker-AuNPs are available. There are three different sections to an S-shaped curve. Initially, growth is exponential because there are ample resources available (Ker-AuNPs). Then, as resources begin to become limited at the saturation point, the cellular uptake rate decreases. Finally, uptake reaches a plateau at the maximum threshold of the environment, with little change in cellular uptake over time.

These results evidence that the cellular uptake dynamic process is a time-dependent phenomenon governed by several parameters such as NPs size/geometry, cell types, and enhanced permeability and retention (EPR) effect.[54, 241-242]

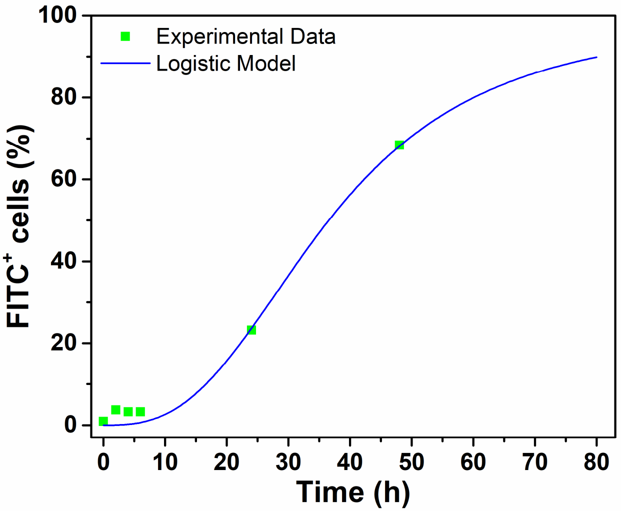

Figure 4.22 *– Cytofluorimetric experimental data for U87-MG cells positivity (expressed as percentage of Keratin-FITC + cells) to Ker*-AuNPs after 2h, 4h, 6h, 24h, and 48h of incubation time fitted using a logistic model.*

Ultrastructural analysis of Ker-AuNPs uptake*

Cellular uptake of Ker*-AuNPs and ultrastructural changes were examined by high-resolution TEM analysis. Results reported in **Figure 4.23** confirm the internalization of the Ker*-AuNPs into U87-MG cells. U87-MG cells (**Figure 4.23**) exhibit an irregular and great morphological variability, cell surface area, and membrane folding exhibited various types of protrusions, including blebs and filopodia. **Figure 4.23 A**, **B** evidence the plasma membrane projections surrounding (**A**) and engulfing (**B**) several Ker*-AuNPs before internalization into the cytoplasm. There is evidence of Ker*-AuNPs on the apical surface along with well-packed Ker*-AuNPs internalized in endocytic vesicles with different electron density (**C**, **D**). Cell structures like nucleus, mitochondria, Golgi apparatus, and rough endoplasmic reticulum (R.E.R) were visible, oval or rod-shaped mitochondria with a medium or high electron density matrix were detected (**A**, **D**).

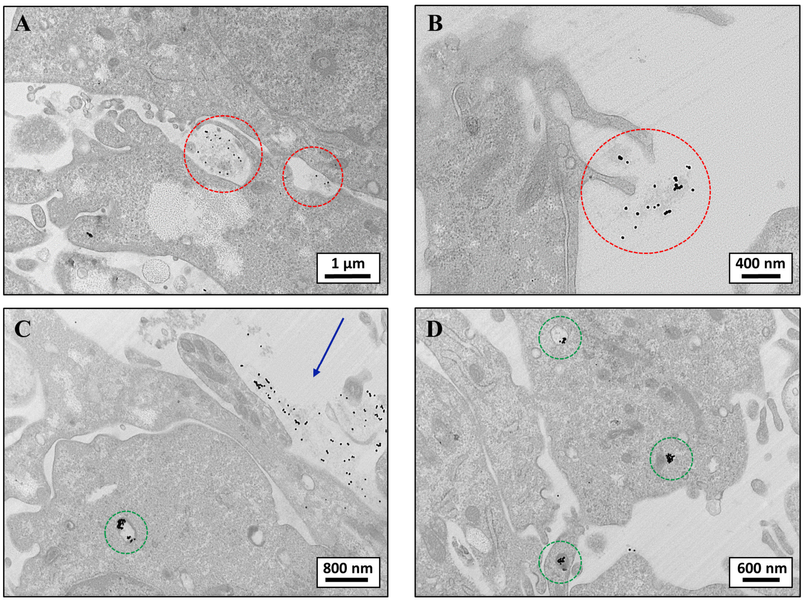

Figure 4.23 *– Ultrastructural localization of Ker*-AuNPs in U87-MG cells. (A, B) Electron dense Ker*-AuNPs were present on the cell surfaces where the plasma membrane projections internalize several Ker*-AuNPs (dotted red circles). (C, D) Ker*-AuNPs were found outside the cell along the plasma membrane (blue arrow) as well as internalized inside small dense vesicles (endosomes) (dotted green circles).*

The detailed analysis carried out by a TEM analysis revealed the Ker*-AuNPs cells' internalization mechanism, which turned out to be an endocytosis-based uptake pathway.

PPT experiments on U87-MG cells incubated with Ker-AuNPs*

Photo-thermal experiments, performed by utilizing the thermo-optical setup sketched in **Figure 4.14**, were devoted to study the effect of the laser illumination on the viability of the U87-MG cells. Experiments were realized by top-illuminating both U87-MG cells (control sample) and U87-MG cells incubated with Ker*-AuNPs, for 10 min at 11.3 W/cm^2. Illumination time and intensity values were selected to optimize both photo-thermal properties and cell viability reduction. While the illumination of U87-MG cells resulted in a negligible increment of temperature to less than 2°C (**Figure 4.24 A**, **B** blue curve), U87-MG cells incubated with Ker*-AuNPs once illuminated showed a moderate temperature increase of about 7.5 °C (**Figure 4.24 C**, **B** red curve) caused by the PPT effect.

The effect of the laser irradiation on cell viability was studied by biparametric cytofluorimetric analysis. This technique aims at detecting the percentage of dead U87-MG cells (incorporating the fluorescent DNA intercalant propidium iodide, PI$^+$ cells) and cells loaded with Ker*-AuNPs (FITC$^+$ cells). U87-MG cells irradiated without Ker*-AuNPs (**Figure 4.24 D**) showed 23.83% (0.68%+23.15%) of PI$^+$ cells, compared to 40.29% (14.16% +26.13%) of PI$^+$ cells in the presence of Ker*-AuNPs (**Figure 4.24 E**). These results confirm that cell viability is minimally affected by laser illumination alone and that the presence of Ker*-AuNPs increases the mortality because of the induced local heating. Noteworthy, among the total percentage of dead cells in the presence of Ker*-AuNPs (**Figure 4.24 E**), 26.13% are both PI$^+$ and FITC$^+$ while 14.16% are only PI$^+$. The total percentage of FITC$^+$ cells obtained after a total incubation time of 48h (24h before + 24h after the laser illumination) is 57.42% (31.29% + 26.13%, **Figure 4.24 E**), in line with the data obtained after a 48h incubation without any illumination process (i.e. 68.4%, **Figure 4.21 D**).

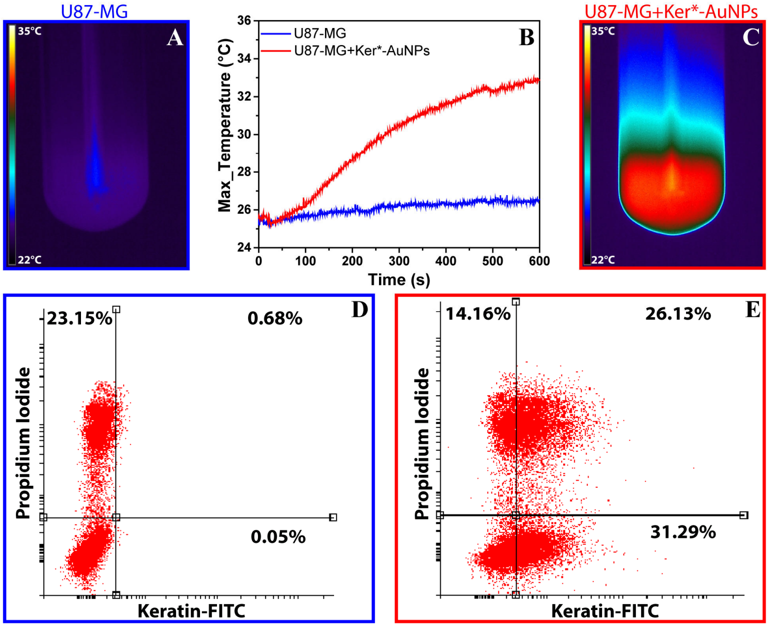

Figure 4.24 *– (A, C) Thermographic images of U87-MG cells alone and incubated with Ker*-AuNPs under laser illumination, (B) along with the corresponding temperature profiles (blue and red curves), (D) biparametric cytofluorimetric analysis of PI staining showing dead U87-MG cells irradiated for 10 min alone and (E) incubated for 24h with Ker*-AuNPs and then irradiated for 10min. Dead cells were evaluated 24h after the irradiation.*

A trypan blue exclusion assay (**Figure 4.25**) was performed to evaluate the percentage of viability of U87-MG cells incubated for 24h with Ker*-AuNPs. Percentages of cell viability were calculated relative to the control cells (100% viability), to take into account the intrinsic cell death, (t 0) immediately after irradiation, (t 4) at 4h after irradiation, and (t 24) at 24h after irradiation.

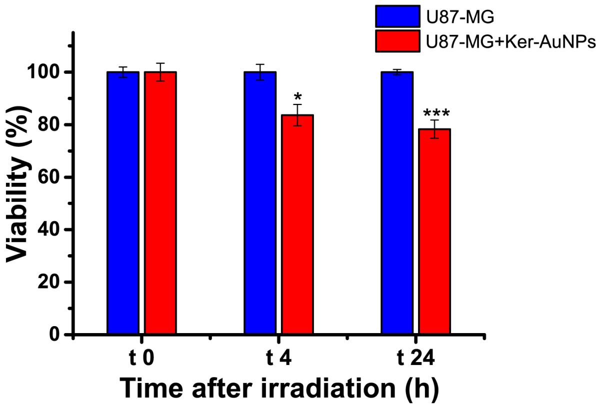

Figure 4.25 *– Trypan blue test results of U87-MG cells incubated and not with Ker-AuNPs at (t 0) immediately after irradiation, (t 4) at 4 h after irradiation, and (t 24) at 24 h after irradiation. (*: $p<0.05$; ***: $p<0.001$).*

The viability percentage assessed immediately after the experiment did not show any significant variation. After 4h from the PPT experiments, the percentage of live cells was decreased by about 17%, compared to the control sample.

An even more substantial reduction in the cell viability of about 22% was observed 24h after irradiation, compared to control samples, comparable with the biparametric cytofluorimetric analysis results. These data highlight that localized photo-thermal heating produced by Ker*-AuNPs is highly selective and confined, with the capability to suppress (kill) predominantly the U87-MG cells that can uptake Ker*-AuNPs.

So, in conclusion, PPT experiments performed by means of the high-resolution thermographic optical setup, have shown that the achieved macroscopic temperature increase after 10 min of laser illumination is ≊35°C (**Figure 4.24 B**, red curve). Although this value is below the minimum threshold to induce cell mortality (≈ 42°C)[86], a reduction of the cell viability of ≈ 30 % (**Figure 4.24 E**) has been measured.

This result can be explained by considering that the temperature at the Ker*-AuNPs surface (which are stuck/penetrated on/in the cell membrane) reaches higher values, hence producing a very effective photo-thermal and/or photo-mechanical damaging.[57]

Spherical AuNPs were used here as model NPs for PPTT, to demonstrate that using a protein coating of keratin on the NPs' surface can preserve their inherent biocompatibility, facilitating their use as a nanotherapeutic. Ker-AuNPs are stable when dispersed in a physiological environment and when heated at high temperatures with a laser, owing to the stability of the Cysteine-gold bond. The physical interaction given by the keratin coating facilitated adsorption and internalization on cells, improving the efficacy of the localized heating promoted by the light.

The optical limitations caused by having the LSPR in the visible region will be overcome by studying a new generation of keratin coated AuNPs with different shapes such as rods and triangles. They both possess higher photo-thermal efficiency[58] as well as LSPR bands centered in the first biological window[243], where cells and growth media are more optically transparent.

Conclusions and Outlook

Nanobiophotonics, including the use of remotely light-triggered and spectrally selective nano-heaters, has emerged as a major thrust area of nanobiotechnology. In this thesis, several AuNPs were tested as efficient, biocompatible, light-to-heat converter when shined on at their plasmonic resonance. This strategy is based on a rapidly growing and promising biophotonic approach called plasmonic photothermal therapy (PPTT), for applications ranging from treating cancer-related diseases to the total eradication of bacterial infections. Furthermore, the PPT phenomenon applications extend to many other applications such as the disinfection of drinking water, the implementation of biosensors, and the manufacture of sunlight-driven smart windows.

In the first part of the thesis, we theoretically describe the localized surface plasmon resonance (LSPR) optical process and the Joule effect induced in plasmonic AuNPs. We show that the resonant oscillation of the free electron cloud at the AuNP surface significantly enhances the absorption cross section and, consequently, light-to-heat conversion. Furthermore, it has been described how by simply acting on the shape, functionalization, and refractive index of the medium surrounding the AuNP, it is possible to shift the plasmon band in the desired spectral range conveniently, and how this can then be inversely exploited to detect chemical-physical changes of the AuNP host material. These general concepts were then put into practice in various applications in both physical and biological environments.

In particular, in the third chapter, the distinctive capabilities of thermotropic LCs to control the LSPR of AuNPs are illustrated, along with the investigation of their potential use to realize active plasmonic nanodevices. By acting on the LCs properties, the LSPR can be actively controlled without modifying the intrinsic properties of the NPs. Further progress in this direction is represented by the possibility to use a surrounding medium whose dielectric function can be controlled through external stimuli such as temperature variations. This thermo-responsive behavior exclusively gives the LCs the dual ability to act as nano-thermometers, visibly manifesting variations in temperature undergoing variations in optical properties. In detail, by exploiting the fruitful combination of AuNPs and LCs, we have created a command layer for anisotropic PPT effects in LCs, and a thermoresponsive large-area plasmonic architecture acting like a remotely controllable mirror.

The first LCs application, showed the photo-anisotropic properties of a particular command layer for LCs, an azobenzene photo-aligning layer (PAL), to control the PPT response ensemble of homogeneously and uniformly distributed AuNPs. We have observed a correlation between the photo-induced heat and the PAL material's optical properties in terms of refractive index and thermal conductivity. Interestingly, the temperature increase can be controlled by varying PAL molecules' orientation thanks to the intrinsic variation of their thermal conductivity, so the PAL influences the AuNPs layer thermal response in an anisotropic way.

The second LCs application reported a hybrid cell composed of AuNPs and CLC, characterized by the typical helix structure. The system demonstrates that suitable optical radiation can mutually affect both the plasmonic and photonic properties of the system. Indeed, both the CLCs selective reflection properties and AuNPs frequency of the LSPR are modulated. Ultimately, the two-hybrid systems AuNPs / LCs, on the one hand, represent a starting point for the realization of thermo-plasmonic assisted LC-based optical devices with reconfigurable thermal conductivity and refractive index. They can be integrated into modern photonic components such as controllable light filters, smart mirrors, and nanoscale thermometers.

Having extensively explored the intriguing properties of LCs, we realized the lack of a fundamental prerequisite for moving towards biomedical applications, namely the biocompatibility. So the next part of the third chapter focuses on using a hydrogel, a smart material, reactive to external stimuli, and biocompatible. This part describes the morphological, optical, and thermo-optical properties of a temperature-sensitive hydrogel poly(N-isopropylacrylamide-co-N-isopropylmethacrylamide) [P(NIPAm-co-NIPMAm]) film containing gold nanorods (AuNRs). We demonstrated the concept of a light-controlled optical beam attenuator by combining GNRs and a responsive hydrogel (P(NIPAm-co-NIPMAm)) material. The optical behavior at the base of this device is straightforward and intuitive. As the temperature increases, the hydrogel goes from a transparent to an opaque state, thus acting as a light attenuator controllable by light. The optical transparency can be modulated using light irradiation resonant with the longitudinal plasmonic resonance of the AuNRs. These experiments allowed us to test a new generation of smart windows that could be activated by sunlight.

The fourth chapter shows the applications of photoinduced heat by biocompatible AuNPs interacting with the living biological world. Taking advantage of the mesophilic characteristic of the E. coli bacterium and its poor ability to survive if exposed to high temperatures, we decided to exploit the AuNRs, as a photothermal-based antimicrobial nano-tool, suitably activated by NIR light, in the "biological window". Viability experiments evidenced that the proposed system, reaching a $T \approx 50°C$ in about 5 min, accomplished a killing efficiency suitable for reducing the E. coli population of about 2 log CFU (colony-forming unit). Hence, the reported all-optical methodology based on the capability of GNRs to convert NIR radiation into heat for an antibacterial application proved to be very promising.

Encouraged by the very positive feedback obtained by exploring the AuNPs-based PPTT on the bacterial population, we decided to step forward further, testing the PPTT on Glioblastoma multiforme (GBM), one of the most lethal and destructive brain cancer, impressively resilient to current treatments. For this application, we used an innovative generation of AuNPs coated with a protein, keratin. These nanoparticles, Ker-AuNPs, exhibited exceptional biocompatibility, excellent thermal stability, massive cellular uptake, and remarkable photothermal and thermo-plasmonic killing capabilities.

The reported structural and functional properties pointed out these Ker-AuNPs as a promising new tool in the field of biocompatible photo-thermal agents for PPT treatments against cancer-related diseases.

Ongoing efforts are devoted to combining spherical Ker-AuNPs with other cancer cell lines such as melanoma, breast and colorectal cancer, and tumor animal models by performing both in vitro and in vivo experiments. Simultaneously, we are working on a new generation of Ker-AuNPs with different geometries and surface functionalization for improving both photo-thermal properties and cellular uptake. However, we believe that our results are already promising and can be used to synergistically enhance the efficacy of immunotherapy or chemotherapy, in the fight against solid tumors, and to realize a new generation of light assisted and on-demand antimicrobial therapies to eradicate antibiotic resistance.

Furthermore, the next steps will be aimed at implementing the transition from nano-therapy to nano-theranostics. To achieve this ambitious goal, the conjugation of AuNPs with radio-tracer molecules is envisaged, to be able to detect the precise location of the nano-agent, through nuclear medicine diagnostic techniques, even before carrying out the PPTT. Based on the combination of targeting, detection, and therapy, this visionary approach will be tested in a 3D bioprinted model of human primary glioblastoma. The end-goal is to perform an in vitro-in vivo correlation unlocking the possibility to realize innovative studies based on an animal-free glioblastoma cancer model.

APPENDIX

A1. Optical waveguide for PPTT of deep tumor

Due to PPTT's nature, localized solid tumors (like breast cancer, head and neck cancer, melanoma) are more suitable for treatment. However, using optical fibers to deliver light into deep tissues makes it possible to achieve photo-thermal treatment to deeply buried tumors.[86]

In this framework, we studied a multi-photon fabrication of compact low-loss optical waveguides in polydimethylsiloxane (PDMS) for PPTT in vivo applications (as a possible strategy for light-triggered plasmonic heating in deep tumors), preliminary focusing on the possibility of tuning light exploiting an all-optical mechanism.

Highly flexible and optically transparent polymers such as the PDMS are exploited for optical power delivery, testing the feasibility of using PDMS waveguides for the transcutaneous transfer and transmission of optical energy several cm into the tissue.[244]

Indeed, PDMS is a kind of silicon-based organic polymers and is particularly known for its flexible mechanical property to be biocompatible with tissues. PDMS is optically transparent, bioinert, non-toxic, and biodegradable, and can be applied in phototherapy and optical sensing.[2]

We present and discuss the realization and characterization of a high refractive index contrast, low-loss, compact, and reconfigurable optical waveguide realized in the bulk of a PDMS layer covered with a well-oriented NLCs film. The optical waveguide is realized by utilizing a multi-photon direct laser writing technique and exploiting a photo-induced radical chain polymerization process. A photo-alignment layer, deposited on the PDMS waveguide, is used as a light-sensitive command layer for varying the refractive index of the NLC film which, in its turn, acts as a reconfigurable cladding for the underlying optical waveguide. The proposed device allows the realization of a light controllable optical waveguide very useful for several applications such as flexible optical circuit boards, wearable, implanted photonic devices, and potentially for in-vivo application of PPTT for deep tumor.

Two-Photon Polymerization Process Development

Optical waveguides are one of the most important photonic components. Optical waveguides are a key element in the development of multifunctional platforms with tailored geometries, such as biomedical and biosensor platforms.[17] In a common slab waveguide, made of three layers of materials with different dielectric constants, the light can be confined in the middle layer by total internal reflection. This occurs only if the middle layer's (core) refractive index is larger than that of the surrounding layers (cladding). Several techniques aiming at inducing a refractive index change in polymers have been developed.

The process of polymer waveguide fabrication in PDMS through laser direct writing and multiphoton polymerization, without using a photoinitiator, was developed for the first time in the Optics Laboratory (LO), École Polytechnique Fédérale de Lausanne (EPFL).[17]

In two-photon polymerization (2PP) the characteristic three-dimensional (3D) spatial resolution of the simultaneous two-photon absorption (2PA) process is used for 3D photoinitiated polymerization.[245] Multiphoton absorption has been defined as simultaneous absorption of two or more photons via virtual states in a medium with an extremely short lifetime (several femtoseconds, fs). Thus, 2PA is only possible if a second photon is absorbed before the decay of this virtual state (**Figure A.1 c**). The process requires a high peak power, which is available from pulsed laser systems. A major feature that distinguishes single-photon absorption from two-photon absorption is the rate of energy (light) absorption as a function of incident intensity. In single or one-photon absorption, the rate of light absorption is directly proportional to the incident light intensity, while for two-photon absorption, the rate of light absorption is proportional to the square of the light incident intensity.[246] This non-linear intensity dependence of the absorption process has substantial implications. While in a medium containing one-photon absorbing chromophores, absorption occurs all along the path of a focused beam, leading to out-of-focus absorption and associated processes. In the two-photon process, absorption occurs only near the focal point.[247] This allows spatial resolution along the beam axis and in the radial direction and is the principle behind the two-photon fluorescence imaging and two-photon microfabrication. This creates a bright light point in the sample without the usual cone of light above and below the focal plane (**Figure A.1 b**, **d**), the hourglass shape is replaced by a point source since there are almost no excitations away from the focal point.

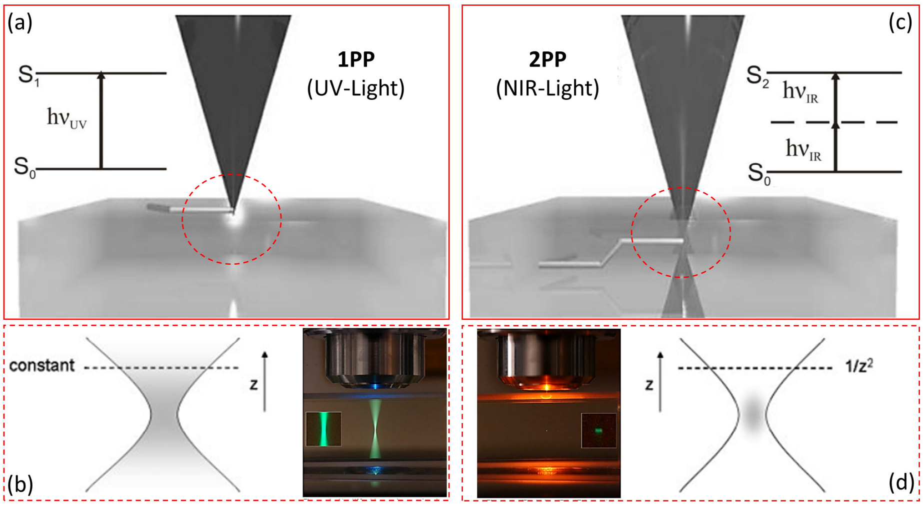

Figure A.1 *– Schematization of single-photon and two-photon process. (a) UV laser induces polymerization through single-photon absorption at the material's surface. (c) Focused NIR fs laser pulses trigger 2PP within the material's small volume. (d) The 2PA non-linear intensity allows a confined polymerization because radical formation decays as* $1/z^2$*, where z is the axial distance away from the focal plane. The hourglass shape (b) is replaced by a point source (d).*

From a chemical point of view, the 2PP technique is based on fs laser radiation interaction, which triggers a highly localized chemical reaction leading to polymerization of the photosensitive material with current resolution down to 100 nm. Polymerization is a process in which monomers or weakly cross-linked polymers (liquid or solid) interconnect and form a 3D network of highly cross-linked polymer (solid). Photoinitiators are often added to increase the material photosensitivity.

A material is polymerized along the trace of the moving laser focus, thus enabling fabrication of any desired polymeric 3D pattern by direct "recording" into the volume of photosensitive material. In a subsequent processing step, the unpolymerized material, which was not exposed to the laser radiation is removed, and the fabricated structure is revealed. The material sensitive in the UV range (λ_{UV}) can be polymerized by irradiation with the infra-red light of approximately double wavelength ($\lambda_{IR}=2\lambda_{UV}$), under the condition that the intensity of the radiation is high enough to initiate two-photon absorption.

In order to accommodate the tight space constraint and requirement for biocompatibility, it was piloted a new photochemistry route that eliminates the use of photoinitiators and achieved waveguides of ~1 µm wide.

The host-guest system we considered in this project includes a PDMS matrix as the host and a liquid monomer permeated into the PDMS intermolecular space as the guest. Besides being polymerizable with good reactivity, requirements on the monomer formulation include: (i) the refractive index of the monomer must be higher than that of the PDMS host matrix; (ii) the monomer molecule must be small and nonpolar to allow for a high solubility in PDMS and an easy extraction after laser exposure; (iii) the absorption spectrum of the monomer must not overlap with the PDMS host.[17]

Based on these considerations, it was identified phenylacetylene as the best candidate, that readily achieves photoinitiator-free multiphoton polymerization in PDMS.

However, it was soon realized that the fabrication using the photoinitiator-free phenylacetylene process is subject to defects due to material damage possibly resulted from uncontrollable beam collapse because of a strong nonlinear optical self-focusing. Furthermore, the writing of very shallow waveguides in the PDMS was subject to the burning of the material.

In light of the stability and burning issue, the fabrication protocol was modified, adopting a photoinitiator approach,[248] with divinylbenzene (DVB, refractive index n=1.561) monomer combined with a suitable commercial photoinitiator, Irgacure OXE02 (λ= 337 nm), the chemical scheme of which is shown in **Figure A.2 a**. Owing to the two polymerizable sites in each DVB monomer molecule, the formed crosslinks in the polymer, increase the overall molecular weight, and reduce the mobility of the molecules. The cross-link in the polymer structure substantially enhances the polymer molecules' stability, which forms the core of the waveguides.

The optical waveguides' fabrication technique employs photo-induced radical chain polymerization initiated by divinylbenzene (DVB) monomer and Irgacure OXE02 photoinitiator molecule. The fabrication procedure of the waveguides consists of four steps (**Figure A.2**) : (i) the preparation of a pristine PDMS slab with a 10:1 mixing ratio between base and curing agent; (ii) the infusion of the monomer+photoinitiator into the PDMS matrix by soaking the PDMS slab in the DVB+IrgacureOxe02 (5 wt%) liquid formulation for 120 hours; (iii) the exposure of the monomer-infused PDMS slab to focused ultrashort laser irradiation; and (iv) the removal of the unreacted monomer through different ethanol washing.

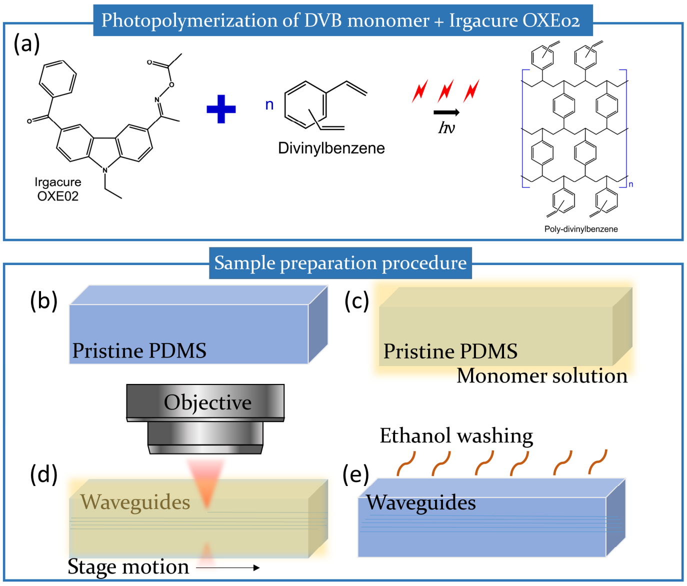

Figure A.2 *– (a) Chemical scheme for the 2PP laser fabrication of polymer optical waveguides using DVB monomer and commercial photoinitiator Irgacure OXE02. Principle of waveguides fabrication in PDMS: (b) preparation of a pristine PDMS substrate; (c) permeation of the monomer molecules into the PDMS matrix; (d) exposure of the monomer-permeated PDMS substrate to focused ultrashort laser irradiation for waveguide writing; (e) removal of the unreacted monomer through ethanol washing. Adapted from* [248].

We used a femtosecond Ti:Sapphire laser (Coherent Chameleon Ultra II, 80 MHz repetition rate, 140 fs pulse width) tuned to 680 nm, which allowed for efficient initiation of polymerization reaction through multi-photon absorption in the DVB+IrgacureOxe02 molecules. The laser beam was focused with a long-working distance, water-immersion objective (0.7 NA) into the PDMS slab (**Figure A.3**). Considering an average laser power at the level of 60 mW, 680 nm wavelength source, and 0.8 NA lens, we estimate that the focal intensity, ignoring the spherical aberration due to the refractive index mismatch, and the possible self-focusing effect, reaches approximately 2×10^{12} W/cm^2 with fine adjustments by tuning the laser power. The DVB-permeated PDMS slab sample was sandwiched between a glass microscope slide and a coverslip (**Figure A.3 a**). To control the depth position of the laser focus, we used a dichroic mirror (50% T/R @650 nm) to steer the full power of the laser beam for writing while allowing a minimal amount of leaked laser light reflected from the top surface of the sample coverslip to reach the CMOS camera after a focusing lens. A good focus spot on the camera indicates that the laser focuses on the top surface of the coverslip, and the consequent control depth is achieved by moving the objective using the translation stage with a micrometer drive.

Numerous tests were carried out before reaching the correct combination of writing speed and laser power to obtain shallow and defect-free waveguides. Ultimately, the waveguides were recorded at writing speeds ranging between 1.8 and 2.5 mm/s, at an average laser power between 60 and 70 mW. At a focusing depth between 450 µm and 25 µm below the sample top surface.

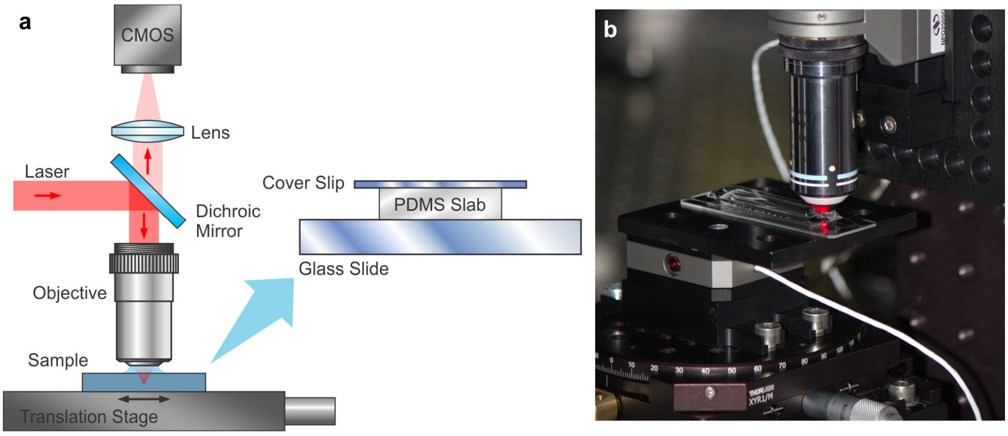

Figure A.3 *– Fabrication system for waveguide writing in PDMS. (a) Schematic illustration of the fabrication system. After beam expansion, the laser beam's full power is steered by the dichroic mirror to the high NA water immersion objective for waveguide writing in the PDMS sample, illustrated in the blow up on the right. A minimal amount of leaked laser light is reflected from the top surface of the sample coverslip reaching the CMOS camera to control the focus depth position. The waveguide shape is controlled by the path of motion set to the stage carrying the sample. (b) Photograph of the writing objective, sample holder, and motion stages. Adapted from* [17].

Waveguides characterization

The waveguides were characterized in terms of:

- dimension and shape with a phase-contrast microscope;
- refractive index contrast ($\Delta n = n_{core} - n_{cladding}$) by means of a custom-made off-axis interferometric imaging system, which turns out to be $\Delta n \approx 0.09$;
- light transmission, coupling linearly polarized white light and HeNe laser light (633 nm), into the waveguides, using a 50x0.8 NA objective and imaged the output using a digital CMOS camera.

A phase-contrast microscope (Nikon IX-71) was used to investigate the sample after the writing process. The phase-contrast images clearly reveal the formation of the waveguides and a smooth core refractive index structure. An example phase contrast image of the waveguides is shown in **Figure A.4**, which were fabricated at 450 µm and 30 µm depth inside the PDMS material, with different peak laser intensity and writing speed. The width of the waveguide was measured to be 0.5µm.

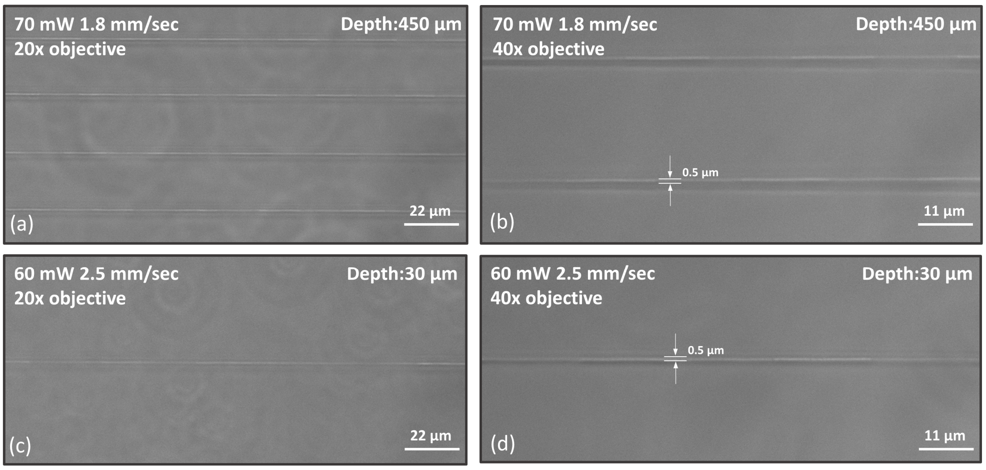

***Figure A.4** – Phase-contrast microscope (Nikon IX-71) images of PDMS optical waveguides written at (a,b) 450µm below the sample top surface, with 70mW laser power and 1.8 mm/s writing speed (20x, 40x magnification objective respectively), and (c,d) 30µm below the sample top surface, with 60mW laser power and 2.5 mm/s writing speed (20x, 40x magnification objective respectively).*

The experimental parameters that determine the focal volume's width, and therefore the resulting feature size, are the pulse energy, the writing speed, and the numerical aperture of the lens used to focus the beam on the sample. In conclusion, shallow waveguides can be written at a lower intensity and higher speed after several tests.

Liquid crystal device fabrication

Once the waveguides are written via the 2PP process, described as previous, into the monomer-infused PDMS slab, and all the unreacted monomer is removed through different ethanol washing, we proceed with the steps that lead to the formation of the final device (**Figure A.5**) with NLCs.

A thin photoaligning layer (PAL) of BY (Brilliant Yellow Dye by Sigma-Aldrich) dissolved in DMF (0.5 wt%) was deposited on the top of the waveguides embedded in the PDMS, using a spin coater (RPM:2000, dwell time:60s), after a PDMS surface activation with an oxygen plasma treatment (45sec). To obtain a nanometric thin, uniform, and homogeneous layer of BY, it was essential to set all the parameters accurately. Then the BY substrate undergoes a UV exposure, in the ELC-500 UV Cure Chamber, (I=30 mW/cm^2, λ=365 nm, $exposure\ time$=20 min), to reorient the BY molecules perpendicularly to the incident light polarization. Then, exploiting the capillary force, NLC (4′-Pentyl-4-biphenylcarbonitrile-5CB) is infiltrated between the PDMS substrate and the glass substrate coated with a thin BY layer to induce planar alignment of the NLC molecules, perpendicular to the WGs. The final thickness of the NLCs layer is d≅5 μm. The gap was created using a mixture of glue and silica microbeads.

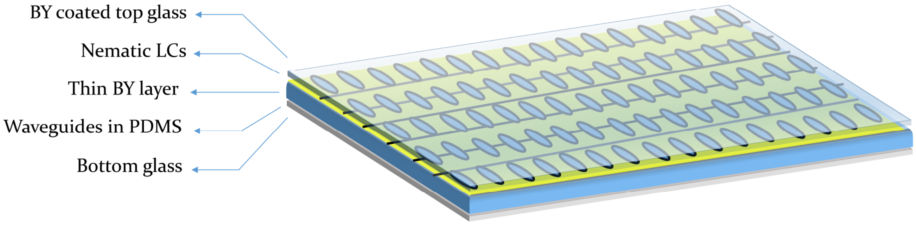

Figure A.5 *– A Layer-by-layer schematization of the final NLCs/PMDS waveguides device.*

At the end of the device realization, to check NLCs alignment, the sample was observed between two crossed polarizers. In this configuration, with the molecular director perpendicular to waveguides, we want to explore the polarization-sensitive optical response probing the output, acting on light polarization in input, as described below.

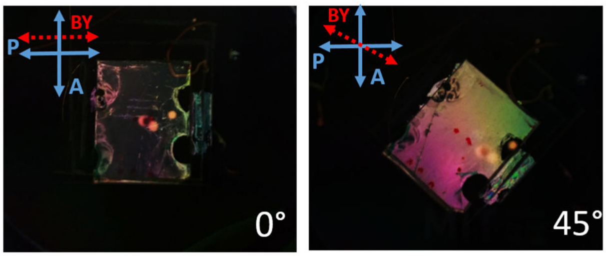

Figure A.6 *– Check of the LCs alignment, observing the NLCs/PMDS waveguides cell between crossed polarizers.*

The all-optical method, based on the presence of a thin layer of photo-aligning molecules, is advantageous because of its simple implementation and low cost, compared with traditional techniques that use electric fields to control the orientation of NLCs.[249]

Light coupling experiments

We coupled white light from a halogen lamp passing a 1-mm iris into the waveguide using a 50×0.8 NA objective and a 633 nm HeNe laser to test the light transmission. We imaged the output using a digital CMOS camera (CMOS2).

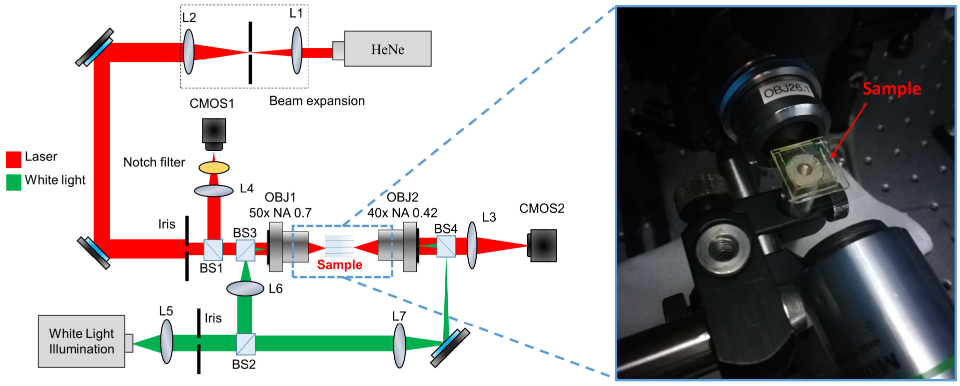

Figure A.7 *– (a) Optical set-up for white light and HeNe laser waveguide coupling, along with a picture of the sample.*

Once we record the images from the output digital CMOS camera, all the (.FITS) data were analyzed using an implemented Matlab code. Image processing aims to extract the intensity value, which corresponds to the integral, calculated as the sum of the pixels value, after several steps summarized in the figure below.

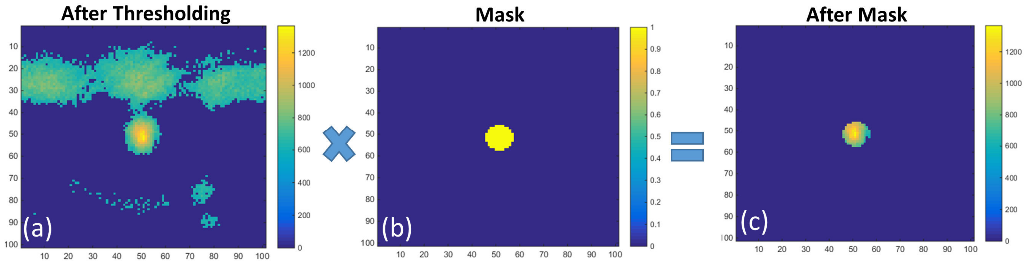

Figure A.8 *– Different steps to process the waveguide output images using an implemented Matlab code: (a) FWHM thresholding, (b) circular mask, and (c) final output.*

To obtain the final intensity values, we processed the output images, first using a calculated threshold based on the full width at half maximum (FWHM) and then applying a circular mask to focus only on the core of the waveguide where the light is confined. The threshold value is fixed as thr_val = 0.44 with respect to the maximum value, so every pixel having a value below this threshold is neglected. Simultaneously, for the circular mask around the waveguide core, we chose a diameter of 12µm, calculated from the experiments. We get only information on how light transmission is modified in this particular region, without considering the surrounding.

We performed a broadband spectral analysis, coupling white light combined with color filters (535-561-585-605-675) nm, to test light transmission's efficiency into the waveguides at different wavelengths.

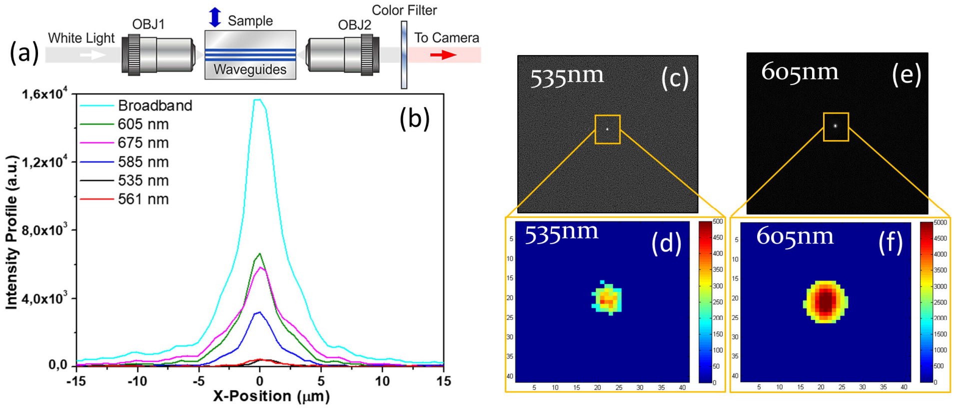

Figure A.9 *– Characterization of the waveguide light transmission. (a) Diagram of the optical set-up used for optical transmission characterization. (c) – (f) Filtered narrowband waveguiding output from the same waveguide (c, d) 535 nm, and (e, f) 605 nm.*

The intensity profile at 561 nm and 535 nm is nearly zero (red and black curves in **Figure A.9 b**, respectively), suggesting that the transmission is mainly located in the 585-605 nm wavelength range. In particular, in **Figure A.9** it is possible to appreciate the difference between the light intensity at the waveguide's output at 535 and 605nm.

To check the waveguide polarization-dependent behavior, a laser beam (633nm) was coupled into the waveguides changing its polarization direction with a λ/2, performing an entire rotation of the polarization angle starting from 0° to 180° at 10° steps.

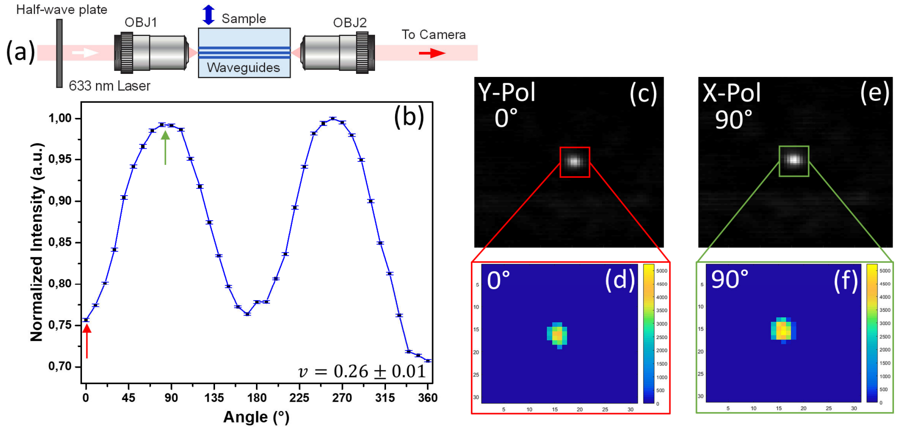

Figure A.10 *– Characterization of waveguide polarization-dependent behavior. (a) Diagram of the optical set-up used for optical transmission characterization. (c) – (e) Mean value of 100 scans waveguiding output from the same waveguide (c, d) 0°(Y-Pol.), and (e, f) 90° (X-Pol.). Images (d,f) were obtained applying a mask and a threshold to (c,d) images.*

To eliminate errors due to the intrinsic oscillations of the laser from the intensity measurement, it was decided to acquire 100 frames for each angle value and then calculate the average value. The visibility parameter gives information on how much the intensity values at the different polarizations differ from the average intensity value:

$$visibility = (I_{X-pol.} - I_{Y-pol.})/\bar{I} \tag{A.1}$$

$$visibility\ error = \bar{\sigma}/\bar{I} \tag{A.2}$$

Where $\bar{I}$ is the normalized intensity mean value. From the curve's sinusoidal trend in **Figure A.10 b**, it can be deduced that the waveguide couples more efficiently the X-polarized light (90°-270°). The intrinsic waveguide birefringence is due to the material and structural asymmetry that causes the TE and TM waves to see different material interfaces and propagate differently.

Randomly oriented NLC effect

Once we discover that the waveguides could efficiently transmit the light inside the core, we decided to test the effect of a NLCs layer on light transmission. To carry out this preliminary test, we proceeded by placing a drop of NLC above the waveguides, therefore without being oriented or aligned, and measuring white light coupling (optical setup **Figure A.7**).

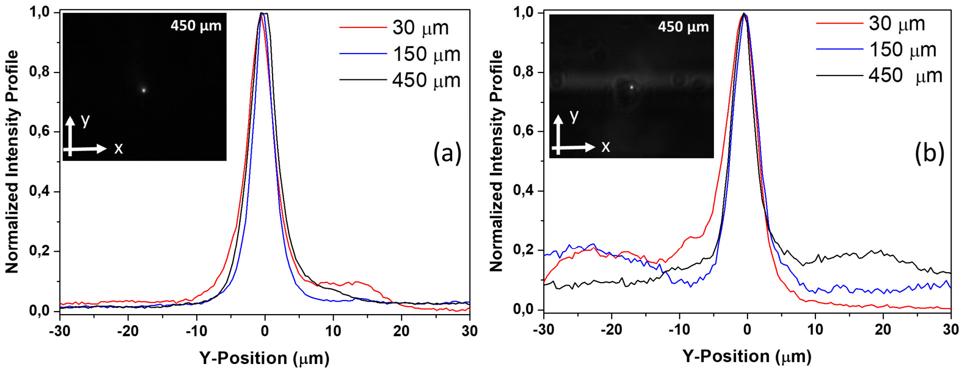

***Figure A.11** – LCs effect on the incoherent light coupling. Output intensity profile of three simple waveguides without (a) and with (b) a NLCs droplet on top. Waveguide outputs are displayed in the image inset.*

Our analysis suggests that the NLC effect on light transmission into small and shallow submicron waveguide is evident like a sort of “leaky mode", which cannot sufficiently confine the optical mode field. The evanescent wave field extending outside of the waveguide, along the Y direction (i.e. the “leaky mode”, evident in the inset of **Figure A.11** b), would couple and diffuse light into the overlying NLC layer which, has a higher refractive index. This result is following the fact that optical fibers as waveguides can be used as sensors to measure strain, temperature, pressure, displacements, vibrations, and other quantities, indeed the evanescent field excitation is employed to sense the environmental refractive index changes.[1]

Oriented NLC effect

Since the NLC is placed on the waveguide with the molecular director perpendicular to the light propagation direction, it will act as a tunable cladding concerning a change in light's incoming polarization direction. So if this cladding index is lower than the core index, the light propagates. Otherwise, when the index is higher the light is no longer guided, depending on the NLC refractive index experienced by the light (ordinary or extraordinary index respectively). To probe this mechanism, we carried out measurements using the same setup in the **Figure A.10 a**, which uses a 633nm laser beam to couple the waveguide, whose polarization direction is varied using a λ/2 plate. We perform this experiment coupling one of the shallower waveguides realized in the PDMS, depth=24.72 ± 2.4 µm. With light propagating with Y-Pol (λ/2 = 0°, 180°, and 360°), the light interacts with the NLC ordinary index $n_o \cong n_{waveguide}$, $n_o = 1.536\ in\ \lambda = (450 \div 656)\ nm$,[250] so the intensity should propagate without being or slightly affected. In comparison, for X-Polarized light (λ/2 = 90° and 270°) the light experiences the extraordinary index of the NLC $n_e > n_{waveguide}$, $n_e = 1.714$ in $\lambda = (450 \div 656)\ nm$,[250] therefore the light should be diffused therefore less confined in the core. Looking at the visibility parameter in **Figure A.12 b,c**, it is evident that the presence of a perpendicularly oriented film of NLCs, acts, although only minimally, on light transmission, decreasing this value, right at the angles corresponding to the input polarization X (90°, 270°), when the light experiences the NLC extraordinary index.

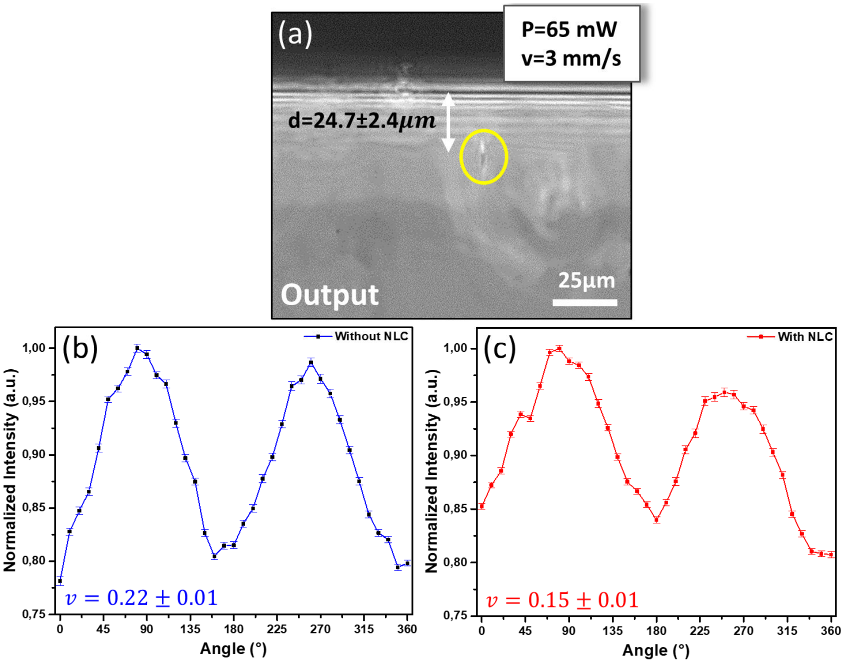

Figure A.12 *–Effect of the polarization direction of a laser beam input coupling the same waveguide (a) (depth 24.7µm) without (b) and with (c) NLCs.*

It is important to note that the effect is not very pronounced, this is probably due to waveguides depth in the PDMS and therefore to the distance of the propagating light from the NLC. In fact, using the beam propagation method (BPM) for simulating the propagation of a coherent beam of light through the waveguide, it emerged that for light to be substantially affected, it would be necessary to have very superficial waveguides, at a depth of maximum 2µm, to be almost in contact with the NLCs.

In conclusion, we have demonstrated that compact optical waveguides can be fabricated in PDMS, through multi-photon laser direct writing, and uniformly covered with a well-oriented NLCs film. We achieved the polymerization by tuning the writing laser wavelength to 680 nm such that the absorption band of the photoinitiator is reached via multi-photon absorption. The smallest and shallowest waveguides we fabricated are 0.5 µm wide and 25 µm deep inside the PDMS material. After we were able to optically align a 5 µm thick layer of NLCs exploiting the photo-alignment properties of a thin layer of BY. The experiments performed so far aimed to assess NLC's influence on the light transmission through the waveguides. Furthermore, the preliminary results obtained give a proof-of-concept of the NLC ability to tune the light inside the waveguides, exploiting its intrinsic birefringence by changing the input light polarization when LCs alignment is established. Nevertheless, further experiments are needed to verify how the light inside the waveguides can be tuned, acting on the LC molecules configuration working with a fixed light polarization direction. We expect such waveguides will receive a wide range of applications in biosensors, microfluidic flow cytometry, wearable photonic devices, electro-elastic optical modulators, flexible optical circuit boards, and optical neural networks.

References

(1) Amiri, I. S.; Azzuhri, S. R. B.; Jalil, M. A.*, et al.* Introduction to photonics: Principles and the most recent applications of microstructures. *Micromachines* **2018,** *9* (9), 452.

(2) Wang, J.; Dong, J. Optical Waveguides and Integrated Optical Devices for Medical Diagnosis, Health Monitoring and Light Therapies. *Sensors* **2020,** *20* (14), 3981.

(3) Song, J.; Qu, J.; Swihart, M. T.; Prasad, P. N. Near-IR responsive nanostructures for nanobiophotonics: Emerging impacts on nanomedicine. *Nanomed. Nanotechnol. Biol. Med.* **2016,** *12* (3), 771-788.

(4) De Sio, L.; Placido, T.; Comparelli, R*., et al.* Next-generation thermo-plasmonic technologies and plasmonic nanoparticles in optoelectronics. *Prog. Quantum Electron.* **2015,** *41*, 23-70.

(5) Maier, S. A. *Plasmonics: fundamentals and applications*, Springer Science & Business Media: 2007.

(6) Atwater, H. A. The promise of plasmonics. *Sci. Am.* **2007,** *296* (4), 56-63.

(7) Baffou, G.; Cichos, F.; Quidant, R. Applications and challenges of thermoplasmonics. *Nat. Mater.* **2020**, 1-13.

(8) Ayala-Orozco, C.; Urban, C.; Bishnoi, S.*, et al.* Sub-100 nm gold nanomatryoshkas improve photo-thermal therapy efficacy in large and highly aggressive triple negative breast tumors. *J. Control. Release* **2014,** *191*, 90-97.

(9) Ali, M. R.; Ibrahim, I. M.; Ali, H. R.; Selim, S. A.; El-Sayed, M. A. Treatment of natural mammary gland tumors in canines and felines using gold nanorods-assisted plasmonic photothermal therapy to induce tumor apoptosis. *Int. J. Nanomedicine* **2016,** *11*, 4849.

(10) Vines, J. B.; Yoon, J. H.; Ryu, N. E.; Lim, D. J.; Park, H. Gold Nanoparticles for Photothermal Cancer Therapy. *Front Chem* **2019,** *7*, 167.

(11) Baffou, G.; Quidant, R.; Girard, C. Heat generation in plasmonic nanostructures: Influence of morphology. *Appl. Phys. Lett.* **2009,** *94* (15), 153109.

(12) Zhang, J. Z. Biomedical applications of shape-controlled plasmonic nanostructures: a case study of hollow gold nanospheres for photothermal ablation therapy of cancer. *The Journal of Physical Chemistry Letters* **2010,** *1* (4), 686-695.

(13) Stern, J. M.; Stanfield, J.; Kabbani, W.; Hsieh, J.-T.; Cadeddu, J. A. Selective prostate cancer thermal ablation with laser activated gold nanoshells. *The Journal of urology* **2008,** *179* (2), 748-753.

(14) Castillo-Martínez, J. C.; Martínez-Castañón, G. A.; Martínez-Gutierrez, F.*, et al.* Antibacterial and antibiofilm activities of the photothermal therapy using gold nanorods against seven different bacterial strains. *Journal of Nanomaterials* **2015,** *2015*.

(15) Pihl, M.; Bruzell, E.; Andersson, M. Bacterial biofilm elimination using gold nanorod localised surface plasmon resonance generated heat. *Mater. Sci. Eng. C* **2017,** *80*, 54-58.

(16) Meeker, D. G.; Jenkins, S. V.; Miller, E. K.*, et al.* Synergistic photothermal and antibiotic killing of biofilm-associated Staphylococcus aureus using targeted antibiotic-loaded gold nanoconstructs. *ACS infectious diseases* **2016,** *2* (4), 241-250.

(17) Panusa, G.; Pu, Y.; Wang, J.; Moser, C.; Psaltis, D. Photoinitiator-free multi-photon fabrication of compact optical waveguides in polydimethylsiloxane. *Optical Materials Express* **2019,** *9* (1), 128-138.

(18) Nguyen, A. K.; Narayan, R. J. Two-photon polymerization for biological applications. *Mater. Today* **2017,** *20* (6), 314-322.

(19) Bond, G. C. Introduction to the physical and chemical properties of gold. *Gold Nanoparticles for Physics, Chemistry and Biology, Imperial College Press, London* **2012**, 29-42.

(20) Baffou, G. *Thermoplasmonics: Heating Metal Nanoparticles Using Light*, Cambridge University Press: 2017.

(21) Ashcroft, N. W.; Mermin, N. D. *Solid State Physics*, Saunders College: 1976.

(22) Mayer, K. M.; Hafner, J. H. Localized surface plasmon resonance sensors. *Chem. Rev.* **2011,** *111* (6), 3828-3857.

(23) Fox, M., Optical properties of solids. American Association of Physics Teachers: 2002.

(24) Born, M.; Wolf, E. *Principles of optics: electromagnetic theory of propagation, interference and diffraction of light*, Elsevier: 2013.

(25) Johnson, P. B.; Christy, R. W. Optical Constants of the Noble Metals. *Physical Review B* **1972,** *6* (12), 4370-4379.

(26) Etchegoin, P. G.; Le Ru, E.; Meyer, M. An analytic model for the optical properties of gold. *The Journal of chemical physics* **2006,** *125* (16), 164705.

(27) Johansen, K.; Arwin, H.; Lundström, I.; Liedberg, B. Imaging surface plasmon resonance sensor based on multiple wavelengths: Sensitivity considerations. *Rev. Sci. Instrum.* **2000,** *71* (9), 3530-3538.

(28) Bohren, C. F.; Huffman, D. R. *Absorption and scattering of light by small particles*, John Wiley & Sons: 2008.

(29) Jackson, J. D., Classical electrodynamics. American Association of Physics Teachers: 1999.

(30) Israelachvili, J. N. *Intermolecular and surface forces*, Academic press: 2011.

(31) Kreibig, U.; Vollmer, M. Theoretical considerations. In *Optical properties of metal clusters*; Springer: 1995; pp 13-201.

(32) De Sio, L., *Active plasmonic nanomaterials*. CRC Press: FL, USA, 2015.

(33) Horvath, H. Gustav Mie and the scattering and absorption of light by particles: Historic developments and basics. *J. Quant. Spectrosc. Radiat. Transfer* **2009,** *110* (11), 787-799.

(34) Mie, G. Beiträge zur Optik trüber Medien, speziell kolloidaler Metallösungen. *Annalen der physik* **1908,** *330* (3), 377-445.

(35) Bohren, C. F.; Huffman, D. R. *Absorption and Scattering of Light by Small Particles*, Wiley: 1983.

(36) Jain, P. K.; Lee, K. S.; El-Sayed, I. H.; El-Sayed, M. A. Calculated absorption and scattering properties of gold nanoparticles of different size, shape, and composition: applications in biological imaging and biomedicine. *J. Phys. Chem. B* **2006,** *110* (14), 7238-7248.

(37) Huang, X.; O'Connor, R.; Kwizera, E. A. Gold nanoparticle based platforms for circulating cancer marker detection. *Nanotheranostics* **2017,** *1* (1), 80.

(38) Bardhan, R.; Grady, N. K.; Cole, J. R.; Joshi, A.; Halas, N. J. Fluorescence enhancement by Au nanostructures: nanoshells and nanorods. *ACS Nano* **2009,** *3* (3), 744-752.

(39) Bardhan, R.; Grady, N. K.; Halas, N. J. Nanoscale control of near-infrared fluorescence enhancement using Au nanoshells. *Small* **2008,** *4* (10), 1716-1722.

(40) Baffou, G.; Quidant, R. Thermo-plasmonics: using metallic nanostructures as nano-sources of heat. *Laser & Photonics Reviews* **2013,** *7* (2), 171-187.

(41) Govorov, A. O.; Richardson, H. H. Generating heat with metal nanoparticles. *Nano today* **2007,** *2* (1), 30-38.

(42) Dickerson, E. B.; Dreaden, E. C.; Huang, X*., et al.* Gold nanorod assisted near-infrared plasmonic photothermal therapy (PPTT) of squamous cell carcinoma in mice. *Cancer Lett.* **2008,** *269* (1), 57-66.

(43) Gobin, A. M.; Lee, M. H.; Halas, N. J*., et al.* Near-infrared resonant nanoshells for combined optical imaging and photothermal cancer therapy. *Nano Lett.* **2007,** *7* (7), 1929-1934.

(44) Henderson, T. A.; Morries, L. D. Near-infrared photonic energy penetration: can infrared phototherapy effectively reach the human brain? *Neuropsychiatr. Dis. Treat.* **2015,** *11*, 2191.

(45) Tsai, M.-F.; Chang, S.-H. G.; Cheng, F.-Y*., et al.* Au nanorod design as light-absorber in the first and second biological near-infrared windows for in vivo photothermal therapy. *ACS Nano* **2013,** *7* (6), 5330-5342.

(46) Cao, D.; Xu, C.; Lu, W.; Qin, C.; Cheng, S. Sunlight-Driven Photo-Thermochromic Smart Windows. *Solar Rrl* **2018,** *2* (4), 1700219.

(47) Zhu, H.; Wang, L. Smart window based on Cu7S4/hydrogel composites with fast photothermal response. *Sol. Energy Mater. Sol. Cells* **2019,** *202*, 110109.

(48) Loeb, S.; Li, C.; Kim, J.-H. Solar photothermal disinfection using broadband-light absorbing gold nanoparticles and carbon black. *Environ. Sci. Technol.* **2018,** *52* (1), 205-213.

(49) Loeb, S. K.; Kim, J.; Jiang, C.*, et al.* Nanoparticle enhanced interfacial solar photothermal water disinfection demonstrated in 3-D printed flow-through reactors. *Environ. Sci. Technol.* **2019,** *53* (13), 7621-7631.

(50) Pedrosa, P.; Vinhas, R.; Fernandes, A.; Baptista, P. V. Gold nanotheranostics: proof-of-concept or clinical tool? *Nanomaterials* **2015,** *5* (4), 1853-1879.

(51) Moores, A.; Goettmann, F. The plasmon band in noble metal nanoparticles: an introduction to theory and applications. *New J. Chem.* **2006,** *30* (8), 1121-1132.

(52) Amendola, V.; Pilot, R.; Frasconi, M.; Maragò, O. M.; Iatì, M. A. Surface plasmon resonance in gold nanoparticles: a review. *J. Phys.: Condens. Matter* **2017,** *29* (20), 203002.

(53) Blaber, M. G.; Arnold, M. D.; Ford, M. J. A review of the optical properties of alloys and intermetallics for plasmonics. *J. Phys.: Condens. Matter* **2010,** *22* (14), 143201.

(54) Chithrani, B. D.; Ghazani, A. A.; Chan, W. C. Determining the size and shape dependence of gold nanoparticle uptake into mammalian cells. *Nano Lett.* **2006,** *6* (4), 662-668.

(55) Verma, A.; Stellacci, F. Effect of surface properties on nanoparticle–cell interactions. *Small* **2010,** *6* (1), 12-21.

(56) Blanco, E.; Shen, H.; Ferrari, M. Principles of nanoparticle design for overcoming biological barriers to drug delivery. *Nat. Biotechnol.* **2015,** *33* (9), 941-951.

(57) Hernandez Montoto, A.; Montes, R.; Samadi, A.*, et al.* Gold nanostars coated with mesoporous silica are effective and nontoxic photothermal agents capable of gate keeping and laser-induced drug release. *ACS Appl. Mater. Interfaces* **2018,** *10* (33), 27644-27656.

(58) Chen, Q.; Qi, H.; Ruan, L.; Ren, Y. Experimental comparison of photothermal conversion efficiency of gold nanotriangle and nanorod in laser induced thermal therapy. *Nanomaterials* **2017,** *7* (12), 416.

(59) Averitt, R. D.; Westcott, S. L.; Halas, N. J. Linear optical properties of gold nanoshells. *JOSA B* **1999,** *16* (10), 1824-1832.

(60) Hu, M.; Chen, J.; Li, Z.-Y.*, et al.* Gold nanostructures: engineering their plasmonic properties for biomedical applications. *Chem. Soc. Rev.* **2006,** *35* (11), 1084-1094.

(61) Link, S.; El-Sayed, M. A., Spectral properties and relaxation dynamics of surface plasmon electronic oscillations in gold and silver nanodots and nanorods. ACS Publications: 1999.

(62) De Sio, L.; Klein, G.; Serak, S.*, et al.* All-optical control of localized plasmonic resonance realized by photoalignment of liquid crystals. *Journal of Materials Chemistry C* **2013,** *1* (45), 7483-7487.

(63) García, M. A. Surface plasmons in metallic nanoparticles: fundamentals and applications. *J. Phys. D: Appl. Phys.* **2011,** *44* (28), 283001.

(64) Underwood, S.; Mulvaney, P. Effect of the solution refractive index on the color of gold colloids. *Langmuir* **1994,** *10* (10), 3427-3430.

(65) Di Fabrizio, E.; Schlücker, S.; Wenger, J.*, et al.* Roadmap on biosensing and photonics with advanced nano-optical methods. *Journal of Optics* **2016,** *18* (6), 063003.

(66) Howes, P. D.; Chandrawati, R.; Stevens, M. M. Colloidal nanoparticles as advanced biological sensors. *Science* **2014,** *346* (6205).

(67) Palpant, B. Photothermal properties of gold nanoparticles. *Gold nanoparticles for physics, chemistry and biology* **2012**, 75-102.

(68) Kim, M.; Lee, J. H.; Nam, J. M. Plasmonic photothermal nanoparticles for biomedical applications. *Adv. Sci.* **2019,** *6* (17), 1900471.

(69) Govorov, A. O.; Zhang, W.; Skeini, T.*, et al.* Gold nanoparticle ensembles as heaters and actuators: melting and collective plasmon resonances. *Nanoscale Research Letters* **2006,** *1* (1), 84.

(70) Baffou, G.; Quidant, R.; García de Abajo, F. J. Nanoscale control of optical heating in complex plasmonic systems. *ACS Nano* **2010,** *4* (2), 709-716.

(71) Carslaw, H. S.; Jaeger, J. C. *Conduction of Heat in Solids*, Clarendon Press: 1959.

(72) Baffou, G.; Girard, C.; Quidant, R. Mapping heat origin in plasmonic structures. *Phys. Rev. Lett.* **2010,** *104* (13), 136805.

(73) Freddi, S.; Sironi, L.; D'Antuono, R.*, et al.* A molecular thermometer for nanoparticles for optical hyperthermia. *Nano Lett.* **2013,** *13* (5), 2004-2010.

(74) Palermo, G.; Sio, L. D.; Placido, T.*, et al.* Plasmonic thermometer based on thermotropic liquid crystals. *Mol. Cryst. Liq. Cryst.* **2015,** *614* (1), 93-99.

(75) De Sio, L.; Caracciolo, G.; Annesi, F.*, et al.* Photo-thermal effects in gold nanorods/DNA complexes. *Micro and Nano Systems Letters* **2015,** *3* (1), 8.

(76) Jauffred, L.; Samadi, A.; Klingberg, H.; Bendix, P. M.; Oddershede, L. B. Plasmonic heating of nanostructures. *Chem. Rev.* **2019,** *119* (13), 8087-8130.

(77) Baffou, G.; Rigneault, H. Femtosecond-pulsed optical heating of gold nanoparticles. *Physical Review B* **2011,** *84* (3), 035415.

(78) Pezzi, L.; De Sio, L.; Veltri, A.*, et al.* Photo-thermal effects in gold nanoparticles dispersed in thermotropic nematic liquid crystals. *Phys. Chem. Chem. Phys.* **2015,** *17* (31), 20281-20287.

(79) Jaque, D.; Maestro, L. M.; Del Rosal, B.*, et al.* Nanoparticles for photothermal therapies. *Nanoscale* **2014,** *6* (16), 9494-9530.

(80) Samadi, A.; Klingberg, H.; Jauffred, L., *et al.* Platinum nanoparticles: a non-toxic, effective and thermally stable alternative plasmonic material for cancer therapy and bioengineering. *Nanoscale* **2018,** *10* (19), 9097-9107.

(81) Richardson, H. H.; Carlson, M. T.; Tandler, P. J.; Hernandez, P.; Govorov, A. O. Experimental and theoretical studies of light-to-heat conversion and collective heating effects in metal nanoparticle solutions. *Nano Lett.* **2009,** *9* (3), 1139-1146.

(82) Baffou, G.; Berto, P.; Bermúdez Ureña, E., *et al.* Photoinduced heating of nanoparticle arrays. *ACS Nano* **2013,** *7* (8), 6478-6488.

(83) Pezzi, L.; Palermo, G.; Veltri, A., *et al.* Photo-thermal study of a layer of randomly distributed gold nanoparticles: From nano-localization to macro-scale effects. *J. Phys. D: Appl. Phys.* **2017,** *50* (43), 435302.

(84) Stockman, M. I.; Kneipp, K.; Bozhevolnyi, S. I., *et al.* Roadmap on plasmonics. *Journal of Optics* **2018,** *20* (4), 043001.

(85) Hirsch, L. R.; Stafford, R. J.; Bankson, J. A., *et al.* Nanoshell-mediated near-infrared thermal therapy of tumors under magnetic resonance guidance. *Proceedings of the National Academy of Sciences* **2003,** *100* (23), 13549-13554.

(86) Ali, M. R.; Wu, Y.; El-Sayed, M. A. Gold-nanoparticle-assisted plasmonic photothermal therapy advances toward clinical application. *J. Phys. Chem. C* **2019,** *123* (25), 15375-15393.

(87) Abadeer, N. S.; Murphy, C. J. Recent progress in cancer thermal therapy using gold nanoparticles. *J. Phys. Chem. C* **2016,** *120* (9), 4691-4716.

(88) Huang, X.; El-Sayed, M. A. Plasmonic photo-thermal therapy (PPTT). *Alexandria J. Med.* **2011,** *47* (1), 1-9.

(89) Cole, J. R.; Mirin, N. A.; Knight, M. W.; Goodrich, G. P.; Halas, N. J. Photothermal efficiencies of nanoshells and nanorods for clinical therapeutic applications. *J. Phys. Chem. C* **2009,** *113* (28), 12090-12094.

(90) Zharov, V. P.; Mercer, K. E.; Galitovskaya, E. N.; Smeltzer, M. S. Photothermal nanotherapeutics and nanodiagnostics for selective killing of bacteria targeted with gold nanoparticles. *Biophys. J.* **2006,** *90* (2), 619-627.

(91) Norman, R. S.; Stone, J. W.; Gole, A.; Murphy, C. J.; Sabo-Attwood, T. L. Targeted photothermal lysis of the pathogenic bacteria, Pseudomonas aeruginosa, with gold nanorods. *Nano Lett.* **2008,** *8* (1), 302-306.

(92) Alkilany, A. M.; Thompson, L. B.; Boulos, S. P.; Sisco, P. N.; Murphy, C. J. Gold nanorods: their potential for photothermal therapeutics and drug delivery, tempered by the complexity of their biological interactions. *Adv. Drug Delivery Rev.* **2012,** *64* (2), 190-199.

(93) Ali, H. R.; Ali, M. R.; Wu, Y., *et al.* Gold nanorods as drug delivery vehicles for rifampicin greatly improve the efficacy of combating Mycobacterium tuberculosis with good biocompatibility with the host cells. *Bioconjugate Chem.* **2016,** *27* (10), 2486-2492.

(94) Pierini, F.; Nakielski, P.; Urbanek, O.*, et al.* Polymer-based nanomaterials for photothermal therapy: from light-responsive to multifunctional nanoplatforms for synergistically combined technologies. *Biomacromolecules* **2018,** *19* (11), 4147-4167.

(95) Han, G.; Ghosh, P.; De, M.; Rotello, V. M. Drug and gene delivery using gold nanoparticles. *NanoBiotechnology* **2007,** *3* (1), 40-45.

(96) Kumar, A.; Mazinder Boruah, B.; Liang, X.-J. Gold nanoparticles: promising nanomaterials for the diagnosis of cancer and HIV/AIDS. *Journal of Nanomaterials* **2011,** *2011.*

(97) Qiu, G.; Gai, Z.; Tao, Y.*, et al.* Dual-functional plasmonic photothermal biosensors for highly accurate severe acute respiratory syndrome coronavirus 2 detection. *ACS Nano* **2020,** *14* (5), 5268-5277.

(98) Samson, R.; Navale, G. R.; Dharne, M. S. Biosensors: frontiers in rapid detection of COVID-19. *3 Biotech* **2020,** *10* (9), 1-9.

(99) Talebian, S.; Wallace, G. G.; Schroeder, A.; Stellacci, F.; Conde, J. Nanotechnology-based disinfectants and sensors for SARS-CoV-2. *Nat. Nanotechnol.* **2020,** *15* (8), 618-621.

(100) Neumann, O.; Urban, A. S.; Day, J.*, et al.* Solar vapor generation enabled by nanoparticles. *ACS Nano* **2013,** *7* (1), 42-49.

(101) Boriskina, S. V.; Green, M. A.; Catchpole, K.*, et al.* Roadmap on optical energy conversion. *Journal of Optics* **2016,** *18* (7), 073004.

(102) Liu, G. L.; Kim, J.; Lu, Y.; Lee, L. P. Optofluidic control using photothermal nanoparticles. *Nat. Mater.* **2006,** *5* (1), 27-32.

(103) Zhu, X.; Vannahme, C.; Højlund-Nielsen, E.; Mortensen, N. A.; Kristensen, A. Plasmonic colour laser printing. *Nat. Nanotechnol.* **2016,** *11* (4), 325-329.

(104) Ndukaife, J. C.; Kildishev, A. V.; Nnanna, A. G. A.*, et al.* Long-range and rapid transport of individual nano-objects by a hybrid electrothermoplasmonic nanotweezer. *Nat. Nanotechnol.* **2016,** *11* (1), 53.

(105) Wang, S.; Komvopoulos, K. Effect of material optical properties on thermo-plasmonics of heat-assisted magnetic recording devices. *J. Appl. Phys.* **2018,** *124* (18), 185109.

(106) BAFFOU, G.; QUIDANT, R. Thermoplasmonics. In *World Scientific Handbook of Metamaterials and Plasmonics*; pp 379-407.

(107) Lin, J.-T.; Hong, Y.-L.; Chang, C.-L. In *Selective cancer therapy via IR-laser-excited gold nanorods*, Optical Interactions with Tissues and Cells XXI, International Society for Optics and Photonics: 2010; p 75620R.

(108) Yue, K.; Nan, J.; Zhang, X.; Tang, J.; Zhang, X. Photothermal effects of gold nanoparticles induced by light emitting diodes. *Appl. Therm. Eng.* **2016,** *99*, 1093-1100.

(109) Carrillo-Torres, R.; García-Soto, M.; Morales-Chávez, S.*, et al.* Hollow Au–Ag bimetallic nanoparticles with high photothermal stability. *RSC Adv.* **2016,** *6* (47), 41304-41312.

(110) Maity, S.; Wu, W.-C.; Tracy, J. B.; Clarke, L. I.; Bochinski, J. R. Nanoscale steady-state temperature gradients within polymer nanocomposites undergoing continuous-wave photothermal heating from gold nanorods. *Nanoscale* **2017,** *9* (32), 11605-11618.

(111) Chiu, M.-J.; Chu, L.-K. Quantifying the photothermal efficiency of gold nanoparticles using tryptophan as an in situ fluorescent thermometer. *Phys. Chem. Chem. Phys.* **2015,** *17* (26), 17090-17100.

(112) Luk, A. T.; Nouizi, F.; Marks, M.; Kart, T.; Gulsen, G. In *Monitoring gold nanoparticle distribution with high resolution using photo-magnetic imaging*, Optical Interactions with Tissue and Cells XXVII, International Society for Optics and Photonics: 2016; p 97060M.

(113) Nakabeppu, O.; Chandrachood, M.; Wu, Y.; Lai, J.; Majumdar, A. Scanning thermal imaging microscopy using composite cantilever probes. *Appl. Phys. Lett.* **1995,** *66* (6), 694-696.

(114) Wang, Y.; Black, K. C.; Luehmann, H.*, et al.* Comparison study of gold nanohexapods, nanorods, and nanocages for photothermal cancer treatment. *ACS Nano* **2013,** *7* (3), 2068-2077.

(115) Chernov, G.; Ibarra-Valdez, J.; Carrillo-Torres, R.*, et al.* Improved Method of Study on the Photothermal Effect of Plasmonic Nanoparticles by Dynamic IR Thermography. *Plasmonics* **2019,** *14* (4), 935-944.

(116) López-Varela, K. A.; Cayetano-Castro, N.; Kolosovas-Machuca, E. S.*, et al.* Dynamic infrared thermography of nanoheaters embedded in skin-equivalent phantoms. *Journal of Nanomaterials* **2018,** *2018*.

(117) Ioffe, Z.; Shamai, T.; Ophir, A.*, et al.* Detection of heating in current-carrying molecular junctions by Raman scattering. *Nat. Nanotechnol.* **2008,** *3* (12), 727-732.

(118) Gao, L.; Wang, L.; Li, C.*, et al.* Single-cell photoacoustic thermometry. *J. Biomed. Opt.* **2013,** *18* (2), 026003.

(119) Gao, L.; Zhang, C.; Li, C.; Wang, L. V. Intracellular temperature mapping with fluorescence-assisted photoacoustic-thermometry. *Appl. Phys. Lett.* **2013,** *102* (19), 193705.

(120) Baffou, G.; Kreuzer, M.; Kulzer, F.; Quidant, R. Temperature mapping near plasmonic nanostructures using fluorescence polarization anisotropy. *Opt. Express* **2009,** *17* (5), 3291-3298.

(121) De Sio, L.; Placido, T.; Serak, S.*, et al.* Nano-Localized Heating Source for Photonics and Plasmonics. *Advanced Optical Materials* **2013,** *1* (12), 899-904.

(122) Huttmann, G.; Birngruber, R. On the possibility of high-precision photothermal microeffects and the measurement of fast thermal denaturation of proteins. *IEEE J. Sel. Top. Quantum Electron.* **1999,** *5* (4), 954-962.

(123) Hrelescu, C.; Stehr, J.; Ringler, M., *et al.* DNA melting in gold nanostove clusters. *J. Phys. Chem. C* **2010,** *114* (16), 7401-7411.

(124) Urban, A.; Fedoruk, M.; Horton, M., *et al.* Controlled nanometric phase transitions of phospholipid membranes by plasmonic heating of single gold nanoparticles. *Nano Lett.* **2009,** *9* (8), 2903-2908.

(125) Kyrsting, A.; Bendix, P. M.; Stamou, D. G.; Oddershede, L. B. Heat profiling of three-dimensionally optically trapped gold nanoparticles using vesicle cargo release. *Nano Lett.* **2011,** *11* (2), 888-892.

(126) Zhu, M.; Baffou, G.; Meyerbröker, N.; Polleux, J. Micropatterning thermoplasmonic gold nanoarrays to manipulate cell adhesion. *ACS Nano* **2012,** *6* (8), 7227-7233.

(127) Bahadori, A.; Oddershede, L. B.; Bendix, P. M. Hot-nanoparticle-mediated fusion of selected cells. *Nano Research* **2017,** *10* (6), 2034-2045.

(128) FLIR, A. The ultimate infrared handbook for R&D professionals. *Boston: FLIR Systems* **2010**.

(129) Tavakolian, P.; Mandelis, A. Perspective: Principles and specifications of photothermal imaging methodologies and their applications to non-invasive biomedical and non-destructive materials imaging. *J. Appl. Phys.* **2018,** *124* (16), 160903.

(130) Ranjit, S.; Choi, M.; Kim, W. Quantification of defects depth in glass fiber reinforced plastic plate by infrared lock-in thermography. *Journal of Mechanical Science and Technology* **2016,** *30* (3), 1111-1118.

(131) Pawar, S. S.; Vavilov, V. P. Applying the heat conduction-based 3D normalization and thermal tomography to pulsed infrared thermography for defect characterization in composite materials. *Int. J. Heat Mass Transfer* **2016,** *94*, 56-65.

(132) Gavrilov, D.; Maev, R. G.; Almond, D. A review of imaging methods in analysis of works of art: Thermographic imaging method in art analysis. *Can. J. Phys.* **2014,** *92* (4), 341-364.

(133) West, C. L.; Doughty, A. C.; Liu, K.; Chen, W. R. Monitoring tissue temperature during photothermal therapy for cancer. *Journal of Bio-X Research* **2019,** *2* (4), 159-168.

(134) Okano, Y.; Ito, K.; Ida, I.; Takahashi, M. The SAR evaluation method by a combination of thermographic experiments and biological tissue-equivalent phantoms. *IEEE Trans. Microwave Theory Tech.* **2000,** *48* (11), 2094-2103.

(135) Jones, B. F. A reappraisal of the use of infrared thermal image analysis in medicine. *IEEE Trans. Med. Imaging* **1998,** *17* (6), 1019-1027.

(136) Silvertown, J. D.; Wong, B. P.; Sivagurunathan, K. S., *et al.* Remineralization of natural early caries lesions in vitro by P11-4 monitored with photothermal radiometry and luminescence. *J. Investig. Clin. Dent.* **2017,** *8* (4), e12257.

(137) Kaiplavil, S.; Mandelis, A. Highly depth-resolved chirped pulse photothermal radar for bone diagnostics. *Rev. Sci. Instrum.* **2011,** *82* (7), 074906.

(138) Lashkari, A.; Pak, F.; Firouzmand, M. Full intelligent cancer classification of thermal breast images to assist physician in clinical diagnostic applications. *Journal of medical signals and sensors* **2016,** *6* (1), 12.

(139) Koay, J.; Herry, C.; Frize, M. In *Analysis of breast thermography with an artificial neural network*, The 26th Annual International Conference of the IEEE Engineering in Medicine and Biology Society, IEEE: 2004; pp 1159-1162.

(140) Van Natta, M.; Chen, P.; Herbek, S.*, et al.* The rise and regulation of thermal facial recognition technology during the COVID-19 pandemic. *Journal of Law and the Biosciences* **2020,** *7* (1).

(141) Jang, B.; Kim, Y. S.; Choi, Y. Effects of gold nanorod concentration on the depth-related temperature increase during hyperthermic ablation. *Small* **2011,** *7* (2), 265-270.

(142) Huang, X.; Jain, P. K.; El-Sayed, I. H.; El-Sayed, M. A. Determination of the minimum temperature required for selective photothermal destruction of cancer cells with the use of immunotargeted gold nanoparticles. *Photochem. Photobiol.* **2006,** *82* (2), 412-417.

(143) Von Maltzahn, G.; Park, J.-H.; Agrawal, A.*, et al.* Computationally guided photothermal tumor therapy using long-circulating gold nanorod antennas. *Cancer Res.* **2009,** *69* (9), 3892-3900.

(144) Maksimova, I. L.; Akchurin, G. G.; Khlebtsov, B. N.*, et al.* Near-infrared laser photothermal therapy of cancer by using gold nanoparticles: Computer simulations and experiment. *Medical Laser Application* **2007,** *22* (3), 199-206.

(145) Terentyuk, G. S.; Maslyakova, G. N.; Suleymanova, L. V.*, et al.* Laser-induced tissue hyperthermia mediated by gold nanoparticles: toward cancer phototherapy. *J. Biomed. Opt.* **2009,** *14* (2), 021016.

(146) Xiao, Y.; Wan, C.; Shahsafi, A.; Salman, J.; Kats, M. A. Depth Thermography: Noninvasive 3D Temperature Profiling Using Infrared Thermal Emission. *ACS Photonics* **2020,** *7* (4), 853-860.

(147) Kirimtat, A.; Krejcar, O.; Selamat, A.; Herrera-Viedma, E. FLIR vs SEEK thermal cameras in biomedicine: comparative diagnosis through infrared thermography. *BMC Bioinformatics* **2020,** *21* (2), 1-10.

(148) Ring, E.; Ammer, K. Infrared thermal imaging in medicine. *Physiol. Meas.* **2012,** *33* (3), R33.

(149) Cerruti, M. G.; Sauthier, M.; Leonard, D.*, et al.* Gold and silica-coated gold nanoparticles as thermographic labels for DNA detection. *Anal. Chem.* **2006,** *78* (10), 3282-3288.

(150) Planck, M. Ueber das Gesetz der Energieverteilung im Normalspectrum. *Annalen der Physik* **1901,** *309* (3), 553-563.

(151) Chandler, N. How Thermal Imaging Works. https://electronics.howstuffworks.com/thermal-imaging.htm (accessed May 21, 2013).

(152) Boldor, D.; Gerbo, N. M.; Monroe, W. T.*, et al.* Temperature measurement of carbon nanotubes using infrared thermography. *Chem. Mater.* **2008,** *20* (12), 4011-4016.

(153) Brites, C. D.; Lima, P. P.; Silva, N. J.*, et al.* Thermometry at the nanoscale. *Nanoscale* **2012,** *4* (16), 4799-4829.

(154) Collings, P. J. *Liquid crystals: nature's delicate phase of matter*, Princeton University Press: 2002.

(155) Meier, G.; Sackmann, E.; Grabmaier, J. G. *Applications of liquid crystals*, Springer Science & Business Media: 2012.

(156) Mitov, M. Cholesteric liquid crystals in living matter. *Soft Matter* **2017,** *13* (23), 4176-4209.

(157) Friedel, G. Les états mésomorphes de la matière. *Ann. Phys.* **1922,** *9* (18), 273-474.

(158) Pasechnik, S. V.; Chigrinov, V. G.; Shmeliova, D. V. *Liquid crystals: viscous and elastic properties in theory and applications*, John Wiley & Sons: 2009.

(159) Mingos, M.; Crabtree, R. *Comprehensive organometallic chemistry III*, Elsevier Science: 2007.

(160) Ito, N.; Sakamoto, K.; Arafune, R.; Ushioda, S. Relation between the molecular orientations of a very thin liquid crystal layer and an underlying rubbed polyimide film. *J. Appl. Phys.* **2000,** *88* (6), 3235-3241.

(161) Chigrinov, V.; Kwok, H. S.; Takada, H.; Takatsu, H. Photo-aligning by azo-dyes: physics and applications. *Liquid Crystals Today* **2005,** *14* (4), 1-15.

(162) Palermo, G.; Cataldi, U.; De Sio, L.*, et al.* Optical control of plasmonic heating effects using reversible photo-alignment of nematic liquid crystals. *Appl. Phys. Lett.* **2016,** *109* (19), 191906.

(163) Collings, P. J.; Hird, M. *Introduction to Liquid Crystals: Chemistry and Physics*, CRC Press: 1997.

(164) Singh, S.; Dunmur, D. A. *Liquid crystals: fundamentals*, World Scientific: 2002.

(165) Kimling, J.; Maier, M.; Okenve, B.*, et al.* Turkevich method for gold nanoparticle synthesis revisited. *J. Phys. Chem. B* **2006,** *110* (32), 15700-15707.

(166) Zhu, P. W.; Napper, D. H. Coil-to-globule type transitions and swelling of poly (N-isopropylacrylamide) and poly (acrylamide) at latex interfaces in alcohol–water mixtures. *J. Colloid Interface Sci.* **1996,** *177* (2), 343-352.

(167) Carlos, L. D.; Palacio, F.; Parada, F. P. *Thermometry at the Nanoscale: Techniques and Selected Applications*, Royal Society of Chemistry: 2016; Vol. 38.

(168) Guan, Y.; Zhang, Y. PNIPAM microgels for biomedical applications: from dispersed particles to 3D assemblies. *Soft Matter* **2011,** *7* (14), 6375-6384.

(169) Matsumoto, K.; Sakikawa, N.; Miyata, T. Thermo-responsive gels that absorb moisture and ooze water. *Nat. Commun.* **2018,** *9* (1), 1-7.

(170) Zhang, Z.; Wang, J.; Nie, X*., et al.* Near infrared laser-induced targeted cancer therapy using thermoresponsive polymer encapsulated gold nanorods. *J. Am. Chem. Soc.* **2014,** *136* (20), 7317-7326.

(171) Saeed, A.; Georget, D. M.; Mayes, A. G. Solid-state thermal stability and degradation of a family of poly (N-isopropylacrylamide-co-hydroxymethylacrylamide) copolymers. *J. Polym. Sci., Part A: Polym. Chem.* **2010,** *48* (24), 5848-5855.

(172) Wei, M.; Serpe, M. J. Temperature–Light Dual-Responsive Au@ PNIPAm Core-Shell Microgel-Based Optical Devices. *Particle & Particle Systems Characterization* **2019,** *36* (1), 1800326.

(173) Cho, J. E.; Kim, S.; Son, S*., et al.* Poly (N-isopropylacrylamide-co-methacrylic acid) Interfacial Layer for Efficient and Stable Inverted Organic Solar Cells. *J. Phys. Chem. C* **2019,** *123* (5), 2755-2765.

(174) Shi, Y.; Ma, C.; Peng, L.; Yu, G. Conductive “smart” hybrid hydrogels with PNIPAM and nanostructured conductive polymers. *Adv. Funct. Mater.* **2015,** *25* (8), 1219-1225.

(175) Shi, S.; Zhang, L.; Wang, T*., et al.* Poly (N-isopropylacrylamide)–Au hybrid microgels: synthesis, characterization, thermally tunable optical and catalytic properties. *Soft Matter* **2013,** *9* (46), 10966-10970.

(176) Mutharani, B.; Ranganathan, P.; Chen, S.-M. Stimuli-enabled reversible switched aclonifen electrochemical sensor based on smart PNIPAM/PANI-Cu hybrid conducting microgel. *Sensors Actuators B: Chem.* **2020,** *304*, 127232.

(177) Farooqi, Z. H.; Khan, S. R.; Begum, R.; Ijaz, A. Review on synthesis, properties, characterization, and applications of responsive microgels fabricated with gold nanostructures. *Rev. Chem. Eng.* **2016,** *32* (1), 49-69.

(178) Mehtala, J. G.; Zemlyanov, D. Y.; Max, J. P*., et al.* Citrate-stabilized gold nanorods. *Langmuir* **2014,** *30* (46), 13727-13730.

(179) Jin, S.; Liu, M.; Chen, S.; Gao, C. Synthesis, characterization and the rapid response property of the temperature responsive PVP-g-PNIPAM hydrogel. *European Polymer Journal* **2008,** *44* (7), 2162-2170.

(180) Gans, R. Über die form ultramikroskopischer goldteilchen. *Annalen der Physik* **1912,** *342* (5), 881-900.

(181) Sun, S.; Wu, P. A one-step strategy for thermal-and pH-responsive graphene oxide interpenetrating polymer hydrogel networks. *J. Mater. Chem.* **2011,** *21* (12), 4095-4097.

(182) Pitsillides, C. M.; Joe, E. K.; Wei, X.; Anderson, R. R.; Lin, C. P. Selective cell targeting with light-absorbing microparticles and nanoparticles. *Biophys. J.* **2003,** *84* (6), 4023-4032.

(183) Jin, H.-G.; Zhong, W.; Yin, S*., et al.* Lesson from nature: biomimetic self-assembling phthalocyanines for high-efficient photothermal therapy within the biological transparent window. *ACS Appl. Mater. Interfaces* **2019,** *11* (4), 3800-3808.

(184) Stabile, J.; Najafali, D.; Cheema, Y*., et al.* Engineering gold nanoparticles for photothermal therapy, surgery, and imaging. In *Nanoparticles for Biomedical Applications*; Elsevier: 2020; pp 175-193.

(185) Raeesi, V.; Chan, W. C. Improving nanoparticle diffusion through tumor collagen matrix by photo-thermal gold nanorods. *Nanoscale* **2016,** *8* (25), 12524-12530.

(186) De Angelis, B.; Depalo, N.; Petronella, F*., et al.* Stimuli-responsive nanoparticle-assisted immunotherapy: a new weapon against solid tumours. *J. Mater. Chem. B* **2020,** *8* (9), 1823-1840.

(187) de Miguel, I.; Prieto, I.; Albornoz, A*., et al.* Plasmon-Based Biofilm Inhibition on Surgical Implants. *Nano Lett.* **2019,** *19* (4), 2524-2529.

(188) Kim, C.-B.; Yi, D. K.; Kim, P. S. S.; Lee, W.; Kim, M. J. Rapid photothermal lysis of the pathogenic bacteria, Escherichia coli using synthesis of gold nanorods. *J. Nanosci. Nanotechnol.* **2009,** *9* (5), 2841-2845.

(189) Biosciences, I. N. Pilot study of AuroLase (tm) therapy in refractory and/or recurrent tumors of the head and neck. *ClinicalTrials gov [Internet]. Bethesda (MD): National Library of Medicine (US)* **2000**.

(190) Feliu, N.; Docter, D.; Heine, M*., et al.* In vivo degeneration and the fate of inorganic nanoparticles. *Chem. Soc. Rev.* **2016,** *45* (9), 2440-2457.

(191) Theuretzbacher, U. Global antimicrobial resistance in Gram-negative pathogens and clinical need. *Curr. Opin. Microbiol.* **2017,** *39*, 106-112.

(192) Wistrand, C.; Söderquist, B.; Magnusson, A.; Nilsson, U. The effect of preheated versus room-temperature skin disinfection on bacterial colonization during pacemaker device implantation: a randomized controlled non-inferiority trial. *Antimicrobial resistance and infection control* **2015,** *4* (1), 44.

(193) Carvalho, F.; George, J.; Sheikh, H. M. A.; Selvin, R. Advances in screening, detection and enumeration of Escherichia coli using nanotechnology-based methods: a review. *J. Biomed. Nanotechnol.* **2018,** *14* (5), 829-846.

(194) Teng, C. P.; Zhou, T.; Ye, E*., et al.* Effective targeted photothermal ablation of multidrug resistant bacteria and their biofilms with NIR-absorbing gold nanocrosses. *Advanced healthcare materials* **2016,** *5* (16), 2122-2130.

(195) Schachter, D. The source of toxicity in CTAB and CTAB-stabilized gold nanorods. Rutgers University-Graduate School-New Brunswick, 2013.

(196) Abreu, A. C.; Tavares, R. R.; Borges, A.; Mergulhão, F.; Simões, M. Current and emergent strategies for disinfection of hospital environments. *J. Antimicrob. Chemother.* **2013,** *68* (12), 2718-2732.

(197) Placido, T.; Aragay, G.; Pons, J*., et al.* Ion-directed assembly of gold nanorods: a strategy for mercury detection. *ACS Appl. Mater. Interfaces* **2013,** *5* (3), 1084-1092.

(198) Wang, Y.; Wan, J.; Miron, R. J.; Zhao, Y.; Zhang, Y. Antibacterial properties and mechanisms of gold–silver nanocages. *Nanoscale* **2016,** *8* (21), 11143-11152.

(199) Baharoglu, Z.; Mazel, D. SOS, the formidable strategy of bacteria against aggressions. *FEMS Microbiol. Rev.* **2014,** *38* (6), 1126-1145.

(200) Pankey, G. A.; Sabath, L. Clinical relevance of bacteriostatic versus bactericidal mechanisms of action in the treatment of Gram-positive bacterial infections. *Clin. Infect. Dis.* **2004,** *38* (6), 864-870.

(201) Yu, E. Y.; Bishop, M.; Zheng, B.*, et al.* Magnetic particle imaging: a novel in vivo imaging platform for cancer detection. *Nano Lett.* **2017,** *17* (3), 1648-1654.

(202) Huang, X.; El-Sayed, I. H.; El-Sayed, M. A. Applications of gold nanorods for cancer imaging and photothermal therapy. In *Cancer Nanotechnol.*; Springer: 2010; pp 343-357.

(203) Riley, R. S.; Day, E. S. Gold nanoparticle-mediated photothermal therapy: applications and opportunities for multimodal cancer treatment. *Wiley Interdiscip. Rev. Nanomed. Nanobiotechnol.* **2017,** *9* (4), e1449.

(204) Biosciences, N. Inc. Pilot study of AuroLase therapy in refractory and/or recurrent tumors of the head and neck. *Clinical-Trials. gov [Internet]; National Library of Medicine: Bethesda, MD.* **2000**, NCT00848042.

(205) Kharlamov, A.; Tyurnina, A.; Veselova, V.*, et al.* Plasmonics for treatment of atherosclerosis: results of NANOM-FIM trial. *J. Nanomed. Nanotechol.* **2013,** *4* (160), 2.

(206) Melamed, J. R.; Edelstein, R. S.; Day, E. S. Elucidating the fundamental mechanisms of cell death triggered by photothermal therapy. *ACS Nano* **2015,** *9* (1), 6-11.

(207) Rostro-Kohanloo, B. C.; Bickford, L. R.; Payne, C. M.*, et al.* The stabilization and targeting of surfactant-synthesized gold nanorods. *Nanotechnology* **2009,** *20* (43), 434005.

(208) Chamberland, D. L.; Agarwal, A.; Kotov, N.*, et al.* Photoacoustic tomography of joints aided by an Etanercept-conjugated gold nanoparticle contrast agent—an ex vivo preliminary rat study. *Nanotechnology* **2008,** *19* (9), 095101.

(209) Niidome, T.; Ohga, A.; Akiyama, Y.*, et al.* Controlled release of PEG chain from gold nanorods: targeted delivery to tumor. *Bioorg. Med. Chem.* **2010,** *18* (12), 4453-4458.

(210) Rayavarapu, R. G.; Petersen, W.; Hartsuiker, L.*, et al.* In vitro toxicity studies of polymer-coated gold nanorods. *Nanotechnology* **2010,** *21* (14), 145101.

(211) Sebak, A. Limitations of Pegylated Nanocarriers: Unfavourable Physicochemical Properties, Biodistribution Patterns and Cellular and Subcellular Fates. *Int. J. Pharm.* **2018,** *10*, 6-12.

(212) Bolaños, K.; Kogan, M. J.; Araya, E. Capping gold nanoparticles with albumin to improve their biomedical properties. *Int. J. Nanomedicine* **2019,** *14*, 6387.

(213) Adura, C.; Guerrero, S.; Salas, E.*, et al.* Stable conjugates of peptides with gold nanorods for biomedical applications with reduced effects on cell viability. *ACS Appl. Mater. Interfaces* **2013,** *5* (10), 4076-4085.

(214) AL-Jawad, S. M.; Taha, A. A.; Al-Halbosiy, M. M.; AL-Barram, L. F. Synthesis and characterization of small-sized gold nanoparticles coated by bovine serum albumin (BSA) for cancer photothermal therapy. *Photodiagnosis Photodyn. Ther.* **2018,** *21*, 201-210.

(215) Mocan, L.; Matea, C.; Tabaran, F. A.*, et al.* Selective ex vivo photothermal nano-therapy of solid liver tumors mediated by albumin conjugated gold nanoparticles. *Biomaterials* **2017,** *119*, 33-42.

(216) Zhang, L.; Xia, K.; Bai, Y.-Y.*, et al.* Synthesis of gold nanorods and their functionalization with bovine serum albumin for optical hyperthermia. *J. Biomed. Nanotechnol.* **2014,** *10* (8), 1440-1449.

(217) Perotto, G.; Sandri, G.; Pignatelli, C.; Milanesi, G.; Athanassiou, A. Water-based synthesis of keratin micro-and nanoparticles with tunable mucoadhesive properties for drug delivery. *J. Mater. Chem. B* **2019,** *7* (28), 4385-4392.

(218) Rouse, J. G.; Van Dyke, M. E. A review of keratin-based biomaterials for biomedical applications. *Materials* **2010,** *3* (2), 999-1014.

(219) Wang, J.; Hao, S.; Luo, T.*, et al.* Feather keratin hydrogel for wound repair: preparation, healing effect and biocompatibility evaluation. *Colloids Surf. B. Biointerfaces* **2017,** *149*, 341-350.

(220) Park, M.; Richardson, A.; Pandzic, E.*, et al.* Visualizing the contribution of keratin-14+ limbal epithelial precursors in corneal wound healing. *Stem Cell Rep.* **2019,** *12* (1), 14-28.

(221) Cilurzo, F.; Selmin, F.; Aluigi, A.; Bellosta, S. Regenerated keratin proteins as potential biomaterial for drug delivery. *Polym. Adv. Technol.* **2013,** *24* (11), 1025-1028.

(222) Zhi, X.; Wang, Y.; Li, P.; Yuan, J.; Shen, J. Preparation of keratin/chlorhexidine complex nanoparticles for long-term and dual stimuli-responsive release. *RSC Adv.* **2015,** *5* (100), 82334-82341.

(223) Li, Y.; Lin, J.; Zhi, X.*, et al.* Triple stimuli-responsive keratin nanoparticles as carriers for drug and potential nitric oxide release. *Mater. Sci. Eng. C* **2018,** *91*, 606-614.

(224) Li, Q.; Zhu, L.; Liu, R.*, et al.* Biological stimuli responsive drug carriers based on keratin for triggerable drug delivery. *J. Mater. Chem.* **2012,** *22* (37), 19964-19973.

(225) Suarato, G.; Contardi, M.; Perotto, G.*, et al.* From fabric to tissue: Recovered wool keratin/polyvinylpyrrolidone biocomposite fibers as artificial scaffold platform. *Mater. Sci. Eng. C* **2020,** *116*, 111151.

(226) Martin, J. J.; Cardamone, J. M.; Irwin, P. L.; Brown, E. M. Keratin capped silver nanoparticles–Synthesis and characterization of a nanomaterial with desirable handling properties. *Colloids Surf. B. Biointerfaces* **2011,** *88* (1), 354-361.

(227) Lü, X.; Cui, S. Wool keratin-stabilized silver nanoparticles. *Bioresour. Technol.* **2010,** *101* (12), 4703-4707.

(228) Irwin, P.; Martin, J.; Nguyen, L.-H.*, et al.* Antimicrobial activity of spherical silver nanoparticles prepared using a biocompatible macromolecular capping agent: evidence for induction of a greatly prolonged bacterial lag phase. *J. Nanobiotechnol.* **2010,** *8* (1), 34.

(229) Jin, K.; Luo, Z.; Zhang, B.; Pang, Z. Biomimetic nanoparticles for inflammation targeting. *Acta Pharm. Sin. B* **2018,** *8* (1), 23-33.

(230) Liu, J.; Peng, Q. Protein-gold nanoparticle interactions and their possible impact on biomedical applications. *Acta Biomater.* **2017,** *55*, 13-27.

(231) Charbgoo, F.; Nejabat, M.; Abnous, K.*, et al.* Gold nanoparticle should understand protein corona for being a clinical nanomaterial. *J. Control. Release* **2018,** *272*, 39-53.

(232) Hottinger, A. F.; Stupp, R.; Homicsko, K. Standards of care and novel approaches in the management of glioblastoma multiforme. *Chin. J. Cancer* **2014,** *33* (1), 32.

(233) Stupp, R.; Mason, W. P.; Van Den Bent, M. J.*, et al.* Radiotherapy plus concomitant and adjuvant temozolomide for glioblastoma. *N. Engl. J. Med.* **2005,** *352* (10), 987-996.

(234) Yamauchi, K.; Yamauchi, A.; Kusunoki, T.; Kohda, A.; Konishi, Y. Preparation of stable aqueous solution of keratins, and physiochemical and biodegradational properties of films. *J. Biomed. Mater. Res.* **1996,** *31* (4), 439-444.

(235) Hu, X.; Kaplan, D.; Cebe, P. Determining beta-sheet crystallinity in fibrous proteins by thermal analysis and infrared spectroscopy. *Macromolecules* **2006,** *39* (18), 6161-6170.

(236) Pignatelli, C.; Perotto, G.; Nardini, M.*, et al.* Electrospun silk fibroin fibers for storage and controlled release of human platelet lysate. *Acta Biomater.* **2018,** *73*, 365-376.

(237) Ferraris, S.; Prato, M.; Vineis, C.*, et al.* Coupling of keratin with titanium: A physico-chemical characterization of functionalized or coated surfaces. *Surf. Coat. Technol.* **2020,** *397*, 126057.

(238) Gobbo, P.; Biesinger, M. C.; Workentin, M. S. Facile synthesis of gold nanoparticle (AuNP)–carbon nanotube (CNT) hybrids through an interfacial Michael addition reaction. *Chem. Commun.* **2013,** *49* (27), 2831-2833.

(239) Chirico, G.; Pallavicini, P.; Collini, M. Gold nanostars for superficial diseases: a promising tool for localized hyperthermia? *Nanomed.* **2014,** *9* (1), 1-3.

(240) Nienhaus, K.; Wang, H.; Nienhaus, G. Nanoparticles for biomedical applications: exploring and exploiting molecular interactions at the nano-bio interface. *Mater. Today Adv.* **2020,** *5*, 100036.

(241) Yang, H.; He, H.; Tong, Z.*, et al.* The impact of size and surface ligand of gold nanorods on liver cancer accumulation and photothermal therapy in the second near-infrared window. *J. Colloid Interface Sci.* **2020,** *565*, 186-196.

(242) Bhamidipati, M.; Fabris, L. Multiparametric assessment of gold nanoparticle cytotoxicity in cancerous and healthy cells: the role of size, shape, and surface chemistry. *Bioconjugate Chem.* **2017,** *28* (2), 449-460.

(243) Anderson, R. R.; Parrish, J. A. The optics of human skin. *J. Investig. Dermatol.* **1981,** *77* (1), 13-19.

(244) Ersen, A.; Sahin, M. Polydimethylsiloxane-based optical waveguides for tetherless powering of floating microstimulators. *J. Biomed. Opt.* **2017,** *22* (5), 055005.

(245) Weiß, T.; Hildebrand, G.; Schade, R.; Liefeith, K. Two-photon polymerization for microfabrication of three-dimensional scaffolds for tissue engineering application. *Eng. Life Sci.* **2009,** *9* (5), 384-390.

(246) LaFratta, C. N.; Fourkas, J. T.; Baldacchini, T.; Farrer, R. A. Multiphoton fabrication. *Angew. Chem. Int. Ed.* **2007,** *46* (33), 6238-6258.

(247) Belfield, K. D.; Ren, X.; Van Stryland, E. W.*, et al.* Near-IR two-photon photoinitiated polymerization using a fluorone/amine initiating system. *J. Am. Chem. Soc.* **2000,** *122* (6), 1217-1218.

(248) Panusa, G.; Pu, Y.; Wang, J.; Moser, C.; Psaltis, D. Fabrication of Sub-Micron Polymer Waveguides through Two-Photon Polymerization in Polydimethylsiloxane. *Polymers* **2020,** *12* (11), 2485.

(249) Wang, R.; Li, D.; Wu, H.*, et al.* All-optical intensity modulator by polarization-dependent graphene-microfiber waveguide. *IEEE Photonics Journal* **2017,** *9* (5), 1-8.

(250) Jun, L.; Chien-Hui, W.; Gauza, S.; Lu, R.; Shin-Tson, W. Refractive indices of liquid crystals for display applications. *Journal of Display Technology* **2005,** *1* (1), 51-61.